Old Dominion University
ODU Digital Commons

Physics Theses & Dissertations | Physics

Summer 1994

Strong Magnetic Field Effects and Molecular Processes with Applications to White Dwarfs

Phillip C. Stancil
Old Dominion University

Follow this and additional works at: https://digitalcommons.odu.edu/physics_etds

 Part of the Astrophysics and Astronomy Commons, and the Atomic, Molecular and Optical Physics Commons

Recommended Citation

Stancil, Phillip C.. "Strong Magnetic Field Effects and Molecular Processes with Applications to White Dwarfs" (1994). Doctor of Philosophy (PhD), dissertation, Physics, Old Dominion University, DOI: 10.25777/fxg0-7j95
https://digitalcommons.odu.edu/physics_etds/121

This Dissertation is brought to you for free and open access by the Physics at ODU Digital Commons. It has been accepted for inclusion in Physics Theses & Dissertations by an authorized administrator of ODU Digital Commons. For more information, please contact digitalcommons@odu.edu.

STRONG MAGNETIC FIELD EFFECTS AND MOLECULAR PROCESSES WITH APPLICATIONS TO WHITE DWARFS

by
Phillip C. Stancil
B.S. May 1986, Old Dominion University
M.S. May 1990, Old Dominion University

A Dissertation submitted to the Faculty of
Old Dominion University in Partial Fulfillment of the
Requirements for the Degree of

DOCTOR OF PHILOSOPHY

PHYSICS

OLD DOMINION UNIVERSITY
August, 1994

Approved by:

Reproduced with permission of the copyright owner. Further reproduction prohibited without permission.

STRONG MAGNETIC FIELD EFFECTS AND MOLECULAR PROCESSES WITH APPLICATIONS TO WHITE DWARFS

Phillip C. Stancil

Old Dominion University, 1994

Dissertation Advisors: Prof. Gary E. Copeland

and Prof. Alex Dalgarno

ABSTRACT

Radiative transitions of hydrogenlike atoms in external magnetic fields of strength applicable to magnetic white dwarfs, i.e. $B \lesssim 10^3$ megagauss, have been investigated for field-free principal quantum numbers $n \lesssim 6$. Finite proton mass corrections are included. Relativistic corrections are also investigated. Transition probabilities are determined using the length, velocity, and acceleration forms of the electric dipole operator. Discrepancies between previous calculations and magnetic white dwarf observations of low-lying bound-bound transitions have been studied. New results for high-lying transitions are also obtained.

The transition probability for the hydrogenlike $2s$ two-photon decay has been investigated and shown to increase substantially with field strength. The computed two-photon spectra show resonances and interference minima. Anomalous Zeeman depolarization features are found in computed two-photon polarization spectra of alkali atoms in laboratory strength magnetic fields. A

Reproduced with permission of the copyright owner. Further reproduction prohibited without permission.

previously observed fine structure depolarization feature is shown to decay with decreasing field strength.

The molecular processes of radiative association, photodissociation, and free-free absorption for the ions He_2^+ and H_2^+ are investigated for various temperatures. New partition functions and dissociation equilibrium constants have also been determined for the two molecular ions.

A persistent $\sim$ 2 nm discrepancy in the Lyα σ^- line center between theoretical calculations and observations of the highly magnetic ($\sim$ 320 MG) white dwarf Grw +70°8247 is interpreted as resonance broadening due to hydrogen-proton and hydrogen-hydrogen collisions in the high-density ($\sim 10^{21}$ cm^{-3}), high-magnetic environment of the star.

The detection prospects of He_2^+ and H_2^+ in cool white dwarfs are discussed and shown to be insignificant. It is suggested, though, that continuous absorption by He_2^+ may be responsible for an observed ultraviolet flux deficiency in some cool helium-rich white dwarfs.

Reproduced with permission of the copyright owner. Further reproduction prohibited without permission.

ACKNOWLEDGEMENTS

I am grateful for the guidance and support afforded me by my two advisors Prof. Gary E. Copeland of the Department of Physics and Prof. Alex Dalgarno of the Astronomy Department at Harvard University. I also thank Prof. Mark D. Havey, Prof. J. Wallace Van Orden, and Prof. Lawrence B. Weinstein of the Department of Physics and Prof. Robert L. Ake of the Department of Chemistry and Biochemistry for serving on my dissertation committee and for providing many helpful suggestions.

I also thank Prof. James L. Cox, Chair of the Department of Physics, Prof. John S. Eck, Associate Vice President for Research and Graduate Studies, Ms. Virginia Maddry, Ms. Valerie Sorenson of the Smithsonian Astrophysical Observatory, and Ms. Verity Parris of the Institute for Theoretical Atomic and Molecular Physics for helping to keep my relocation to Cambridge as painless as possible. I am indebted to Dr. James F. Babb, Dr. Kate P. Kirby, and Dr. George A. Victor, all of the Harvard-Smithsonian Center for Astrophysics, and Ms. Angela Putney of Palomar Observatory, California Institute of Technology, for many enlightening conversions.

Support for this work was provided by the Smithsonian Astrophysical Observatory and the Virginia Space Grant Consortium. I thank the Institute for Theoretical Atomic and Molecular Physics for use of their computational resources.

Reproduced with permission of the copyright owner. Further reproduction prohibited without permission.

TABLE OF CONTENTS

Reproduced with permission of the copyright owner. Further reproduction prohibited without permission.

LIST OF TABLES

Reproduced with permission of the copyright owner. Further reproduction prohibited without permission.

Reproduced with permission of the copyright owner. Further reproduction prohibited without permission.

LIST OF FIGURES

FIGURES PAGE

Reproduced with permission of the copyright owner. Further reproduction prohibited without permission.

Reproduced with permission of the copyright owner. Further reproduction prohibited without permission.

1. INTRODUCTION

Some atomic and molecular data which are difficult to acquire in the laboratory must be determined by theoretical means. Generally, this information is necessary for astrophysical investigations where the species are not easily produced, the process of interest is difficult to separate from others, or the environment cannot be recreated on the earth. This dissertation considers two such situations: (i) the hydrogen atom in a strong magnetic field and (ii) radiative formation and destruction of diatomic molecular ions consisting of hydrogen or helium.

Theoretical investigations of hydrogen and other atoms in strong magnetic fields have been pursued for the past thirty years with ever increasing sophistication and precision [1–43]. This work was originally stimulated by the discovery of strong magnetic fields in neutron stars [44] and some white dwarfs [45]. Recent theoretical spectra incorporating calculated atomic data with atmospheric models of magnetic white dwarf stars have revealed some discrepancies with flux and polarization measurements [46,47]. This development and the increasing precision of observations foster further and more accurate calculations of atomic structure in strong fields. We present new calculations of nonrelativistic energies, relativistic corrections, and transition probabilities for hydrogen and the hydrogenlike ion He^+ in Sec. 2.1.

While structure calculations have received considerable attention, little work has been directed toward higher-order processes, for example, photoionization and two-photon transitions. Photoionization calculations have centered predominately around the low-field regime ($B \sim 6$ Tesla (T), where 1 T = 10^4 G) [48–52] in an effort to understand experimental observations [53–56]. Some work in intense fields has also been performed by Schmitt et al. [57] and Wunner et al. [58] for applications to neutron stars. Investigations in the intermediate-field regime has been generally

Reproduced with permission of the copyright owner. Further reproduction prohibited without permission.

limited to the work of Alijah et al. [59] and Wang and Greene [60], but only for transitions originating from the ground state. Photoionization cross sections from excited states are believed to be necessary to resolve the above mentioned polarization spectra discrepancies in magnetic white dwarfs. Though these cross sections are not given here, the wave functions determined in Sec. 2.1 are a first step in that calculation, possibly by time-dependent methods [61], to be attempted in the future. Some discussion is given in Sec. 4.1 on the anticipated impact of magnetic-field-dependent photoionization cross sections on the interpretation of spectra from the star Grw $+70°8247$.

Atomic two-photon transitions in a magnetic field have not been previously investigated theoretically or experimentally. Experiments involving two-photon absorption and polarization of alkali atoms in the absence of a field are numerous and reveal interference effects due to fine structure coherence [62–65]. A calculation of two-photon electron cyclotron emission in a field of 10^9 T has been performed by Alexander and Mészáros [66,67] who demonstrate its importance as an opacity source in the x-ray spectra of accreting pulsars. Sec. 2.2 presents the first calculation of spontaneous two-photon emission by hydrogenlike atoms in strong magnetic fields while two-photon polarization of alkali atoms in laboratory strength magnetic fields is computationally investigated in Sec. 2.3.

Light diatomic molecules particularly those containing hydrogen are important in many astrophysical situations with the most important being H_2. In contrast, the molecular ions H_2^+ and He_2^+ have not been astronomically observed. We investigate in Sec 3.1 the formation of these ions by radiative association while their destruction by photodissociation is studied in Sec. 3.2. New semiclassical calculations of free-free absorption by H_2^+ and He_2^+ are also given in Sec. 3.2. Sec. 3.3 gives new tabulations of H_2^+ and He_2^+ partition functions and dissociation equilibrium constants which are useful for computations of cool stellar atmospheres and absorption coefficients.

Reproduced with permission of the copyright owner. Further reproduction prohibited without permission.

Finally, an effort is made to apply the results of Chapters 2 and 3, particularly Secs. 2.1 and 3.2, to investigations of magnetic and cool white dwarf stars. These stars contain the extreme environmental conditions of strong magnetic fields and high particle densities certainly unreachable by earth-bound experimental investigations. They are excellent laboratories for testing theoretical calculations in these peculiar situations.

Reproduced with permission of the copyright owner. Further reproduction prohibited without permission.

2. MAGNETIC FIELD EFFECTS ON ATOMS

2.1. Structure Calculations of Hydrogenlike Atoms

2.1.1. Nonrelativistic Infinite Proton Mass Energies

For an electron in the presence of a nucleus of infinite mass with charge Z and a uniform external magnetic field B parallel to the z-axis, the Schrödinger Hamiltonian is given by*

$$H_o = -\frac{\nabla^2}{2} - \frac{Z}{r} + B\left(\frac{m}{2} + m_s\right) + \frac{B^2}{8} r^2 \sin^2\theta \qquad (2.1\text{-}1)$$

where m is the magnetic or azimuthal quantum number, m_s is the spin quantum number, and $B = 1$ corresponds to $\sim 2.350 \times 10^5$ T (2350 MG). The individual terms of the Hamiltonian are the kinetic energy T, the Coulomb potential V_C , the linear Zeeman potential V_{LZ} , and the quadratic Zeeman potential V_{QZ} , respectively.

The strong field problem can be loosely divided into three regimes [1]: (i) the Paschen-Back region where $\langle V_C \rangle >> \langle V_{LZ} \rangle >> \langle V_{QZ} \rangle$, (ii) the intermediate-field region with $\langle V_{LZ} \rangle \gtrsim \langle V_{QZ} \rangle \approx \langle V_C \rangle$ or $\langle V_{QZ} \rangle \gtrsim \langle V_{LZ} \rangle \approx \langle V_C \rangle$, and (iii) the intense-field or Landau regime where $\langle V_{QZ} \rangle > \langle V_{LZ} \rangle >> \langle V_C \rangle$. Here $\langle V \rangle$ corresponds to the expectation value of the operator V.

As is well known, in the Paschen-Back regime the linear Zeeman potential can be treated as a perturbation to the field-free solution [68]. The shift in energy from the field-free eigenvalue is simply $B(m/2 + m_s)$ which is independent of the principal quantum number n and the angular momentum quantum number ℓ. Note that in this

---

*Atomic units are used throughout this work unless otherwise noted. These units correspond to setting $e = h = m_e = 1$ and $\alpha = 1/c$. Lengths are given in Bohr radii a_o and energies in au (hartrees) where 1 au = 27.2113962 eV.

Reproduced with permission of the copyright owner. Further reproduction prohibited without permission.

regime n and ℓ are "good" quantum numbers while for higher field strengths they are not. Further, only m and z-parity π remain "good" quantum numbers at any field strength. Nevertheless, n and ℓ will be used to label the states since they indicate the dominant contribution.

Since the spin and angular momentum are not coupled in strong fields, m_s is not allowed to change during a transition, giving the selection rule

$$\Delta m_s = 0 \tag{2.1-2}$$

in addition to

$$\Delta m = 0, \pm 1. \tag{2.1-3}$$

Selection rules (2.1-2) and (2.1-3) are applicable for all the work considered in Secs. 2.1 and 2.2. As a consequence of Eq. (2.1-2), and as is customary, only spin down states, $m_s = -\frac{1}{2}$, will be considered since we are ultimately only interested in spin-allowed transitions.

For the intense-field regime, V_C is treated as a perturbation to the solution of a free electron in a magnetic field. This approach is generally referred to as the adiabatic approximation. Much work involving the energy levels and radiative transitions has been carried out by various groups [4,5,17–19,23,29,30,36,43], generally for applications to neutron stars with field strengths of $\sim 10^6$ MG and as such will not be considered here.

In the intermediate-field regime, V_C and the Zeeman contributions are comparable so a perturbative approach is inappropriate. The Ritz variational method [68] has received the most attention and has been applied in the intermediate-field regime by the Louisiana State University (LSU) group [6–12], Kara and McDowell [16], the Tübingen group [17–23], and others. The method is based on Rayleigh's variational principle which states for the Hamiltonian H_o with exact eigenvalue E, an approximate eigenvalue $E(\psi)$ is given by

Reproduced with permission of the copyright owner. Further reproduction prohibited without permission.

$$E(\psi) = \frac{\langle\psi|H_o|\psi\rangle}{\langle\psi|\psi\rangle} \geq E \tag{2.1-4}$$

where ψ is an arbitrary trial function which differs from the exact eigenfunction of H_o to first order. $E(\psi)$ is larger than E, but with a small difference to only second order which decreases as ψ approaches the exact eigenfunction. The Ritz method chooses ψ to be a function with adjustable parameters which are optimized to obtain the minimum value of $E(\psi)$. $E(\psi)$ is then an upper limit to the exact eigenvalue E.

Various types of trial functions have been used for the intermediate-field regime, but most are based on the expansion of field-free hydrogenic functions. The LSU group used a basis of the form

$$\phi_{i\ell}^m = (a_i r^\ell + b_i r^{\ell+1}) \exp(-\beta_i r) Y_\ell^m(\theta, \varphi) \tag{2.1-5}$$

where $Y_\ell^m(\theta, \varphi)$ is a spherical harmonic, a_i and b_i are linear expansion coefficients, and β_i is a nonlinear variational parameter. The Tübingen group used a form similar to Eq. (2.1-5) for $B \lesssim 1$ given by

$$\phi_\ell^m = \frac{1}{r} f_\ell(r) Y_\ell^m(\theta, \varphi) \tag{2.1-6}$$

where $f_\ell(r)$ is a numerical function which reduces to the usual hydrogenic radial function as $B \to 0$. For $B \gtrsim 1$, the Tübingen group incorporated an expansion in terms of the Landau functions $\Phi_N^m(\rho, \varphi)$ given in cylindrical coordinates by

$$\phi_N^m = g_N(z) \Phi_N^m(\rho, \varphi) \tag{2.1-7}$$

where $g_N(z)$ is a numerical horizontal hydrogenic-type function,

$$\Phi_N^m(\rho, \varphi) = \xi^{|m|/2} L_N^{|m|}(\xi) \exp(-\xi/2) \exp(im\varphi), \tag{2.1-8}$$

N is the Landau quantum number, $L_N^{|m|}$ is an associated Laguerre polynomial, $\xi = (\rho/\rho_o)^2$, $\rho_o = \sqrt{2/\alpha B}$, and α is the fine structure constant. The Landau functions are exact solutions of a free electron in a magnetic field which is obtained for the Hamiltonian of Eq. (2.1-1) in the limit where $B \to \infty$ or $Z \to 0$.

Reproduced with permission of the copyright owner. Further reproduction prohibited without permission.

Kara and McDowell [16], who were only interested in $B > 0.1$, chose to work in the cylindrical basis

$$\phi^M = z^\beta \rho^\gamma \exp(-\delta r^2) \exp(im\varphi) \tag{2.1-9}$$

where β, γ, and δ are nonlinear variational parameters.

The Tübingen expansions of Eqs. (2.1-6) and (2.1-7) do not include a nonlinear variational parameter. Instead, they exploit the limiting symmetries by choosing basis sets which give the exact solution as $B \to 0$ (hydrogenic: spherical) and $B \to \infty$ or $Z \to 0$ (Landau: cylindrical). Their results appear to converge to higher accuracy with fewer terms than the LSU results or those of Kara and McDowell, however convergence becomes poorer as $B = 1$ is approached from either limit. All of these calculations give transition data for $n \lesssim 5$ typically. The most comprehensive work in terms of field strength range is that by Forster et al. [21] who considered all three field regimes but for $n \leq 3$ only. Wunner et al. [22] supplemented these calculations for n up to five, but concentrated on the intermediate regime. The work of Henry and O'Connell [12] is also limited to the intermediate-field region, but includes $n \leq 5$.

Most recently, Chen and Goldman [37] incorporated both limiting symmetries into a single function by constructing a mixed Slater-Landau basis of the form

$$\phi^m_{n\ell} = r^{n-1} \exp(-\lambda' r - \beta r^2 \sin^2\theta) \cos^{\ell-|m|}\theta \sin^{|m|}\theta \exp(im\varphi) \tag{2.1-10}$$

where $n = 1,2,3,...,$

$$\ell = \begin{cases} 0,2,4,..., \text{ even parity states,} \\ 1,3,5,..., \text{ odd parity states,} \end{cases} \tag{2.1-11}$$

and λ' and β are nonlinear variational parameters. In the present investigation, we choose to adopt the basis of Eq. (2.1-10) since it contains both symmetries with correct solutions at each limit, can be easily optimized by increasing the basis size and adjusting the nonlinear parameters, and can be completely represented analytically.

Reproduced with permission of the copyright owner. Further reproduction prohibited without permission.

There are many other basis sets and approaches that have been used but are not discussed here since most are similar to one of the above. One exception is the Hamiltonian matrix method of Garstang and Kemic [2,3]. While a basis set of field-free hydrogenic functions is used, Garstang and Kemic do not minimize the energy but instead construct a matrix of expectation values for the Hamiltonian of Eq. (2.1-1) which is truncated to some cutoff value n_c. The matrix then gives approximate eigenvalues and eigenfunctions for all states (below the cutoff). They choose $n_c = 9$ and obtain results for $n \leq 6$ and $B \leq 20$ MG. While this is a Rayleigh variational method and should in principle work at higher field strengths, it does not give the precision obtainable from a minimalization procedure. For example, as will be shown later, their transition wavelengths agree at best to within only 0.4 nm of the current work.

2.1.2. Method of Calculation and Results

It is well known that the time-independent Schrödinger equation with the Hamiltonian given by Eq. (2.1-1) is not completely separable. Only the φ-dependence can be removed hence giving the only "good" quantum number m with the exception of the z-parity. The problem remaining is a coupled set of second-order ordinary differential equations in r and θ.

We chose to use the Ritz variational method which requires matrix elements of the Hamiltonian. The effect of the kinetic energy operator in Eq. (2.1-1) on the basis function (2.1-10) can be obtained analytically. The necessary matrix elements in Eq. (2.1-4) are then of the form

$$\int_0^{\pi} \cos^{\ell'}\theta \sin^{m'}\theta d\theta \int_0^{\infty} r^{n'} \exp(-\lambda' r - \beta r^2 \sin^2\theta) dr \qquad (2.1\text{-}12)$$

which can be obtained by multiple Gauss quadrature [70]. Laguerre polynomials were used to evaluate the inner r-integral and Legendre polynomials for the outer θ-integral. The resulting Hamiltonian matrix was then diagonalized with the EISPACK

Reproduced with permission of the copyright owner. Further reproduction prohibited without permission.

subroutine RSG.

The typical procedure requires a guess for λ' and β and the choice of a starting basis size for a particular B. The integrals in Eq. (2.1-12) are evaluated and the Hamiltonian matrix is diagonalized to obtain the eigenvalues and expansion coefficients. The above is repeated twice for different but similar values of the variational parameters. Though RSG gives the full spectrum of eigenvalues, we must concentrate on a particular $n\ell m$-state for the minimalization. A downhill simplex method [71] is then incorporated to minimize energy $E_{\rm NR}^{\infty}$ by varying λ' and β until convergence. The three sets of $(E_{\rm NR}^{\infty}, \lambda', \beta)$ are supplied as initial guesses. The above procedure is repeated for incremental increases in basis size until convergence.

Results for typical states at various field strengths are given in Table 2.1-1 with comparison to some previous calculations. The present results generally converge to an accuracy better than or equal to the previous computations. Though the basis sizes of our calculations are greater than those of Ref. [20], we are always smaller than Chen and Goldman [37,38] who use the same basis functions but appear to incorporate 50 terms. Also, Rösner et al. [20] use an adapted multiconfiguration Hartree-Fock code which is presumably more computationally expensive. Comparison to Xi et al. [35] is difficult since they use a B-spline basis, but require over 500 terms.

Even as $B \rightarrow 0$ some states remain admixtures of degenerate field-free levels. For example, the "$4p_0$" and "$4f_0$" states are mixtures of hydrogenic $4p_0$ and $4f_0$ levels and are labeled by the dominant level contribution with a "prime," i.e., $|4p_0'\rangle \approx -0.811|4p_0\rangle + 0.585|4f_0\rangle$ and $|4f_0'\rangle \approx -0.811|4f_0\rangle - 0.585|4p_0\rangle$. Tables of approximate mixing coefficients are given in Garstang and Kemic [2]. These are naturally obtained in our computation by requiring the starting basis size to be large enough to have the flexibility of incorporating both levels in the variational calculation.

This mixing increases the difficulty of eigenvalue convergence by adding additional states to a symmetry. For example, the $5p_0'$ is the sixth eigenvalue and not

Reproduced with permission of the copyright owner. Further reproduction prohibited without permission.

TABLE 2.1-1. Some nonrelativistic infinite proton mass energies of hydrogen in a magnetic field for $m_s = -\frac{1}{2}$.

State	B (au)	$-E_{NR}^{\infty}$ (au)			
$n\ell_m\pi$		Ref. [20]	Refs. [37,38][a]	Ref. [35][b]	Present results
$1s+$	2.0×10^{-4}	0.500100(1)[c]	-	0.50009999	0.5000999900000(1)[c]
	2.0×10^{-3}	0.500994(1)	-	0.500999	0.5009990000442(8)
	2.0×10^{-2}	0.509900(2)	-	0.509900045	0.5099000440894(8)
	0.1	0.5475265(3)	0.5475264804	-	0.547526480401(21)
	1.0	0.831169(7)	0.83116889673	0.83116889	0.83116889(28)
	2.0	1.022214(11)	1.02221390766	1.02221285	1.022214(24)
$2s+$	2.0×10^{-4}	0.12509985(1)	-	-	0.12509986000024(2)
	2.0×10^{-3}	0.1259860(2)	-	-	0.125986002548(8)
	1.0×10^{-2}	0.1296516(2)	0.129651571	-	0.129651571358(15)
	2.0×10^{-2}	0.1336242(3)	-	-	0.133624177535(24)
	0.1	0.1480892(7)	0.148089156	-	0.14808916(28)
$2p_0-$	2.0×10^{-4}	0.12509995(1)	-	0.12509994	0.1250999400000612(1)
	1.0×10^{-3}	0.1254985(1)	0.1254985000	0.12549850	0.1254985000420(6)
	2.0×10^{-3}	0.125994(1)	-	0.12599400	0.125994000671 7(8)
	1.0×10^{-2}	0.1298504(2)	0.1298504158	0.12985042	0.1298504158325(12)
	2.0×10^{-2}	0.13440645(3)	-	0.134406465	0.1344064660(15)
	0.1	0.1624101(6)	0.1624100784	0.16241008	0.1624100789(30)
	0.2	0.1851840(8)	-	0.18518404	0.18518404(24)
$2p_{-1}+$	2.0×10^{-4}	0.1251999(1)	-	-	0.1251998800002(1)
	2.0×10^{-3}	0.1269880(2)	-	-	0.12698800185(8)
	2.0×10^{-2}	0.1438176(3)	-	-	0.143817610348(21)
	0.1	0.20084567(5)	0.20084567237	-	0.2008456724(32)
	0.2	0.2505391(7)	-	-	0.2505391(24)
$3d_0'+$	2.0×10^{-4}	0.05565535(2)	-	-	0.0556553486978(12)
	2.0×10^{-3}	0.05653489(3)	-	-	0.0565348858464(18)
	2.0×10^{-2}	0.06361695(5)	-	-	0.06361693547(45)
	0.1	0.074938(12)	-	-	0.074938(40)
$3d_{-1}-$	2.0×10^{-4}	0.0557552(1)	-	-	0.055755195559(6)
	2.0×10^{-3}	0.0575196(3)	-	-	0.057519594775(24)
	2.0×10^{-2}	0.07225355(4)	-	-	0.072253547538(24)
	0.1	0.1078121(8)	-	-	0.10781210(18)
$4p_0'-$	2.0×10^{-4}	0.03134845(2)	-	-	0.031348454156(12)
	2.0×10^{-3}	0.03209659(4)	-	-	0.03209658635(18)
	1.0×10^{-2}	0.03291787(5)	-	-	0.0329178768(36)

[a]Typically 50 terms of the basis (2.1-10) are used.

[b]Typically 500 B-spline functions are used.

[c]The number in parenthesis gives the basis size.

Reproduced with permission of the copyright owner. Further reproduction prohibited without permission.

the fourth of the p_0 symmetry since the eigenvalues are, in decreasing binding energy, $2p_0$, $3p_0$, $4f_0'$, $4p_0'$, $5f_0'$, $5p_0'$, ... This problem becomes acute for high-lying levels in the intermediate-field regime as was experienced by Rösner et al. [20] who obtain convergence to only two figures for $4p_0'$ near $B = 10^{-2}$ using basis set (2.1-7). They have made improvements to six figures by increasing the basis size to give matrices of $\sim 6000 \times 6000$ using a Cray 1 supercomputer [72]. The present results are obtained with the computational resources of IBM RS/6000-type workstations only. The reported number of significant figures reflects our converged accuracy.

Appendix A contains a more extensive list of energies. The new results are presented for fields applicable to magnetic white dwarfs and are given for a finer grid of field strengths than previously. In particular, values for $n = 6$ states are given for the first time.

2.1.3. Nuclear Mass and Charge Scaling

The nuclear mass is set to infinity for computational convenience, but does not represent the physical situation. In field-free calculations, the infinite nuclear mass energies are corrected by multiplication of the reduced mass $\mu = m_N m_e/(m_N + m_e)$ where m_N and m_e are the nuclear and electron masses, respectively. Pavlov-Verevkin and Zhilinskii [73] have shown that the correction is slightly more complicated in the presence of a magnetic field and give the result

$$E_{NR}(B) = \mu E_{NR}^{\infty}(B/\mu^2) - \frac{B}{m_N}(m + 2m_s). \qquad (2.1\text{-}13)$$

The correction is important for small m_N (i.e., hydrogen), large B, and non-zero m. The binding energy of hydrogen is reduced by 2.7216×10^{-4} at zero-field which is significant compared to the reported accuracy of the previous section. The binding energy will be increased for positive m when $Bm > m_N(\mu - 1)E_{NR}^{\infty}$ neglecting m_s.

Surmelian and O'Connell [74] obtained the following relation for scaling the nuclear charge

Reproduced with permission of the copyright owner. Further reproduction prohibited without permission.

$$E_{\rm NR}^{\infty}(Z,B) = Z^2 E_{\rm NR}^{\infty}(Z=1, B/Z^2), \tag{2.1-14}$$

which is rigorously applicable only to infinite mass energies.

To obtain a scaling relation for both charge and mass, one begins with the Schrödinger equation for the two-particle system in a uniform magnetic field and reduces it to the one-particle, relative motion form [73]. Taking the center of mass momentum to be zero and performing the scale transformation $\mathbf{r}_t = \mu Z \mathbf{r}$ gives the new scaling relation

$$E_{\rm NR}(Z,B) = \mu Z^2 E_{\rm NR}^{\infty}(Z=1, B/\mu^2 Z^2) - \frac{B}{m_{\rm N}}(m + 2m_s). \tag{2.1-15}$$

Equation (2.1-15) reduces to (2.1-13) for $Z = 1$ and to (2.1-14) for $m_{\rm N} = \infty$.

2.1.4. Relativistic Corrections

Relativistic effects on hydrogenlike atoms have been addressed by only a few authors. The early calculations of Lindgren and Virtamo [76,77] applied the adiabatic approximation in intense fields. They obtained a correction which reduces the $1s$ binding energy and showed that it increases with field strength from 5.1×10^{-7} at $B = 2$ to 2.0×10^{-4} at $B = 2000$. The Dirac equation for an electron in the presence of an infinite mass nucleus and external magnetic field has recently been variationally solved by Chen and Goldman [37,38] using basis sets similar to Eq. (2.1-10). Their relativistic correction changes sign from positive to negative below $B \sim 40$. Above $B = 200$ the corrections of Lindgren and Virtamo are in reasonable agreement with the newer calculation, but at $B = 2$ the adiabatic approximation is an order of magnitude too small and the wrong sign.

Since as Chen and Goldman show, the corrections are no larger than 10^{-5} of the ground state energy and smaller for excited states, a perturbational approach would seem appropriate. Treating the problem of the Dirac electron in a Coulomb field, but introducing the magnetic field perturbatively through the general Paschen-Back effect [68], Chen and Goldman obtain for the ground state energy following Rose [78]

Reproduced with permission of the copyright owner. Further reproduction prohibited without permission.

$$E^{\infty}_{\mathrm{R,P},1s} = (\gamma_1 - 1)/\alpha^2 - B(2\gamma_1 + 1)/6$$
$$= -\frac{Z^2}{2} - \frac{\alpha^2 Z^4}{8} - \frac{B}{2} + \frac{\alpha^2 Z^2 B}{6} + \cdots \qquad (2.1\text{-}16)$$

where $\gamma_k = \sqrt{k^2 - (\alpha Z)^2}$ and the second line is given to order α^2. From Eq. (2.1-16), the relativistic correction is

$$\Delta E^{\infty}_{\mathrm{R,P},1s} = -\frac{1}{2}(\alpha Z^2)\frac{Z^2/4 - B/3}{Z^2/2 + B/2}|E^{\infty}_{\mathrm{NR}}(Z)| \qquad (2.1\text{-}17)$$

They also obtained the $2p_{-1}$ ($j = \frac{3}{2}, m_j = -\frac{3}{2}$) energy

$$E^{\infty}_{\mathrm{R,P},2p_{-1}} = (\gamma_2/2 - 1)/\alpha^2 - B(2\gamma_2 + 1)/5$$
$$= -\frac{Z^2}{8} - \frac{\alpha^2 Z^4}{128} - B + \frac{\alpha^2 Z^2 B}{10} + \cdots \qquad (2.1\text{-}18)$$

and the relativistic correction

$$\Delta E^{\infty}_{\mathrm{R,P},2p_{-1}} = -\frac{1}{2}(\alpha Z^2)\frac{Z^2/64 - B/5}{Z^2/8 + B/2}|E^{\infty}_{\mathrm{NR}}(Z)|. \qquad (2.1\text{-}19)$$

From Rose, one can determine the energy for the $2s$ ($j = \frac{1}{2}, m_j = -\frac{1}{2}$) state as

$$E^{\infty}_{\mathrm{R,P},2s} = W_{21}/\alpha^2 - \frac{B}{3}\frac{W_{21}}{\alpha Z}(2W_{21} + 1)(1 - W_{21}^2)^{\frac{1}{2}}$$
$$= -\frac{Z^2}{8} - \frac{5\alpha^2 Z^4}{128} - \frac{B}{2} + \frac{\alpha^2 Z^2 B}{24} + \cdots \qquad (2.1\text{-}20)$$

where $W_{21} = \sqrt{(1 + \gamma_1)/2}$. The relativistic correction is then

$$\Delta E^{\infty}_{\mathrm{R,P},2s} = -\frac{1}{2}(\alpha Z^2)\frac{5Z^2/64 - B/12}{Z^2/8 + B/2}|E^{\infty}_{\mathrm{NR}}(Z)|. \qquad (2.1\text{-}21)$$

These relations begin to diverge from the variational results of Chen and Goldman for $B \gtrsim 10^{-2}$ as shown in Table 2.1-2. Though both methods incorporate the Dirac electron, i.e. relativistic corrections to all orders, the above relations only treat the field dependence perturbatively and as a result it is no surprise that they break down for strong fields. Below we try an alternative approach which treats the relativistic corrections to the electron perturbatively to first order, but variationally includes the field dependence by incorporating the wave functions determined in Sec. 2.1.2.

Reproduced with permission of the copyright owner. Further reproduction prohibited without permission.

TABLE 2.1-2. Relativistic infinite proton mass corrections for hydrogen in a magnetic field. Comparison of variational solutions of the Dirac equation for Coulomb and magnetic fields [37,38], exact Dirac electron in a Coulomb field with perturbative treatment of the magnetic field, and the present calculation of Pauli approximation corrections with the magnetic field treated variationally.

State	B(au)	$E_{\rm NR}^{\infty}$ (au)	$\Delta E_{\rm R}^{\infty}$ (10^{-6} au)		
$n\ell_m(jm_j)$			Refs. [37,38]	Eqs. (2.1-17)-(2.1-21)	Present Results
$1s\ (\frac{1}{2},-\frac{1}{2})$	0	-0.500000000	-6.6565975	-6.6564202	-6.6564202
	10^{-2}	-0.5049750028	-6.569601	-6.5673429	-6.657529
	0.1	-0.5475264804	-5.92794	-5.742953	-6.803989
	1	-0.831168896	-4.3290	1.844263	-15.26919
$2s\ (\frac{1}{2},-\frac{1}{2})$	0	-0.12500000	-	-2.0801313	-2.0801313
	10^{-2}	-0.1296515714	-2.074	-2.052428	-2.09338
	5×10^{-2}	-0.1420167205	-2.236	-1.8644	-2.3602
	0.1	-0.14808916	-2.577	-1.5725	-2.9035
	0.2	-0.148986678	-2.905	-1.0835	-3.699
	0.5	-0.150807855	-2.292	-0.3904	
	1	-0.160468983	-2.086	0.0356	
$2p_0\ (\frac{1}{2},-\frac{1}{2})$	0	-0.12500000	-	-2.0801313	-2.0801313
	10^{-2}	-0.1298504158	-0.9479	-	-2.08566
	0.1	-0.1624100789	-0.9740	-	-2.48349
$2p_{-1}\ (\frac{3}{2},-\frac{3}{2})$	0	-0.12500000	-	-0.4160263	-0.4160263
	0.1	-0.2008456724	-0.225	0.10398	-0.79511

Reproduced with permission of the copyright owner. Further reproduction prohibited without permission.

2.1.4.1. Relativistic Kinetic Energy

The nonrelativistic infinite nuclear mass Hamiltonian Eq. (2.1-1) neglects the term

$$H_{\mathrm{KE}} = -\frac{\alpha^2}{8}\nabla^4 \tag{2.1-22}$$

which can be obtained from the Pauli approximation (to order α^2) of the Dirac equation for an electron in a potential V_{C} [75]. Utilizing Eq. (2.1-1), Eq. (2.1-22) can be written

$$\begin{aligned} H_{\mathrm{KE}} &= -\frac{\alpha^2}{2}T^2 \\ &= -\frac{\alpha^2}{2}\left[H_o + \frac{Z}{r} - B\left(\frac{m}{2} + m_s\right) - \frac{B^2}{8}r^2\sin^2\theta\right]^2 \end{aligned} \tag{2.1-23}$$

or

$$\begin{aligned} H_{\mathrm{KE}} = -\frac{\alpha^2}{2}\Big[&{H_o}^2 + \frac{Z^2}{r^2} + \frac{B^2}{4}(m+2m_s)^2 + \frac{B^4}{64}r^4\sin^4\theta \\ &+ Z(H_o\frac{1}{r} + \frac{1}{r}H_o) - BH_o(m+2m_s) - \frac{B^2}{8}(H_o r^2\sin^2\theta + r^2\sin^2\theta H_o) \\ &- ZB(m+2m_s)\frac{1}{r} - \frac{ZB^2}{4}r\sin^2\theta + \frac{B^3}{8}(m+2m_s)r^2\sin^2\theta\Big]. \end{aligned} \tag{2.1-24}$$

Since, H_o is Hermitian and $\langle H_o\rangle = E^{\infty}_{\mathrm{NR}}$, the expectation value of Eq. (2.1-24) gives

$$\begin{aligned} \Delta E^{\infty}_{\mathrm{KE}} = -\frac{Z^4\alpha^2}{2}\Bigg\{&\left[(E^{\infty}_{\mathrm{NR}})^2 + 2E^{\infty}_{\mathrm{NR}}\left\langle\psi\left|\frac{1}{r}\right|\psi\right\rangle + \left\langle\psi\left|\frac{1}{r^2}\right|\psi\right\rangle\right] \\ &- B(m+2m_s)\left[E^{\infty}_{\mathrm{NR}} + \left\langle\psi\left|\frac{1}{r}\right|\psi\right\rangle\right] \\ &+ \frac{B^2}{4}\left[(m+2m_s)^2 - \langle\psi|r\sin^2\theta|\psi\rangle - E^{\infty}_{\mathrm{NR}}\langle\psi|r^2\ sin^2\theta|\psi\rangle\right] \\ &+ \frac{B^3}{8}(m+2m_s)\langle\psi|r^2\ sin^2\theta|\psi\rangle + \frac{B^4}{64}\langle\psi|r^4\sin^4\theta|\psi\rangle\Bigg\}, \end{aligned} \tag{2.1-25}$$

where the energies and expectation values depend on B but are for $Z = 1$. For $B = 0$, Eq. (2.1-25) reduces to Eq. (16.4-9) of Ref. [75] given by

$$\Delta E^{\infty}_{\mathrm{KE}} = -\frac{Z^4\alpha^2}{2}\left[(E^{\infty}_{\mathrm{NR}})^2 + 2E^{\infty}_{\mathrm{NR}}\left\langle\psi\left|\frac{1}{r}\right|\psi\right\rangle + \left\langle\psi\left|\frac{1}{r^2}\right|\psi\right\rangle\right] \tag{2.1-26}$$

Reproduced with permission of the copyright owner. Further reproduction prohibited without permission.

or

$$\Delta E_{\rm KE}^{\infty} = -\frac{Z^4\alpha^2}{2n^3}\left[-\frac{3}{4n} + \frac{1}{l+\frac{1}{2}}\right]. \tag{2.1-27}$$

2.1.4.2. Spin-Orbit Coupling

The Hamiltonian of Eq. (2.1-1) also neglects the spin-orbit interaction term

$$\begin{aligned} H_{\rm SO} &= -\frac{\alpha^2}{4}\sigma \cdot \nabla V_{\rm C} \times \mathbf{p} \\ &= \zeta(r)\mathbf{L}\cdot\mathbf{S} \end{aligned} \tag{2.1-28}$$

where $\zeta(r) = Z\alpha^2/2r^3$. Since the total angular momentum $\mathbf{J} = \mathbf{L} + \mathbf{S}$, $\mathbf{L}\cdot\mathbf{S} = \frac{1}{2}(J^2 - L^2 - S^2)$. The matrix element of Eq. (2.1-28) which does not depend explicitly on B is then given by

$$\Delta E_{\rm SO}^{\infty} = \frac{Z^4\alpha^2}{4}\left\langle\psi\left|\frac{j(j+1) - \ell(\ell+1) - s(s+1)}{r^3}\right|\psi\right\rangle, \tag{2.1-29}$$

where $j = \ell \pm s$. Equation (2.1-29) is non-zero for s-states with $B > 0$ since they will have d,g, ...-wave contributions. In addition, ψ which consists of the uncoupled representation basis expansion (2.1-10) will give off-diagonal matrix elements for the $\mathbf{L}\cdot\mathbf{S}$ operator. When $B = 0$, Eq. (2.1-29) reduces to Eq. (16.3-17) of Ref. [75] given by

$$\Delta E_{\rm SO}^{\infty} = \frac{Z^4\alpha^2}{4}\frac{1}{n^3(\ell+1)(\ell+\frac{1}{2})\ell}\begin{cases} \ell/2, & j = \ell + 1/2 \\ -\frac{1}{2}(\ell+1), & j = \ell - 1/2. \end{cases} \tag{2.1-30}$$

2.1.4.3. The Darwin Term

The final correction is due to the neglected Hamiltonian term

$$\begin{aligned} H_{\rm D} &= \frac{\alpha^2}{8}\nabla\cdot\mathbf{E} \\ &= -\frac{Z\alpha^2}{8}\nabla^2\left(\frac{1}{r}\right) \end{aligned} \tag{2.1-31}$$

for which the matrix element is

Reproduced with permission of the copyright owner. Further reproduction prohibited without permission.

$$\Delta E_{\rm D}^{\infty} = \frac{Z^4\alpha^2}{2}|\psi(r=0,Z=1,B)|^2. \tag{2.1-32}$$

This correction is non-zero for s-states only. It reduces to

$$\Delta E_{\rm D}^{\infty} = \frac{Z^4\alpha^2}{2n^3} \tag{2.1-33}$$

for $B = 0$ which is Eq. (16.4-22) of Weissbluth [75].

2.1.4.4. Results and Discussion

The total relativistic correction is then given by

$$\Delta E_{\rm R}^{\infty} = \Delta E_{\rm KE}^{\infty} + \Delta E_{\rm SO}^{\infty} + \Delta E_{\rm D}^{\infty}. \tag{2.1-34}$$

Some results for the total correction are presented in Table 2.1-2 with comparisons to the Dirac-variational computations of Chen and Goldman [37,38] and the relativistic perturbational Eqs. (2.1-17) to (2.1-21). The present calculations appear to be diverging from both the Chen and Goldman values and the perturbational results. Our corrections always give increased binding with field strength while the perturbational values always decrease the binding energy with increasing field strength. One can see this will always be true by noting the field dependent relativistic correction term, the fourth term of the second line of Eq. (2.1-16) for the $1s$ for example, is positive. For our corrections, the first order term in B of Eq. (2.1-27) is dominant and gives an increasing negative contribution. While the Darwin term and the zeroth order term of Eq. (2.1-27) give increasing positive contributions with field strength, they cannot offset the first order B term. The spin-orbit contribution for s-states is negligible. Taking the Chen and Goldman results as "exact", it appears that the present formulation can only give the relativistic correction to about one significant figure up to $B = 0.5$. A more extensive tabulation is given in Appendix B including data for each of the three individual contributions.

According to Eqs. (2.1-25), (2.1-29), and (2.1-32), the total relativistic correction scales as Z^4 for hydrogenlike ions, but this correction is only the leading term to

Reproduced with permission of the copyright owner. Further reproduction prohibited without permission.

TABLE 2.1-3. Z-scaling of relativistic infinite proton mass corrections for the ground state of hydrogenlike atoms in a magnetic field from variational solutions of the Dirac equation from Refs. [37,38] and present corrections compared to direct Dirac-variational solutions.

Z	B(au)	$-E_{\rm NR}^{\infty}$ (au)	$-\Delta E_{\rm R}^{\infty}$ (au)		
			$-\Delta E_{\rm R}^{\infty}(Z)$ Refs. [37,38]	$-Z^4\Delta E_{\rm R}^{\infty}(Z=1)$ Refs. [37,38]	$-Z^4\Delta E_{\rm R}^{\infty}(Z=1)$ Present Results
1	0	0.5000	6.6565975×10^{-6}	6.6565975×10^{-6}	6.6564202×10^{-6}
20	0	200.000	1.0765234	1.0650556	1.065027232
40	0	800.000	17.8074978	17.0408896	17.04043571
92	0	4232.000	629.198023	476.873959	476.861257
1	1	0.8311688967	4.3290×10^{-6}	4.3290×10^{-6}	1.527×10^{-5}
5	25	20.7792224	2.707475×10^{-3}	2.7056×10^{-3}	9.543×10^{-3}
1	2	1.022139	4.121×10^{-6}	4.121×10^{-6}	-
5	50	25.55534768	2.577475×10^{-3}	2.576×10^{-3}	-
20	800	408.8855628	0.6662508	0.6594	-

Reproduced with permission of the copyright owner. Further reproduction prohibited without permission.

α^2 from the Pauli approximation of the Dirac equation. Chen and Goldman [37,38] evaluated explicitly the relativistic corrections for a particular nuclear charge Z. In Table 2.1-3 we compare how well the Z^4-scaling holds for the present corrections and the $Z = 1$ Dirac-variational corrections. The Z^4-scaling is accurate to three significant figures for $Z < 20$ at $B = 0$. For $B > 0$, the Chen and Goldman results can be scaled up to $B < 2$ for $Z < 20$ to two significant figures. The present corrections which do not agree well with the Chen and Goldman results at $B = 1$ and $Z = 1$, also do not scale well. It maybe necessary to include the next order term in α to obtain a better Z-scaling.

2.1.5. Radiative Transitions

Transition strengths have not been as thoroughly investigated by previous authors as the binding energies. An extensive tabulation of wavelengths, dipole strengths, oscillator strengths, and transition probabilities is given in Forster et al. [21] for $n \leq 3$, addition transition data is given in Wunner et al. [22,72], Garstang and Kemic [2,3], Smith et al. [8], Brandi et al. [13], and Kara and McDowell [16]. Henry and O'Connell [12] give the transition wavelengths graphically, but apparently the probabilities are unpublished. Below we give some definitions and relations for computing transition results.

The length form of the electric-dipole (E1) transition operator between initial state ψ_a and final state ψ_b with binding energies E_a and E_b, respectively, is given by the familiar

$$\mathbf{D}^{\mathrm{L}}_{ab} = \langle \psi_b | \mathbf{r} | \psi_a \rangle \tag{2.1-35}$$

even in the presence of a magnetic field [8], while the velocity form

$$\mathbf{D}^{\mathrm{V}}_{ab} = \frac{-\langle \psi_b | \nabla | \psi_a \rangle + \frac{i}{2} \langle \psi_b | \mathbf{B} \times \mathbf{r} | \psi_a \rangle}{E_{ab}} \tag{2.1-36}$$

has been found by Smith et al. [8] to contain an additional magnetic-field-dependent term. The transition energy $E_{ab} = E_a - E_b$ and $\mathbf{r}$ is the position vector of the

Reproduced with permission of the copyright owner. Further reproduction prohibited without permission.

electron with respect to the origin. Equation (2.1-36) can be obtained by introducing the uniform external magnetic field into the usual semiclassical formulation of the interaction of an atom with a classical radiation field [79]. We derive the new, more convenient velocity form

$$\mathbf{D}^{\mathrm{V}}_{\mathrm{ab}} = \frac{-\langle\psi_{\mathrm{b}}|\nabla|\psi_{\mathrm{a}}\rangle}{E_{\mathrm{ab}} - \frac{B}{2}(m_{\mathrm{b}} - m_{\mathrm{a}})} \tag{2.1-37}$$

as well as the new acceleration form

$$\mathbf{D}^{\mathrm{A}}_{\mathrm{ab}} = \frac{Z\langle\psi_{\mathrm{b}}|\frac{\mathbf{r}}{r^3}|\psi_{\mathrm{a}}\rangle + \frac{B^2}{4}[\langle\psi_{\mathrm{b}}|\mathbf{r}\sin^2\theta|\psi_{\mathrm{a}}\rangle + \langle\psi_{\mathrm{b}}|r\sin\theta\cos\theta\hat{\theta}|\psi_{\mathrm{a}}\rangle]}{E_{\mathrm{ab}}[E_{\mathrm{ab}} - \frac{B}{2}(m_{\mathrm{b}} - m_{\mathrm{a}})]}, \tag{2.1-38}$$

where m_{a} and m_{b} are the magnetic quantum numbers of states ψ_{a} and ψ_{b}, respectively.

The absorption oscillator strength is defined as

$$f_{\mathrm{ba}} = \frac{2}{3}E_{\mathrm{ab}}|\mathrm{D}_{\mathrm{ab}}|^2, \tag{2.1-39}$$

while the transition probability is given by

$$A_{\mathrm{ab}} = \frac{4}{3}\alpha^3 E^3_{\mathrm{ab}}|\mathbf{D}_{\mathrm{ab}}|^2. \tag{2.1-40}$$

Hasegawa and Howard [80] obtained the oscillator strength sum-rule

$$\sum_{\mathrm{b}} f_{\mathrm{ba}} = 1 + (m_{\mathrm{b}} - m_{\mathrm{a}})m_{\mathrm{a}} + \frac{B}{2}(m_{\mathrm{b}} - m_{\mathrm{a}})\langle\psi_{\mathrm{b}}|r^2\sin^2\theta|\psi_{\mathrm{a}}\rangle. \tag{2.1-41}$$

We derive the new, more convenient sum-rule

$$\sum_{\mathrm{b}} \frac{\left[E_{\mathrm{ab}} - \frac{B}{2}(m_{\mathrm{b}} - m_{\mathrm{a}})\right] f_{\mathrm{ba}}}{E_{\mathrm{ab}}} = 1. \tag{2.1-42}$$

Forster et al. [21] give the scaling relations for nuclear charge

$$D_{\mathrm{ab}}(Z, B) = Z^{-1}D_{\mathrm{ab}}(Z = 1, B/Z^2) \tag{2.1-43}$$

and

$$A_{\mathrm{ab}}(Z, B) = Z^4 A_{\mathrm{ab}}(Z = 1, B/Z^2). \tag{2.1-44}$$

Reproduced with permission of the copyright owner. Further reproduction prohibited without permission.

The oscillator strength is independent of Z. Wunner et al. [81] give the nuclear mass scaling relations, but these are not usually applied since the correction is on the order of the computational uncertainties.

2.1.5.1. Results and Discussion

We have determined transition data from the wave functions obtained in Sec. 2.1.2 using the basis of Eq. (2.1-10). Typical examples of transition probabilities are given in Table 2.1-4 with comparison to some previous calculations. The new results agree with the calculations of Forster et al. [21] to within their quoted accuracy of four figures. The earlier calculations of Kemic [3], Smith et al. [8], Brandi et al. [13], and Kara and McDowell [16] are not as accurate, but generally agree with the new computation. Due to the difficulty in obtaining accurate relativistic corrections to the energies as discussed in Sec. 2.1.4, the wavelengths include only finite nuclear mass corrections and therefore are reliable to only six significant figures.

Considerable pain was taken to ensure the convergence of the present results. Transition data were evaluated for different basis sizes and all three forms of the dipole operator. Convergence in the oscillator strength sum rules and amount of basis set cancellation were also checked. Table 2.1-5 gives some typical examples of the quality of basis set convergence.

A tabulation of transition wavelengths, dipole strengths, oscillator strengths, and transition probabilities for many spin-allowed transitions in hydrogen is given in Appendix C. Appendix D contains some corresponding results for the hydrogenlike ion He^+. Figures 2.1-1 and 2.1-2 display the wavelengths of the H I and He II Lyα components, respectively.

Reproduced with permission of the copyright owner. Further reproduction prohibited without permission.

TABLE 2.1-4. Comparison of hydrogen transition probabilities and wavelengths in a magnetic field to previous calculations. The finite proton mass correction is included.

Transition	B (au)	$A(10^8\ s^{-1})$ / λ (Å)				
		Ref. [8]	Ref. [16]	Refs. [13,3]	Ref. [21]	Present results
$1s-2p_0$	4.254×10^{-3}	6.27	6.27	6.17	-	6.261131
	(10 MG)	1210.8	-	-	-	1215.611
	0.02	-	-	-	6.324	6.3238
		-	-	-	1214	1214.09
	4.254×10^{-2}	6.55	6.5	6.44	-	6.5341
	(100 MG)	1204.0	-	-	-	1208.77
	0.1	-	-	-	7.430	7.433
		-	-	-	1184	1183.75
$1s-2p_1$	4.254×10^{-3}	6.39	6.37	6.27	-	6.3715
		1203.9	-	-	-	1208.68
	0.02	-	-	-	6.918	6.9178
		-	-	-	1181	1180.82
	4.254×10^{-2}	8.06	7.93	7.94	-	8.03555
		1132.7	-	-	-	1137.10
	0.1	-	-	-	12.35	12.353
		-	-	-	1021	1020.72
$1s-2p_{-1}$	4.254×10^{-3}	6.18	6.17	6.06	-	6.1585
		1217	-	-	-	1222.45
	0.02	-	-	-	5.898	5.89803
		-	-	-	1245	1245.26
	4.254×10^{-2}	5.76	5.69	5.63	-	5.7405
		1267	-	-	-	1271.92
	0.1	-	-	-	5.780	5.780
		-	-	-	1315	1314.78
	0.2	-	-	-	5.979	5.97905
		-	-	-	1341	1341.02
$2p_0-3d_{-1}$	4.254×10^{-3}	0.279	0.304	0.299	-	0.298
		6731.9	-	6758.7	-	6755.10
	0.02	-	-	-	0.2386	0.2386
		-	-	-	7334	7333.50
	4.254×10^{-2}	0.198	0.172	0.197	-	0.197
		7807.1	-	7946.6	-	7834.24

Reproduced with permission of the copyright owner. Further reproduction prohibited without permission.

$2p_0 - 3d_0$	4.254×10^{-3}	0.437	-	-	-	0.4357398
		6532.8	-	-	6558.4	6558.450003
	0.02	-	-	-	-	0.459773
		-	-	-	-	6439.95905
	4.254×10^{-2}	0.518	-	-	-	0.514392
		6095.1	-	-	6085.8	6120.540
	0.1	-	-	-	-	0.60131
		-	-	-	-	5211.7
$2s - 2p_0$	4.254×10^{-3}	9.05-11	8.46-11	3.12-6	-	9.1019-11
		1.2583+7	-	-	-	1.26069+7
	0.02	-	-	-	9.237-7	9.2388-7
		-	-	-	5.828+5	5.82754+5
	4.254×10^{-2}	7.05-5	6.50-5	1.77-4	-	7.075259-5
		1.3739+5	-	-		1.3766323+5
	0.1	-	-	-	6.024-3	6.02418-3
		-	-	-	3.183+4	3.1833261+4

Reproduced with permission of the copyright owner. Further reproduction prohibited without permission.

TABLE 2.1-5. Convergence properties of hydrogen transition probabilities in a magnetic field for various basis sizes.

B (au)	$1s$		$2p_0$		$A(10^8\ s^{-1})$	Cancellation[b]	f-sum Eq. (2.1-42)	Dipole Form[c]
	N_n[a]	N_l	N_n	N_l				
0	1	1	1	1	6.25808580	1.000000	-	L,V,A
	1	1	16	1	6.25808580	0.999994	1.000000	L
					6.25808580	0.999998	1.000000	V
					6.25808580	1.000000	1.010213	A
4.254×10^{-3}	4	1	4	3	6.26107272	0.999269	0.9455173	L
					6.26114302	0.999560	0.98916	V
					6.26113253	0.999855	1.20561	A
	5	3	4	5	6.26113107	0.99917	0.945517	L
					6.26113104	0.99953	0.983976	V
					6.26113077	0.99983	1.205606	A
	5	3	5	4	6.26113105	0.999168	0.979014	L
					6.26113106	0.999552	0.996562	V
					6.26113116	0.999831	1.142353	A
	5	3	6	5	6.26113105	0.99917	0.992341	L
					6.26113105	0.999515	0.999330	V
					6.26113103	0.99985	1.088363	A
2.0×10^{-2}	5	3	4	4	6.32380241	0.978616	0.948122	L
					6.32380153	0.987343	0.984949	V
					6.32378998	0.99592	1.19996	A
	5	3	5	3	6.32380214	0.85475	0.97289	L
					6.32380192	0.88541	0.99464	V
					6.32379220	0.94231	1.15461	A
	5	3	6	3	6.32380191	0.930225	0.991429	L
					6.32380211	0.947132	0.999179	V
					6.32379810	0.974396	1.091280	A
4.254×10^{-2}	5	3	6	3	6.53415888	0.862894	0.992587	L
					6.53415973	0.919207	0.999311	V
					6.53414084	0.958430	1.081406	A

Reproduced with permission of the copyright owner. Further reproduction prohibited without permission.

	5	3	7	3	6.53415911	0.854815	0.997434	L
					6.53415960	0.906720	0.999875	V
					6.53412942	0.955495	1.048757	A
	5	3	5	4	6.53415876	0.749634	0.995656	L
					6.53415967	0.815375	0.999708	V
					6.53414395	0.904091	1.061540	A
0.1	5	3	6	3	7.43273113	0.758149	0.997675	L
					7.43274983	0.895996	0.999880	V
					7.43263063	0.952099	1.043072	A
	5	3	7	3	7.43273171	0.417092	0.995042	L
					7.43274950	0.564747	0.999462	V
					7.43267909	0.758904	1.057318	A
	6	3	6	3	7.43274799	0.7940131	0.997675	L
					7.43274834	0.898706	0.999880	V
					7.43263065	0.963356	1.043072	A

[a] N_n and N_ℓ are the number of expansion terms in n and ℓ for the basis (2.1-10). The total basis size is $N_n \times N_\ell$.

[b] A measure of the cancellation is obtained from the ratio of the dipole moment determined by taking the absolute values of the expansion coefficients to the real dipole moment. A ratio of one gives no cancellation.

[c] L=length, V=velocity, and A=acceleration.

Reproduced with permission of the copyright owner. Further reproduction prohibited without permission.

Reproduced with permission of the copyright owner. Further reproduction prohibited without permission.

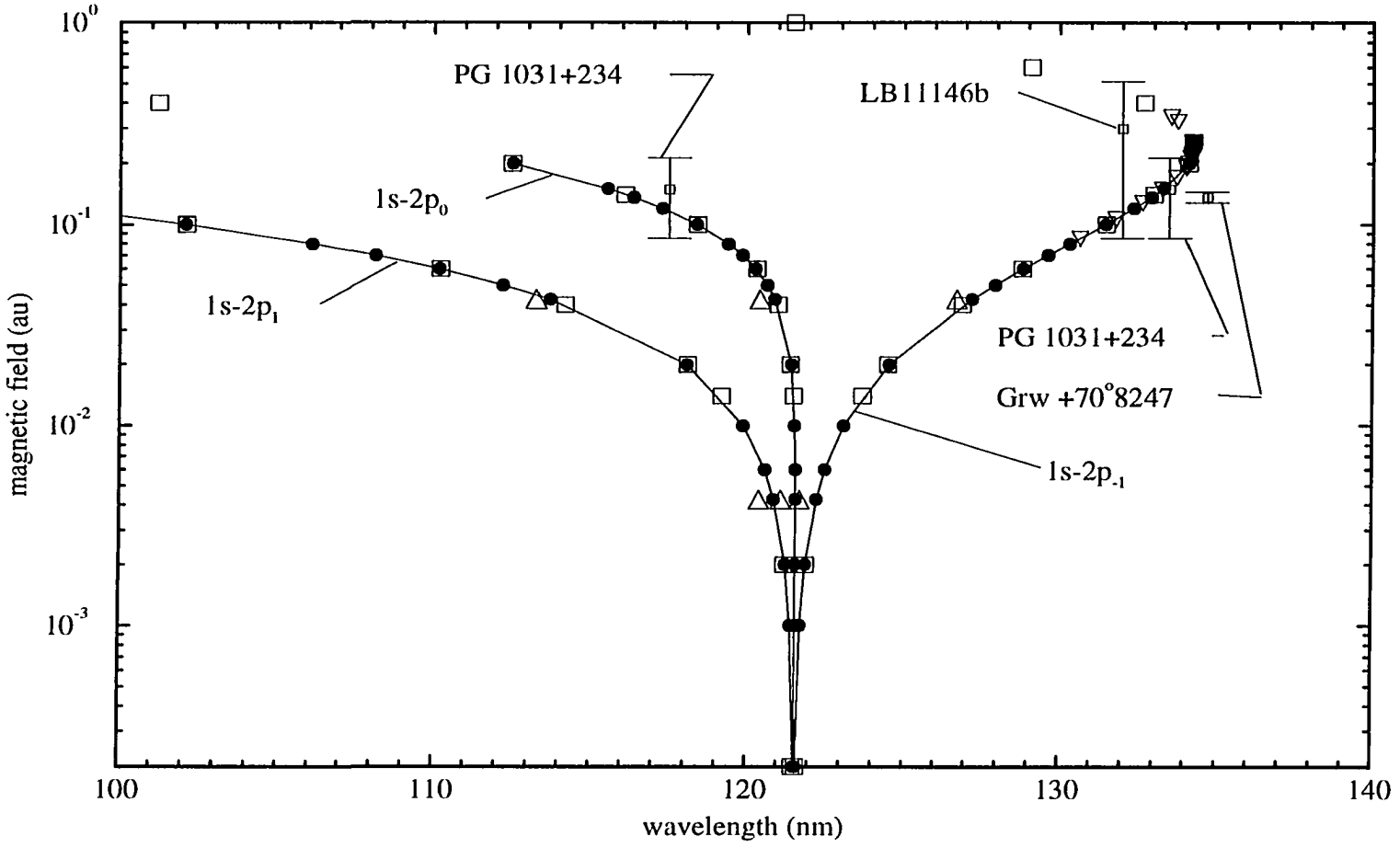

FIG. 2.1-1. Wavelengths of the hydrogen Lyα transitions versus magnetic field. The present results are given by the filled circles, triangles from Ref. [8], upside down triangles from Ref. [11], and squares from Ref. [21]. Magnetic white dwarf observations are shown for comparison.

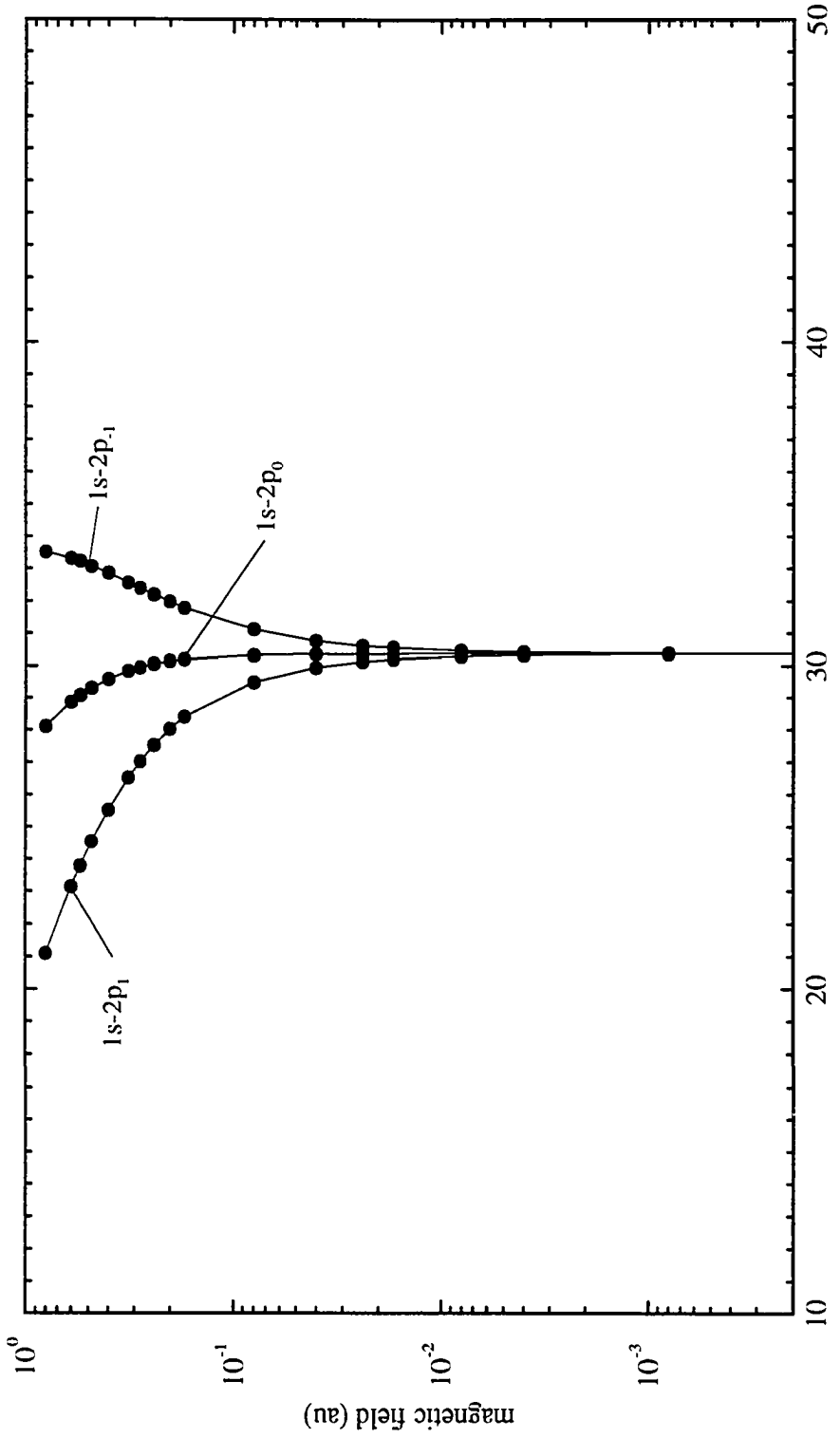

FIG. 2.1-2. Same as FIG. 2.1-1 but for He II.

Reproduced with permission of the copyright owner. Further reproduction prohibited without permission.

2.2. Spontaneous Two-Photon Emission by Hydrogenlike Atoms

The investigation of two-photon processes, and in particular the $2s \rightarrow 1s$ transition for hydrogen and hydrogenlike ions, has been of considerable interest from the beginnings of quantum mechanics to the present day [82–89]. Until recently however, little attention has been given to two-photon processes in strong magnetic fields [66,67].

In this section, the theory of two-photon processes as developed by Shapiro and Breit [85] and Tung et al. [89] along with previously available magnetic-field-dependent energy level values and dipole strengths are used to estimate the spontaneous emission probability for the $2s \rightarrow 1s$ transition of hydrogen and hydrogenlike ions in a uniform magnetic field ranging from 47 to 4.7×10^8 T. Published results from this section can be found in Stancil and Copeland [90].

2.2.1. Theory

The probability per second for spontaneous two-photon emission in the nonrelativistic electric dipole approximation from an arbitrary state $\psi^{m'}_{n'\ell'} = |n'\ell'm'\rangle$ to an arbitrary state $\psi^{m}_{n\ell} = |n\ell m\rangle$ in the frequency range $d\nu_1$ of the first photon with frequency ν_1 is [85]

$$A(\nu_1)d\nu_1 = \frac{2^{10}\pi^6\nu_1^3\nu_2^3}{h^2c^6}\left|\sum_{n''\ell''m''}\left\{\frac{\langle n'\ell'm'|\mathbf{r}\cdot\hat{\mathbf{e}}_1|n''\ell''m''\rangle\langle n''\ell''m''|\mathbf{r}\cdot\hat{\mathbf{e}}_2|n\ell m\rangle}{\nu_{n'\ell'm',n''\ell''m''}+\nu_2}\right.\right.$$
$$\left.\left.+\frac{\langle n'\ell'm'|\mathbf{r}\cdot\hat{\mathbf{e}}_2|n''\ell''m''\rangle\langle n''\ell''m''|\mathbf{r}\cdot\hat{\mathbf{e}}_1|n\ell m\rangle}{\nu_{n'\ell'm',n''\ell''m''}+\nu_1}\right\}\right|^2 d\nu_1, \qquad (2.2\text{-}1)$$

where ν_2 is the frequency of the second photon, $|n''\ell''m''\rangle$ is the intermediate state, $\hat{\mathbf{e}}_1$ is the polarization vector of ν_1, and $\hat{\mathbf{e}}_2$ is the polarization vector of ν_2. The sum over intermediate levels includes the bound as well as the continuum states. The two-photon frequencies are related by

Reproduced with permission of the copyright owner. Further reproduction prohibited without permission.

$$\nu_1 + \nu_2 = \nu_{n'\ell'm',n\ell m}$$

$$\equiv \nu_o, \tag{2.2-2}$$

where ν_o is the total frequency difference between states $|n'\ell'm'\rangle$ and $|n\ell m\rangle$. The total two-photon transition probability is then given by [83]

$$A_{n\ell m,n'\ell'm'} = \frac{1}{2}\int_0^{\nu_o} A(\nu_1)d\nu_1. \tag{2.2-3}$$

We now let

$$A(\nu_1)d\nu_1 = c_1\nu_1^3\nu_2^3 M d\nu_1, \tag{2.2-4}$$

where

$$c_1 = \frac{2^{10}\pi^6}{h^2c^6} \tag{2.2-5}$$

and

$$M = \left| \sum_{n''\ell''m''} \left\{ \frac{\langle n'\ell'm'|\mathbf{r}\cdot\hat{\mathbf{e}}_1|n''\ell''m''\rangle\langle n''\ell''m''|\mathbf{r}\cdot\hat{\mathbf{e}}_2|n\ell m\rangle}{\nu_{n'\ell'm',n''\ell''m''} + \nu_2} + \frac{\langle n'\ell'm'|\mathbf{r}\cdot\hat{\mathbf{e}}_2|n''\ell''m''\rangle\langle n''\ell''m''|\mathbf{r}\cdot\hat{\mathbf{e}}_1|n\ell m\rangle}{\nu_{n'\ell'm',n''\ell''m''} + \nu_1} \right\} \right|^2 \tag{2.2-6}$$

is the effective matrix element.

For $n's \rightarrow ns$ transitions ($\ell' = \ell = m' = m = 0$ and $\ell'' = 1$), we have

$$M = \left| \sum_{n''=2}^{\infty} \sum_{m''=-1}^{1} \left\{ \frac{\langle n'00|\mathbf{r}\cdot\hat{\mathbf{e}}_1|n''1m''\rangle\langle n''1m''|\mathbf{r}\cdot\hat{\mathbf{e}}_2|n00\rangle}{\nu_{n'00,n''1m''} + \nu_2} + \frac{\langle n'00|\mathbf{r}\cdot\hat{\mathbf{e}}_2|n''1m''\rangle\langle n''1m''|\mathbf{r}\cdot\hat{\mathbf{e}}_1|n00\rangle}{\nu_{n'00,n''1m''} + \nu_1} \right\} \right|^2. \tag{2.2-7}$$

At this point we note that previous workers [83] neglected the Zeeman structure and set the matrix elements for individual m-states equal. We must retain the m-state structure here because of the large quadratic Zeeman splitting in the $n''p$ states as a result of the strong magnetic field and the effect the field has on the different m-state dipole strengths. We define in cartesian coordinates the field to be parallel

Reproduced with permission of the copyright owner. Further reproduction prohibited without permission.

to the z-axis, $\mathbf{B} = (0, 0, B)$, and the polarization vector to be $\hat{\mathbf{e}} = (e_x, e_y, e_z)$ which gives the effective matrix element

$$M = \left| \sum_{n''=2}^{\infty} \left\{ Y^{n'00}_{n''1\text{-}1} Y^{n00}_{n''1\text{-}1} \left[\frac{1}{\nu_{n'00,n''1\text{-}1} + \nu_2} + \frac{1}{\nu_{n'00,n''1\text{-}1} + \nu_1} \right] \right.\right.$$
$$+ Z^{n'00}_{n''10} Z^{n00}_{n''10} \left[\frac{1}{\nu_{n'00,n''10} + \nu_2} + \frac{1}{\nu_{n'00,n''10} + \nu_1} \right]$$
$$\left.\left. + X^{n'00}_{n''11} X^{n00}_{n''11} \left[\frac{1}{\nu_{n'00,n''11} + \nu_2} + \frac{1}{\nu_{n'00,n''11} + \nu_1} \right] \right\} \right|^2, \tag{2.2-8}$$

where X, Y, and Z are dipole matrix elements. Since for $\Delta m = 0$ transitions the photon is linearly polarized with the field [68], we define

$$Z^{n'00}_{n''10} \mathbf{e}_z = \langle n'00 | \mathbf{r} \cdot \hat{\mathbf{e}} | n''10 \rangle. \tag{2.2-9}$$

Likewise, for $\Delta m = \pm 1$ transitions the photon is linearly polarized perpendicular to the field so that

$$X^{n'00}_{n''11} \mathbf{e}_x = \langle n'00 | \mathbf{r} \cdot \hat{\mathbf{e}} | n''11 \rangle \tag{2.2-10}$$

and

$$Y^{n'00}_{n''1-1} \mathbf{e}_y = \langle n'00 | \mathbf{r} \cdot \hat{\mathbf{e}} | n''1\text{-}1 \rangle. \tag{2.2-11}$$

For the total two-photon spontaneous emission, we average over all orientations of the polarization. Therefore, we require

$$e_{1_x} e_{2_x} = e_{1_y} e_{2_y} = e_{1_z} e_{2_z} = e_1 e_2, \tag{2.2-12}$$

which gives $\hat{\mathbf{e}}_1 \cdot \hat{\mathbf{e}}_2 = 3 e_1 e_2$.

Defining for Eq. (2.2-8)

$$S_y(B) = \sum_{n''=2}^{\infty} Y^{n'00}_{n''1\text{-}1} Y^{n00}_{n''1\text{-}1} \left[\frac{1}{\nu_{n'00,n''1-1} + \nu_2} + \frac{1}{\nu_{n'00,n''1-1} + \nu_1} \right] \tag{2.2-13}$$

and similarly for S_x and S_z gives

Reproduced with permission of the copyright owner. Further reproduction prohibited without permission.

$$M(B) = |(e_1 e_2)^2|_{\rm avg} |\{S_y(B) + S_z(B) + S_x(B)\}^2|_{\rm avg}$$
$$= \frac{1}{3}\left|\left[\frac{1}{3}\{S_y(b) + S_z(B) + S_x(B)\}\right]^2\right|_{\rm avg}. \qquad (2.2\text{-}14)$$

The sums S_x, S_y, and S_z are functions of the frequencies ν_1, ν_2, and $\nu_{n'00,n''1m''}$ and the dipole matrix elements X, Y, and Z. The matrix elements and $\nu_{n'00,n''1m''}$ are functions of the magnetic field. Therefore, the total transition probability can be written

$$A_{n00,n'00} = \frac{1}{2}\int_0^{\nu_o(B)} A(\nu_1, B)d\nu_1$$
$$= \frac{1}{2}c_1 \int_0^{\nu_o(B)} \nu_1^3(\nu_o(B) - \nu_1)^3 M(\nu_1, B)d\nu_1. \qquad (2.2\text{-}15)$$

Eq. (2.2-1), which leads to Eq. (2.2-15), was derived in Ref. [82] using second-order perturbation theory for an atom interacting with a radiation field, but not with an external, homogeneous magnetic field. The derivation incorporated the standard rotating wave approximation and the assumption that the populations of the intermediate states are much less than that of the final state. It can be shown that both approximations are valid for the application of a magnetic field.

2.2.2 Calculations

Prior to the work performed in Sec. 2.1 the published magnetic-field dependent computations were available over the field range of 47 to 4.7×10^8 T and consist of energy levels with $n \leq 4$, but only dipole transition strengths for $n \leq 3$. Continuum transition calculations are available only for a few field strengths (2000 T [59], 1175-11,750 T [60], 2.35×10^7 T, and 4.7×10^9 T [57,58]). We neglect the continuum contribution and include only the $2p$ and $3p$ levels in the sum for the calculation of M. A sum over ℓ'' with $\ell'' = 1,3,5,\ldots$ is actually required in Eq. (2.2-7) since the intermediate states are no longer restricted to p-states and virtual transitions are no longer restricted by electric dipole selection rules. Transitions with $\Delta\ell$=3,5, ... become allowed for atoms in strong magnetic fields since ℓ is no longer a good quantum number

Reproduced with permission of the copyright owner. Further reproduction prohibited without permission.

and the states contain admixtures of different ℓ-character. Though the results of Sec. 2.1 could allow the inclusion of higher $\Delta\ell$ transitions, their contribution is probably negligible and are not included here.

The exact calculation of the $2s \rightarrow 1s$ spontaneous emission in the field-free case results in a value of 8.2284 s^{-1} [89]. If only the $2p$ term is included in the sum M a result of 11.71342 s^{-1} is obtained while inclusion of both $2p$ and $3p$ terms gives 10.09387 s^{-1} (about 20% too large). If higher np terms and the continuum are included, the result will reduce to the exact value as $n \rightarrow \infty$. This reduction in the probability with n, for $n \geq 3$, occurs because the contribution given by the $2p$ term is opposite in sign from the remaining np terms and the continuum [88]. If at worst, the same error occurs for the transition rate under the application of an arbitrary magnetic field, then using only the $2p$ and $3p$ data we can obtain an upper limit to the effect of a magnetic field on the $2s \rightarrow 1s$ emission rate. Actually, our calculation improves with field strength as shall be discussed below. The reliance of our semi-empirical method on the available magnetic-field-dependent atomic data can be avoided by using the variational procedure of Victor and Dalgarno [91]. Though the variational method has been successfully applied to two-photon processes in the field-free helium isoelectronic sequence [91–93], it is not pursued here.

To solve Eq. (2.2-15), we have generated code in REDUCE 3.3, an algebraic manipulation software package [94]. The uncertainty in the results are independent of the machine calculation and depend only on the uncertainty of the previously published energy levels (10^{-4}%) and transition strength data (0.1%), the appropriate physical constants ($< 10^{-6}$%), and the limit of the sum in the effective matrix element M.

A problem arises because M contains singularities. The current integration algorithm in REDUCE is not able to handle singularities. Note this is not a numerical integration technique; REDUCE actually returns an analytic function, but evaluating

Reproduced with permission of the copyright owner. Further reproduction prohibited without permission.

it over an interval containing one or more singularities cannot be guaranteed to give a correct result.

A singularity occurs when a photon is in resonance with an intermediate state. At or near resonance, the natural linewidths of the intermediate states must be included in Eq. (2.2-1) [95]. This is done by replacing the denominator in Eq. (2.2-1) by

$$\sqrt{(\nu_{n'\ell'm',n''\ell''m''} + \nu_i)^2 + \left(\frac{\Gamma_{n''\ell''m''}}{2}\right)^2}, \tag{2.2-16}$$

where $\Gamma_{n''\ell''m''}$ is the FWHM natural linewidth of the intermediate level and $i = 1, 2$. The natural linewidths are calculated from the magnetic-field-dependent energy levels and matrix elements and are given in Table 2.2-1. The inclusion of Eq. (2.2-16) removes the singularities, but large resonances still occur when $\nu_i = -\nu_{n'\ell'm',n''\ell''m''}$. Currently, an integration library for REDUCE can integrate functions involving square roots, but unfortunately it cannot handle products of square roots as introduced by inclusion of Eq. (2.2-16) in Eq. (2.2-15). As a consequence, the integration in Eq. (2.2-15) was performed in a piece-wise fashion. Regions near the resonances were evaluated with the IMSL numerical algorithm QDAGP with Eq. (2.2-16) included in Eq. (2.2-15), while REDUCE code was used for regions away from the resonances without including Eq. (2.2-16). The matching occurred at photon frequencies $\pm\epsilon\Gamma_{n''\ell''m''}$ from each resonance. The parameter ϵ was varied over the range from 10 to 10^5 with a resulting variation in the total transition probability of no more than 0.06%, but more typically about 0.01% except for the low field case where the uncertainties in the Zeeman splitting calculations of previous authors are on the order of the splitting. Numerical integration contributed an uncertainty only of 10^{-6}%. So within the limit of the sum in M, the uncertainty in the two-photon transition probability is dominated by the dipole moment uncertainty. The results are reported to this corresponding accuracy.

Reproduced with permission of the copyright owner. Further reproduction prohibited without permission.

TABLE 2.2-1. Energies ν_1, FWHM linewidths Γ, and magnitudes $A_{1s2s}(\nu_1)$ of the first two resonances for the $2s \rightarrow 1s$ hydrogen two-photon transition.

B (au)	$2p_0$ resonance			$2p_{-1}$ resonance		
	ν_1(au)	$\Gamma^a(10^{-8}$ au)	$A_{1s2s}(\nu_1)(\text{au}^{-1}\text{s}^{-1})$	ν_1(au)	Γ^a $(10^{-8}$ au)	$A_{1s2s}(\nu_1)(\text{au}^{-1}\text{s}^{-1})$
0.0002	–	–	–	0.0002001	1.515	1.938+6
0.002	0.0000096	1.504	1.33+3[b]	0.002004	1.504	1.959+9
0.014	0.0003871	1.524	1.146+8	0.00710	1.448	7.110+11
0.02	0.000785	1.532	9.222+8	0.01020	1.430	2.096+12
0.04	0.002955	1.576	4.824+10	0.02071	1.393	1.652+13
0.06	0.00614	1.640	4.220+11	0.03140	1.385	5.148+13
0.1	0.01432	1.802	5.902+12	0.0528	1.401	1.839+14
0.14	0.02334	1.982	2.094+13	0.0734	1.423	3.630+14
0.2	0.03620	2.269	7.204+13	0.1016	1.448	6.026+14
0.4	0.0651	3.199	2.916+14	0.1722	1.457	7.498+14
0.6	0.0809	4.077	3.940+14	0.2219	1.427	5.940+14
1	0.0996	5.710	4.472+14	0.2962	1.367	5.028+14
1.4	0.1115	7.205	4.478+14	0.3543	1.321	4.558+14
2	0.1238	9.301	4.266+14	0.4226	1.272	4.166+14
4	0.1469	15.50	3.550+14	0.4930	1.181	3.594+14
6	0.1595	20.75	3.082+14	0.545	1.133	3.318+14
10	0.1738	29.69	2.512+14	0.621	1.073	3.014+14
14	0.1820	37.33	2.164+14	0.681	1.032	2.828+14
20	0.1896	47.16	1.833+14	0.750	0.988	2.640+14
40	0.2006	72.15	1.304+14	0.905	0.897	2.300+14
60	0.2047	90.70	1.060+14	1.008	0.841	2.114+14
100	0.2075	118.6	8.134+13	1.155	0.766	1.899+14
200	0.2077	164.4	5.672+13	1.380	0.662	1.634+14
400	0.2044	218.8	3.962+13	1.636	0.555	1.408+14
1000	0.1967	302.9	2.496+13	2.024	0.423	1.156+14
2000	0.1894	374.2	1.786+13	2.353	0.334	9.980+13

[a]Determined from Refs. [20,21]

[b]The notation 1.33+3 corresponds to 1.33×10^3.

Reproduced with permission of the copyright owner. Further reproduction prohibited without permission.

2.2.3. Results and Discussion

2.2.3.1. Transition probabilities for hydrogen. Fig. 2.2-1 displays a plot of the $2s \rightarrow 1s$ two-photon spontaneous emission transition probability A_{1s2s} of atomic hydrogen as a function of the magnetic field as calculated from Eq. (2.2-15). Numerical results are presented in Table 2.2-2. At $B = 1$, the cyclotron radius is equal to the Bohr radius.

For $B = 2 \times 10^{-4}$ there is little change in the transition probability A_{1s2s} from the field-free case. Between $B = 2 \times 10^{-3}$ and 2×10^{-1}, A_{1s2s} quickly climbs six orders of magnitude to 1.626×10^{7} s^{-1}. A_{1s2s} reaches a maximum of 1.537×10^{8} s^{-1} at $B = 60$ (1.41×10^{6} T) and decays slightly to 1.055×10^{8} s^{-1} out to $B = 2000$ (4.7×10^{8} T). Compare this behavior to that of the $2p_{-1} \rightarrow 1s$ one-photon transition probability, which has a field-free value of 6.26×10^{8} s^{-1} and decreases slightly to a value of 1.38×10^{8} s^{-1} at $B = 2000$. In the high field region, A_{1s2s} is comparable in magnitude to the $2p_{-1} \rightarrow 1s$ one-photon transition probability. This is greater than seven orders of magnitude change from the field-free case. This dramatic increase in transition probability can be attributed to the ℓ-character mixing of the states which results in "stealing" of transition strength. This increase might suggest for a physical system with a magnetic field in the region of 10^{4} to 10^{9} T, that two-photon transitions may contribute significantly to an observed spectrum. A similar effect has been shown to occur by Alexander and Mészáros [66] for electron cyclotron emissions in a field of 10^{9} T.

2.2.3.2. Hydrogen two-photon spectra. Fig. 2.2-2 displays plots of the spectral distribution $A_{1s2s}(\nu_1)$ as a function of the frequency of the first photon ν_1 (in atomic units) for various field strengths. The dash line includes only the $2p$ terms in the sum of M while the solid line includes both the $2p$ and $3p$ terms. The first plot ($B = 2 \times 10^{-4}$) is similar to that given by Tung et al. [89] for the field-free case except for the resonances near 0 and 0.375. The spectral distribution is zero at 0 and 0.375.

Reproduced with permission of the copyright owner. Further reproduction prohibited without permission.

Reproduced with permission of the copyright owner. Further reproduction prohibited without permission.

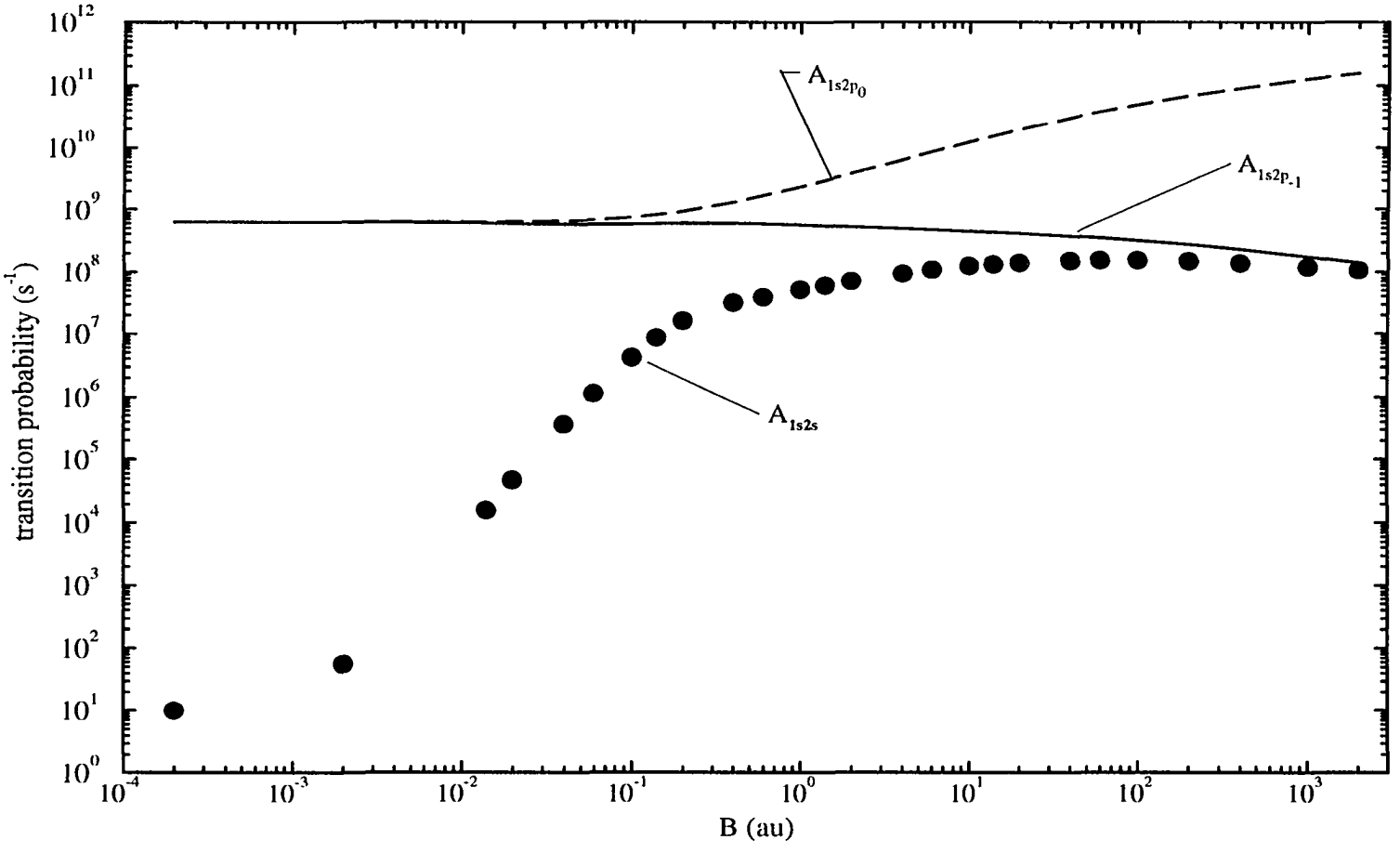

FIG. 2.2-1. Hydrogen 2s-1s spontaneous two-photon emission probability A_{1s2s} (filled circles) with magnetic field strength. A_{1s2s} is compared to the one-photon transition probabilities A_{1s2p_0} (dashed line) and $A_{1s2p_{-1}}$ (solid line) from Ref. [21].

TABLE 2.2-2. Two-photon $2s \rightarrow 1s$ spontaneous emission transition probabilities A_{1s2s} for hydrogenlike atoms at various magnetic field strengths and nuclear charge Z. The results were obtained by including $2p$ and $3p$ contributions to the sum in Eq. (2.2-7). The data in brackets include only $2p$ contributions. Where bracketed results are not given, A_{1s2s} was not changed by inclusion of $3p$ terms to within the precision indicated.

B (au)	Z	$A_{1s2s}(s^{-1})$	B (au)	Z	$A_{1s2s}(s^{-1})$
0.0002	1	10 [11.74]	40	1	1.509+8
0.002	1	56 [58.08]	60	1	1.537+8
0.014	1	1.615+4[a]	100	1	1.537+8
0.02	1	4.712+4	200	1	1.481+8
0.04	1	3.625+5	400	1	1.373+8
0.06	1	1.130+6	1000	1	1.195+8
0.1	1	4.188+6	2000	1	1.055+8
0.14	1	8.765+6			
0.2	1	1.626+7	0.0008	2	6+2 [7.490+2]
0.4	1	3.179+7	0.008	2	1.3+3 [1.491+3]
0.6	1	3.853+7	0.056	2	2.589+5 [2.591+5]
1	1	5.084+7	0.08	2	7.544+5 [7.547+5]
1.4	1	6.007+7	0.8	2	2.602+8
2	1	7.063+7			
4	1	9.307+7	0.0018	3	7+3 [8.527+3]
6	1	1.063+8	0.018	3	1.0+4 [1.229+4]
10	1	1.222+8	0.126	3	1.315+6 [1.317+6]
14	1	1.314+8	0.18	3	3.822+6 [3.826+6]
20	1	1.398+8	1.8	3	1.317+9

[a]The notation 1.615+4 corresponds to 1.615×10^4.

Reproduced with permission of the copyright owner. Further reproduction prohibited without permission.

Reproduced with permission of the copyright owner. Further reproduction prohibited without permission.

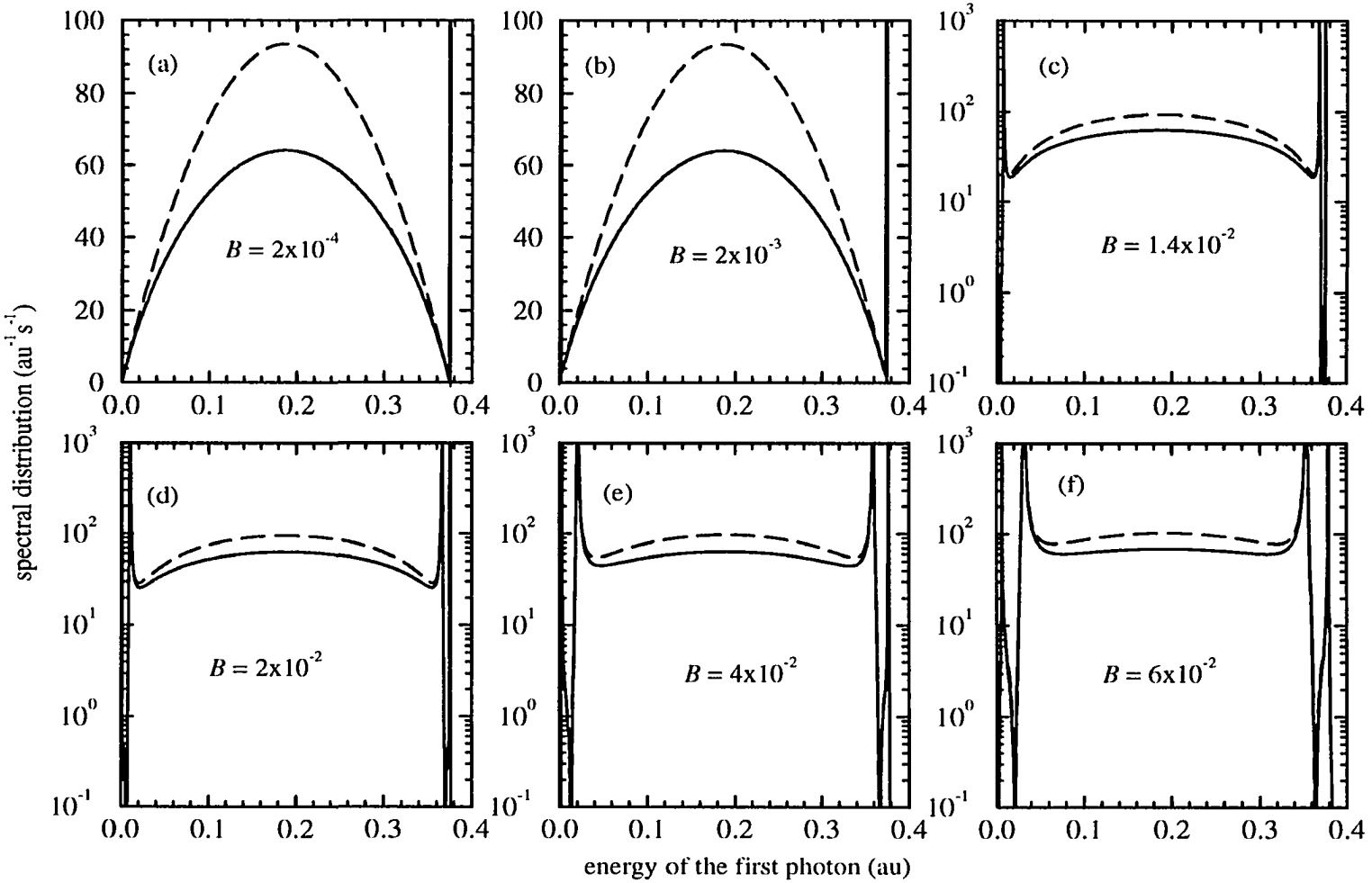

FIG. 2.2-2. Spectral distribution function for various magnetic field strengths. The dashed line includes only *2p* contributions while the solid line contains both *2p* and *3p* contributions.

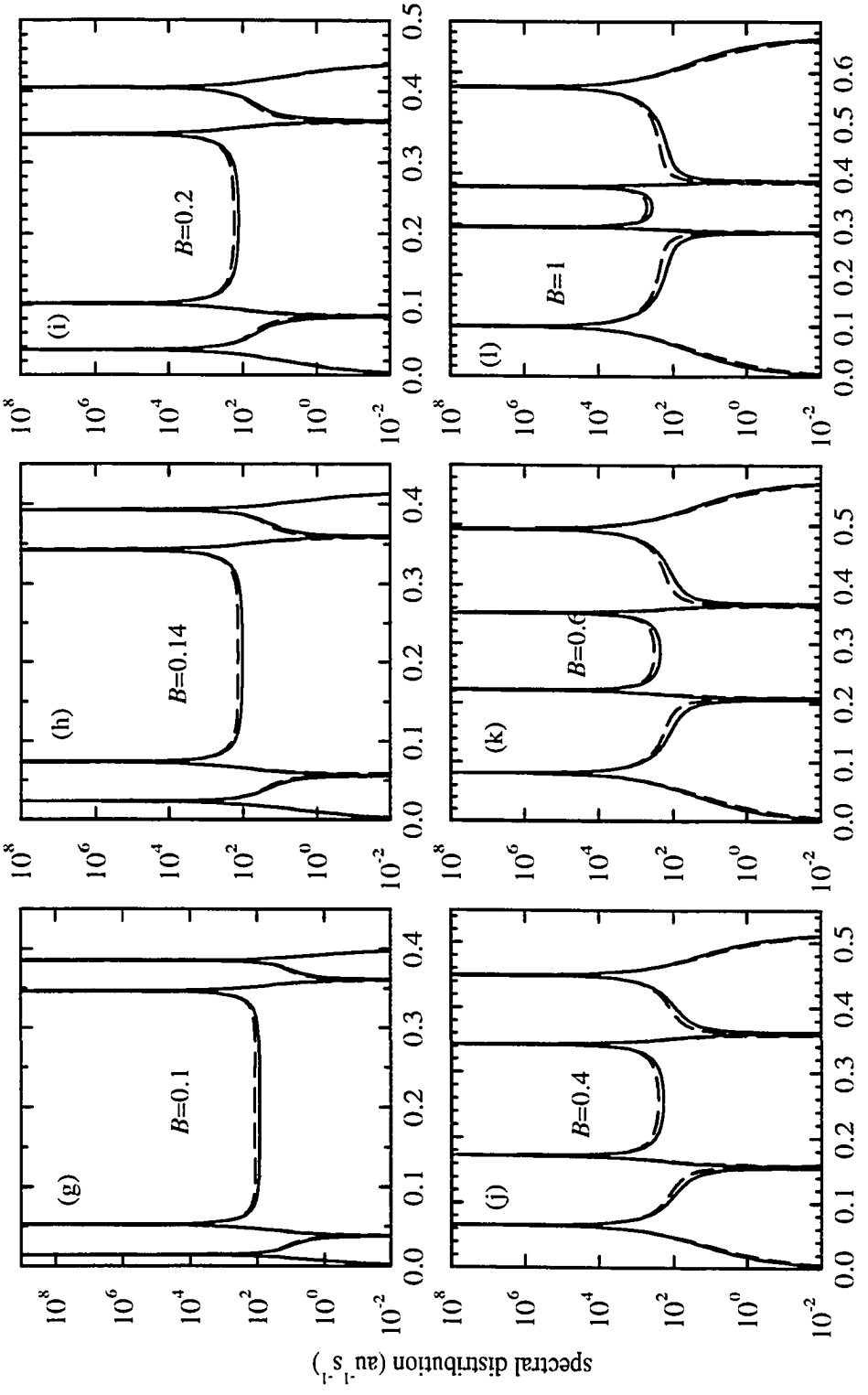

FIG. 2.2-2. Continued.

Reproduced with permission of the copyright owner. Further reproduction prohibited without permission.

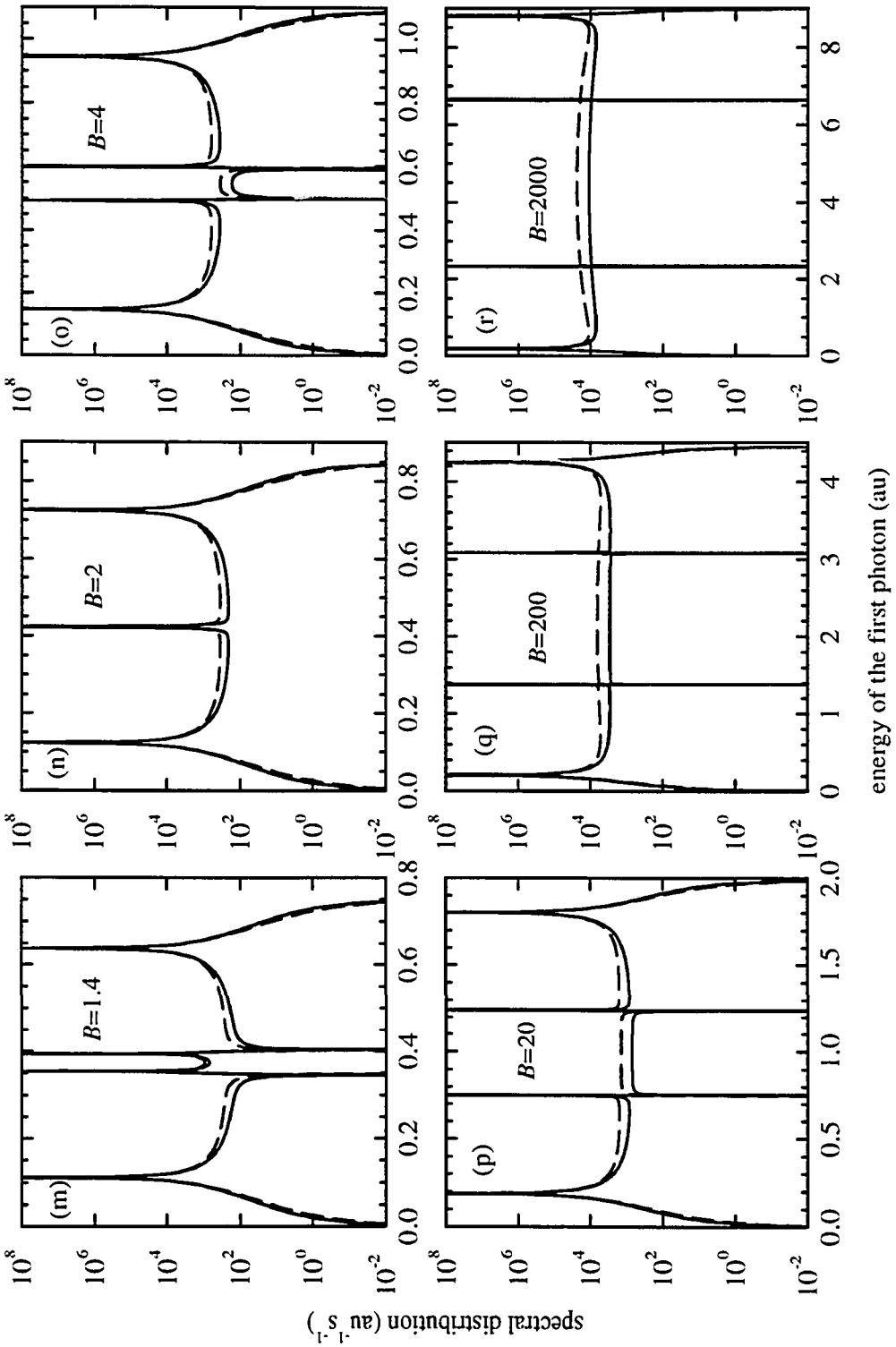

FIG. 2.2-2. Continued.

Reproduced with permission of the copyright owner. Further reproduction prohibited without permission.

This is as expected since both cases correspond to $2s$-$1s$ single-photon transitions (where the photon frequencies are forbidden by dipole selection rules). The spectral distribution is maximum (neglecting the resonances) when the two photons have equal frequencies. A finer energy resolution of this plot reveals features at low and high energy (see Fig. 2.2-3).

As the magnetic field is increased these features are resolved more readily. The resonances occur as a consequence of the Zeeman interaction removing the m-state degeneracy of the $2p$ level. The magnetic field pushes both the $2p_0$ and the $2p_{-1}$ states below the $2s$ level. Between the $2s$ and $1s$ levels there is an infinite distribution of intermediate virtual states. With the applied magnetic field, two of these virtual states correspond to the two real discrete $2p_0$ and $2p_{-1}$ states resulting in resonant enhancements of the two-photon transition probability. For example, consider the case where $B = 1.4$. The resonances at 0.1115 and 0.638 are due to an interaction with the $2p_0$ state while those at 0.3543 and 0.3952 are due to the $2p_{-1}$ state. The $2p_1$ state does not contribute a resonance because the magnetic field pushes it into the continuum. The minima at 0.3471 and 0.4025 result from an interference effect between the two resonant pathways: $2s \rightarrow 2p_0 \rightarrow 1s$ and $2s \rightarrow 2p_{-1} \rightarrow 1s$. Table 2.2-1 gives the energies, linewidths, and magnitudes of the first two resonances for each of the field strengths in Fig. 2.2-2 while Table 2.2-3 gives the energies and linewidths of the minima. The minima linewidths are FWHM with respect to the magnitude at $\frac{1}{2}\nu_o$.

The frequencies of the resonances do not depend on the number of terms used for the sum in M, but the frequency and linewidth of the minima do. When $3p$ terms are included, the frequencies of the minima shift generally by $< 0.6\%$ of ν_o from the $2p$ only values. For $B < 1$, the shift is to lower energies for the first minimum and to higher energies for the second. The reverse is true for $B > 1$. The linewidths decrease for $B < 1$ by usually $< 4\%$, but for $B > 1$, they may increase by as much as 30%.

Reproduced with permission of the copyright owner. Further reproduction prohibited without permission.

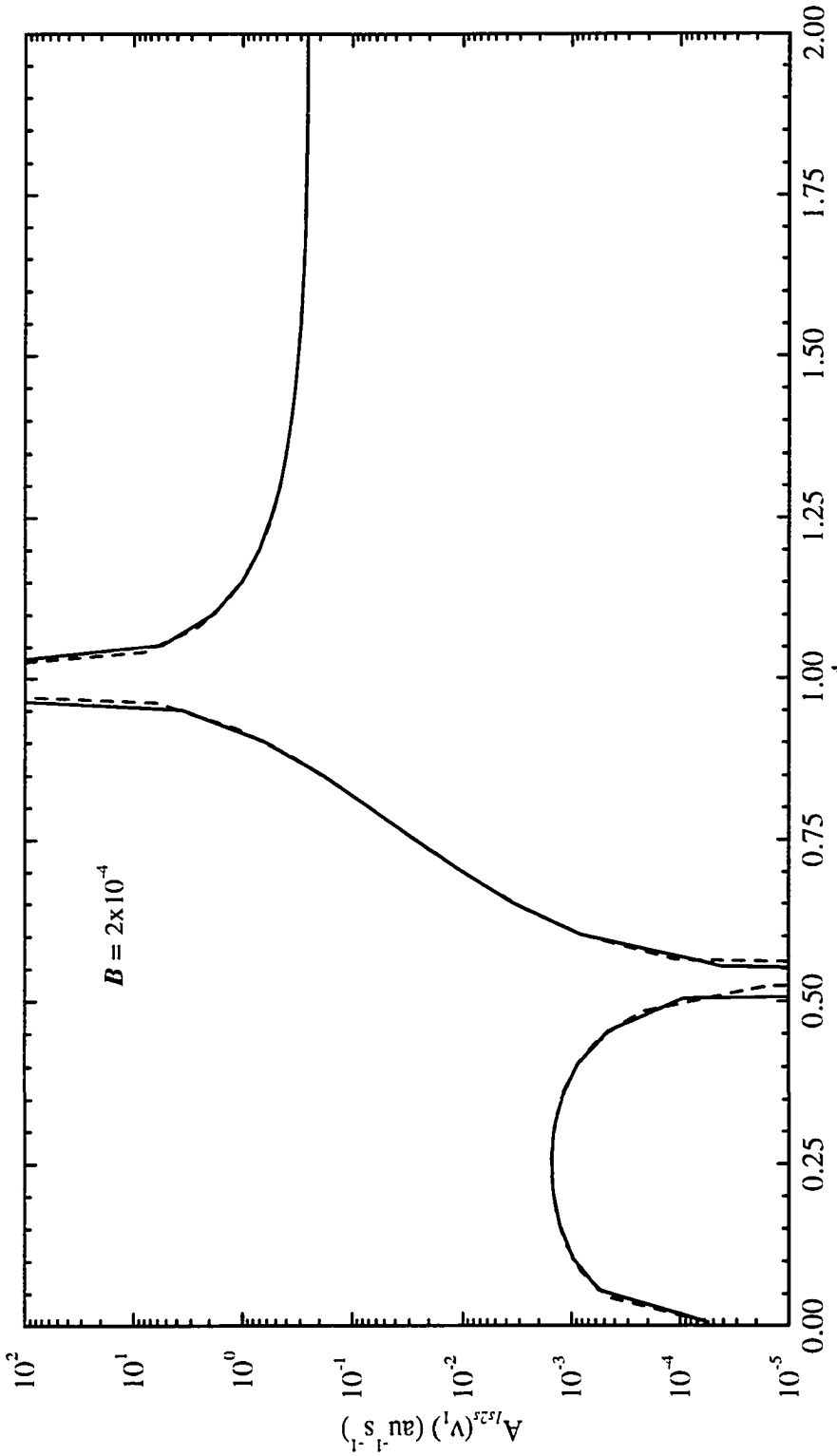

FIG. 2.2-3. Same as FIG. 2.2-2 but at reduced frequency scale to show low frequency minimum and resonance at $B = 2x10^{-4}$.

Reproduced with permission of the copyright owner. Further reproduction prohibited without permission.

TABLE 2.2-3. Energies ν_1 of the minima, their linewidths Γ at half the magnitude of $A_{1s2s}(\frac{1}{2}\nu_o)$, and the total $2s \rightarrow 1s$ energy difference ν_o for hydrogen. The minima and linewidths were determined with $2p$ and $3p$ contributions included in M.

B (au)	First minimum ν_1(au)	Second minimum ν_1(au)	Γ(au)	ν_o (au) [a]
0.0002	0.0000537	0.3450	0.000008[b]	0.3750001
0.002	0.000571	0.3745	0.000781	0.375008
0.014	0.004228	0.3717	0.00592	0.3756311
0.02	0.00616	0.3708	0.00810	0.3762758
0.04	0.01313	0.3668	0.01448	0.3798607
0.06	0.02088	0.3644	0.01955	0.3852401
0.1	0.03804	0.3614	0.02691	0.3994374
0.14	0.05605	0.3599	0.03182	0.4159167
0.2	0.08245	0.3589	0.03684	0.4413948
0.4	0.1542	0.3613	0.04920	0.5154392
0.6	0.2069	0.3679	0.05965	0.5746970
1	0.2846	0.3862	0.09785	0.6707001
1.4	0.3452	0.4044	0.1663	0.7494414
2	–	–	–	0.84827
4	0.4999	0.5920	0.01198	1.0919834
6	0.5505	0.7200	0.01177	1.270596
10	0.6265	0.9125	0.009915	1.538912
14	0.6845	1.061	0.008570	1.7450275
20	0.7525	1.239	0.007290	1.991594
40	0.9065	1.657	0.003952	2.562853
60	1.010	1.950	0.003225	2.958864
100	1.156	2.378	0.003299	3.532881
200	1.381	3.078	0.002262	4.457590
400	1.637	3.934	0.001590	5.570125
1000	2.024	5.340	0.000955	7.366195
2000	2.353	6.645	0.000605	8.99824

[a]From Ref. [20]

[b]There is only one resonance at this field strength. The linewidth is determined with respect to the local maximum of energies less than the minimum. See Fig. 2.2-3.

Reproduced with permission of the copyright owner. Further reproduction prohibited without permission.

Results given in Table 2.2-3 include contributions from $2p$ and $3p$ terms.

Both resonances and minima have been observed in other hydrogen two-photon calculations, but without a magnetic field and only for higher state transitions. For example, Tung et al. [89] found resonances for the $3s \rightarrow 1s$ spontaneous emission due to resonant transitions to the $2p$ level. In the $4s \rightarrow 1s$ spontaneous emission, resonances and interference minima occur through an interaction between the $3p$ and $2p$ levels. Experimentally, both of these effects have been observed in field-free two-photon absorption in sodium vapor between the $3s$ and $4d$ levels where the $3p\ ^2P_{\frac{1}{2}}$ and $3p\ ^2P_{\frac{3}{2}}$ levels are the resonant states [62].

Another interesting feature can be seen in Fig. 2.2-2 by comparing the sequence of plots from $B = 1.4$ to 4. In the first instance, and for all preceding plots, the first minimum is between the first and second resonances. At $B = 2$, the minima have disappeared and the second and third resonances appear to overlap. In the latter instance, and for all plots thereafter, the first minimum appears to be between the second and third resonances. This shifting of the minimum is due to the migration of the $2p_{-1}$ level from near the $2s$ level to halfway between the $2s$ and $1s$ levels (at $B \sim 1$) to near the $1s$ level. Actually, the minimum is not shifting its relative position with respect to the resonances, but it is the second and third resonances that are switching places because the second resonance is migrating towards higher frequency while the third is migrating towards lower frequency. The resonances pass each other at $B \sim 1$ and interesting enough this is the field strength that gives a cyclotron radius approximately equal to the Bohr radius.

Comparing the plots in Fig. 2.2-2 reveals the cause of the increase in transition probability with field strength. The energy difference between the $2s$ and $1s$ levels increases from 0.375 to 8.998 due to the rapid increase of the $1s$ level binding energy with field strength. Neglecting resonances, the maximum of the spectral distribution increases from 64 to 11280 $\text{au}^{-1}\text{s}^{-1}$. But, most importantly, the resonances themselves

Reproduced with permission of the copyright owner. Further reproduction prohibited without permission.

contribute significantly and are dominant for $B \geq 0.014$. The above effects collectively increase the spectral distribution curve whose area is the total transition probability.

Inclusion of the higher $n''p$ terms ($n'' \geq 4$) and the continuum in the sum in M will not affect the general shape of the spectral distributions, but will only slightly reduce the magnitude. Of the $n''p$ states, only $2p_0$ and $2p_{-1}$ can reside between the $2s$ and $1s$ states for all values of B. None of the higher $n''p$ levels cross the $2s$ level and therefore will not produce any additional resonance or interference features. Since the resonances give the dominant contributions to the transition probability for large fields, the exclusion of the higher $n''p$ terms and the continuum will have a negligible effect for $B \geq 0.014$ as can be seen by comparing the transition probabilities calculated with and without the $3p$ terms given in Table 2.2-2. Other $n''\ell''$-states with ℓ'' =3,5, ...and $m'' \sim -\ell''$ will cross the $2s$ level, but with negligible dipole strengths.

2.2.3.3. Cascade emission of the 2s level. When an intermediate state $|n''\ell''m''\rangle$ corresponds to a real state and has energy between the $|n'\ell'm'\rangle$ and $|n\ell m\rangle$ states, cascade emission from the $|n'\ell'm'\rangle$ state (the $2s$ level in our situation) must also be considered as a possible decay route. In the field-free case, cascade emission is not important since $A_{2p2s} = 0$. Even, if the Lamb shift is considered, Shapiro and Breit [85] have estimated that $A_{2p2s} = 2 \times 10^{-10}$ s^{-1}, ten orders of magnitude smaller than the two-photon decay rate and therefore negligible. Conversely, cascade emission becomes important when a strong magnetic field is applied.

In the nonrelativistic dipole approximation, decay of the $2s$ level can only result from the $2s \rightarrow 1s$ two-photon emission and the cascade emissions $2s \rightarrow 2p_0 \rightarrow 1s$ and $2s \rightarrow 2p_{-1} \rightarrow 1s$. The total decay rate is therefore the sum of the rates of the three possible decay routes. Fig. 2.2-4 plots the branching ratios r_i for each of the decay routes as a function of magnetic field. At the low-field limit, the two-photon ratio r_1 is unity while the cascade ratios, r_2 and r_3, approach zero as expected. For $B \geq 2 \times 10^{-2}$, r_1 is constant at 0.193 and remains an important contribution to the

Reproduced with permission of the copyright owner. Further reproduction prohibited without permission.

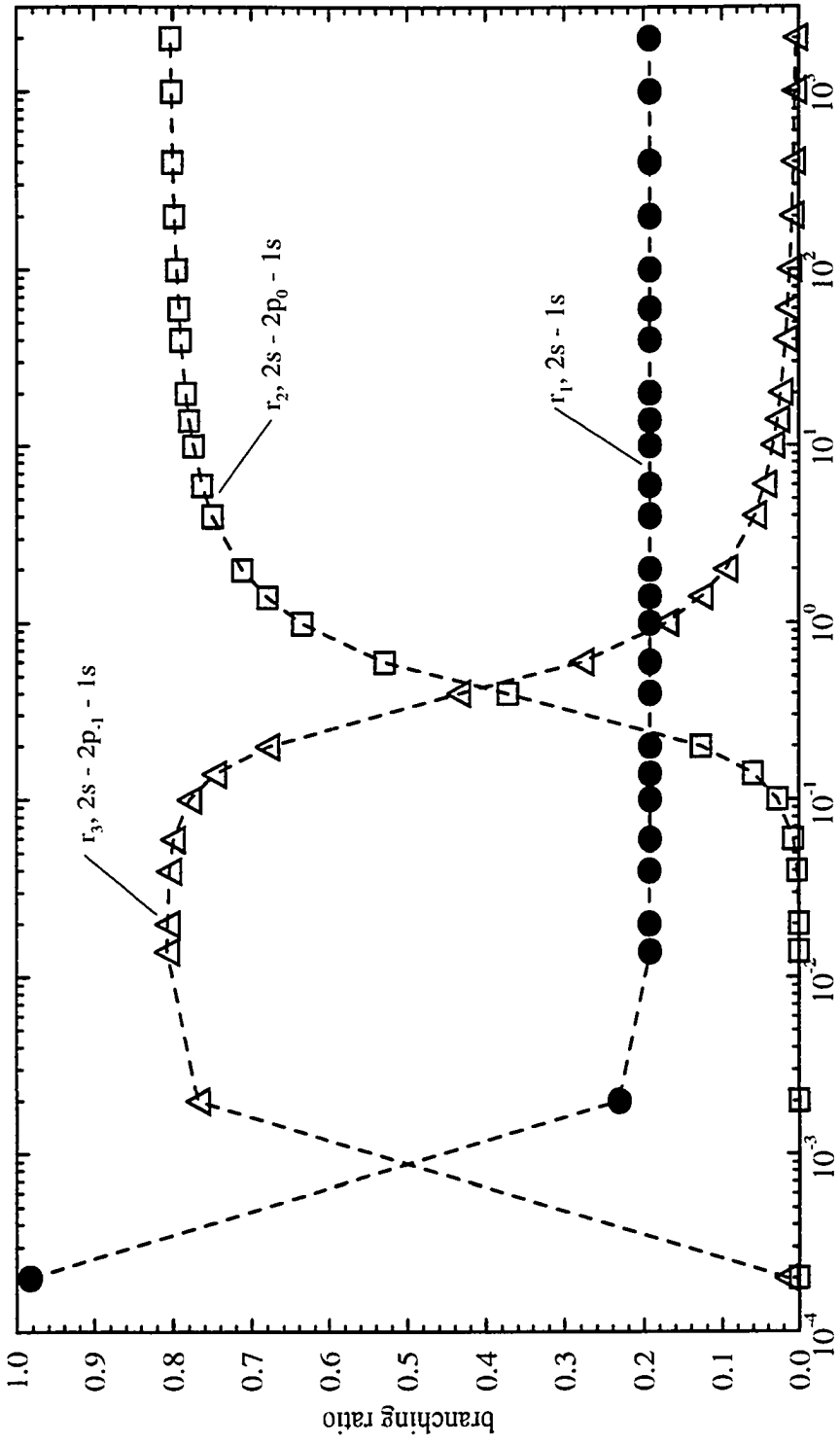

FIG. 2.2-4. Branching ratios for the decay of the hydrogen 2s level with magnetic field strength.

Reproduced with permission of the copyright owner. Further reproduction prohibited without permission.

total decay rate. The ratio r_2 remains small for $B \leq 0.2$, but becomes the major rate for $B \geq 0.4$. The ratio r_3 is the major decay route between $B = 2 \times 10^{-3}$ and 2×10^{-1}, but is small between $B = 2$ and 2000.

2.2.3.4. Higher multipole and other corrections. The inclusion of relativistic effects to the field-free $2s \rightarrow 1s$ two-photon emission is on the order of 7×10^{-4} s^{-1} [96], but may become important for $B > 100$ [37]. Contributions from higher multipole terms are less than 3×10^{-10} s^{-1} at zero field [96]. Recent work by Cuvelliez et al. [39] has shown that magnetic dipole (M1) and electric quadrupole (E2) transitions are weak for field strengths between $B = 2$ and $B = 2000$ except for E2 $\Delta m = 0$ transitions. The E2 $2s \rightarrow 1s$ transition approaches a probability of 10^7 s^{-1} at $B = 2000$, which is about 10% of the two-photon A_{1s2s} rate and therefore contributes 2% to the total $2s$ decay. In addition, a two-E2-photon transition may contribute to the total two-photon rate and need to be included in Eq. (2.2-7), but the contribution is probably no greater than 0.01%. Decay by a one-photon M1 transition at zero field is only 2.4957×10^{-6} s^{-1} [97], but may become important in the intermediate-field regime for $B \lesssim 1$.

2.2.3.5. Hydrogenlike ions. Results for hydrogenlike ions with nuclear charge Z can be obtained from the hydrogen values using the relations for the energy, dipole moment matrix element, and one-photon transition probability given by Eqs. (2.1-14), (2.1-43), and (2.1-44), respectively, and the linewidth

$$\Gamma(Z, B) = Z^4 \Gamma(Z = 1, B/Z^2). \tag{2.2-17}$$

For $B = 0$ [85],

$$A_{1s2s}(Z) = Z^6 A_{1s2s}(Z = 1), \tag{2.2-18}$$

which can easily be obtained from the relations for the effective matrix element and the spectral distribution

Reproduced with permission of the copyright owner. Further reproduction prohibited without permission.

$$M_{1s2s}(\nu_1, Z) = Z^{-8} M_{1s2s}(\nu_1, Z = 1) \tag{2.2-19}$$

and

$$A_{1s2s}(\nu_1, Z) = Z^4 A_{1s2s}(\nu_1, Z = 1). \tag{2.2-20}$$

For $n's \rightarrow 1s$ transitions with $n' \geq 3$, Eqs. (2.2-18) to (2.2-20) are not valid since there are resonances between n' and $n = 1$ created by real $n''p$ states. The resonances require that the denominator in Eq. (2.2-1) be replaced by Eq. (2.2-16). Now E (or ν) scales as Z^2 while Γ scales as Z^4 and thus near the resonances the Γ-term dominates the ν-term in Eq. (2.2-16). Thus Eqs. (2.2-19) and (2.2-20) are replaced near the resonances by

$$M_{1sn's}(\nu_1, Z) = Z^{-12} M_{1sn's}(\nu_1, Z = 1), \; n' \geq 3, \tag{2.2-21}$$

and

$$A_{1sn's}(\nu_1, Z) = A_{1sn's}(\nu_1, Z = 1), \; n' \geq 3. \tag{2.2-22}$$

Eq. (2.2-22) reveals the unexpected result that at a resonance the spectral distribution is independent of Z. Therefore, the spectral distribution magnitudes given in Table 2.2-1 are appropriate for all Z, but with their energies shifted by Z^2 from the value for hydrogen. Since the resonances dominate the spectral distribution, the two-photon transition is then given approximately by

$$A_{1sn's}(Z) = Z^2 A_{1sn's}(Z = 1), \; n' \geq 3, \tag{2.2-23}$$

which scales as Z^2 instead of Z^6 as in Eq. (2.2-18).

When a large magnetic field is applied, resonances appear as discussed above for the $2s \rightarrow 1s$ case similar to the $n's \rightarrow 1s$ field-free case with $n' \geq 3$. So, for $B \geq 0.014$ and near the resonances we have

$$M_{1s2s}(\nu_1, Z, B) = Z^{-12} M_{1s2s}(\nu_1, Z = 1, B/Z^2), \tag{2.2-24}$$

Reproduced with permission of the copyright owner. Further reproduction prohibited without permission.

and

$$A_{1s2s}(\nu_1, Z, B) = A_{1s2s}(\nu_1, Z = 1, B/Z^2), \tag{2.2-25}$$

and since the resonances dominate the spectral distribution

$$A_{1s2s}(Z, B) \approx Z^4 A_{1s2s}(Z = 1, B/Z^2),\ B \geq 0.014. \tag{2.2-26}$$

Eq. (2.2-26) scales as Z^4 instead of Z^2 because the integration over energy in Eq. (2.2-15) is dominated by the linewidth which scales as Z^4. So, the total two-photon transition probability can be obtained for all hydrogenlike ions when $B \geq 0.014$ using Eq. (2.2-26) and Table 2.2-2. Some values for He^+ and Li^{2+} are given in Table 2.2-2 for $B \leq 0.014$.

Reproduced with permission of the copyright owner. Further reproduction prohibited without permission.

2.3. Two-Photon Polarization of Alkali Atoms

It is well known that the application of a strong, laboratory-strength external magnetic field ($B < 10$ T) to an atom and the subsequent probing of the highly-excited Rydberg states results in rich, seemingly chaotic spectra containing a multitude of resonance and interference features (for a compilation see Gay [98]). These features are attributed to Rydberg progressions converging to many Landau thresholds created by the applied field and are a consequence of the quadratic Zeeman splitting of levels near the continuum.

In the absence of a magnetic field, interference effects in two-photon experiments were first observed by Bjorkholm and Liao [62]. They measured the fluorescence from the Na $4p\ ^2P_j$ level after a $3s\ ^2S_{\frac{1}{2}} \rightarrow 4d\ ^2D_j$ excitation using two counterpropagating lasers tuned to resonance near the intermediate $3p\ ^2P_j$ levels. At a frequency between the intermediate ^2P_j levels ($\sim \frac{1}{2}\zeta$ larger than the Na D2 frequency, where ζ is the ^2P_j spin-orbit constant) a minimum in the fluorescence was observed and was attributed to the destructive interference of the intermediate levels. About two decades ago it was noted that high precision measurements could be made by obtaining polarization spectra. Tam and Au [63] investigated Rayleigh scattering in Na and found a reversal in the polarization to $\sim -100\%$ at the excitation frequency observed by Bjorkholm and Liao [62] for the fluorescence minimum. Later, Zei et al. [64] performed a two-photon experiment similar to Bjorkholm and Liao [62], but measured the polarization and found an analogous reversal to the one observed by Tam and Au [63].

In this section, we regress from the strong field regime to extend the previous two-photon investigation of Sec. 2.2 to study this depolarization phenomena for low-lying levels in H and the alkali-atoms Li and Na in the presence of laboratory-strength magnetic fields. Published results from this work are to appear in Stancil and Copeland

Reproduced with permission of the copyright owner. Further reproduction prohibited without permission.

[99]. For this section units typical for experimentalists are used, i.e. energy or frequency ω in cm^{-1} and magnetic field strength in T.

2.3.1. Theory

The probability for an atom in an initial level $|a\rangle$ to be excited via a two-photon absorption to a final level $|b\rangle$ with an intermediate level $|i\rangle$ is given within the non-relativistic dipole approximation analogous to Eq. (2.2-1) by

$$W_{ba} = K' I_1 I_2 \sum_{m_a} \sum_{m_b} \left| \sum_{m_i} \left\{ \frac{\langle b|\mathbf{r}\cdot\hat{\mathbf{e}}_1|i\rangle\langle i|\mathbf{r}\cdot\hat{\mathbf{e}}_2|a\rangle}{\omega_2 - \omega_{ia}} + \frac{\langle b|\mathbf{r}\cdot\hat{\mathbf{e}}_2|i\rangle\langle i|\mathbf{r}\cdot\hat{\mathbf{e}}_1|a\rangle}{\omega_1 - \omega_{ia}} \right\} \right|^2 \quad (2.3\text{-}1)$$

where I_1 and I_2 are the intensities of the incident laser beams of frequencies ω_1 and ω_2 with polarization vectors $\hat{\mathbf{e}}_1$ and $\hat{\mathbf{e}}_2$, ω_{bi} and ω_{ia} are the gross structure frequency differences, the sums are taken over the various sublevels of $|a\rangle$, $|b\rangle$, and $|i\rangle$, and K' is a proportionality constant. The geometry of the problem is displayed in Fig. 2.3-1 with the excitation scheme given in Fig. 2.3-2. Equation (2.3-1) as discussed in Sec. 2.2.2 is obtained from second-order time-dependent perturbation theory assuming the incident intensities to be weak and the population of $|b\rangle$ to be negligible compared to $|a\rangle$.

For laboratory situations, we are interested in field strengths less than or equal to those corresponding to the Paschen-Back regime discussed in Sec. 2.1.1. More specifically, we will study the transition between the weak-field region or anomalous Zeeman effect and the Paschen-Back regime. In the weak-field regime, the total angular momentum j is a "good" quantum number while ℓ and s are not since the orbital and spin angular momentum are coupled. The transition selection rules are

$$\Delta j = 0, \pm 1 \quad (2.3\text{-}2)$$

and

$$\Delta m_j = 0, \pm 1 \quad (2.3\text{-}3)$$

where $m_j = m + m_s$ is the projection of j onto the z-axis.

Reproduced with permission of the copyright owner. Further reproduction prohibited without permission.

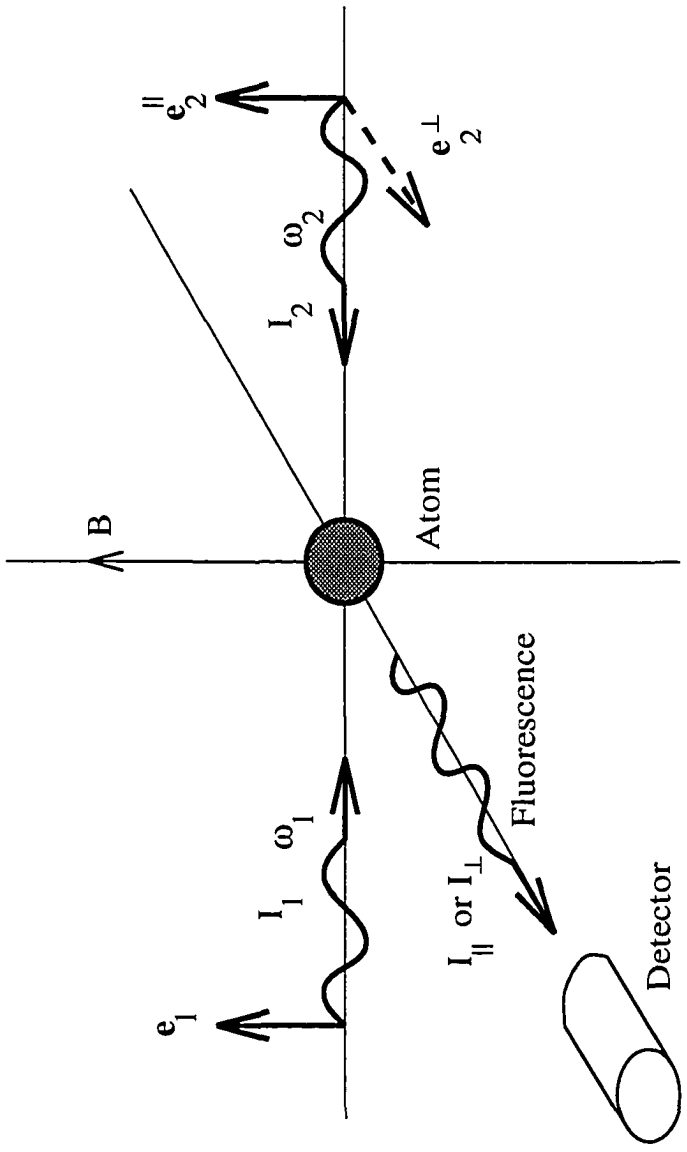

FIG. 2.3-1. Two-photon excitation and fluorescence geometry.

Reproduced with permission of the copyright owner. Further reproduction prohibited without permission.

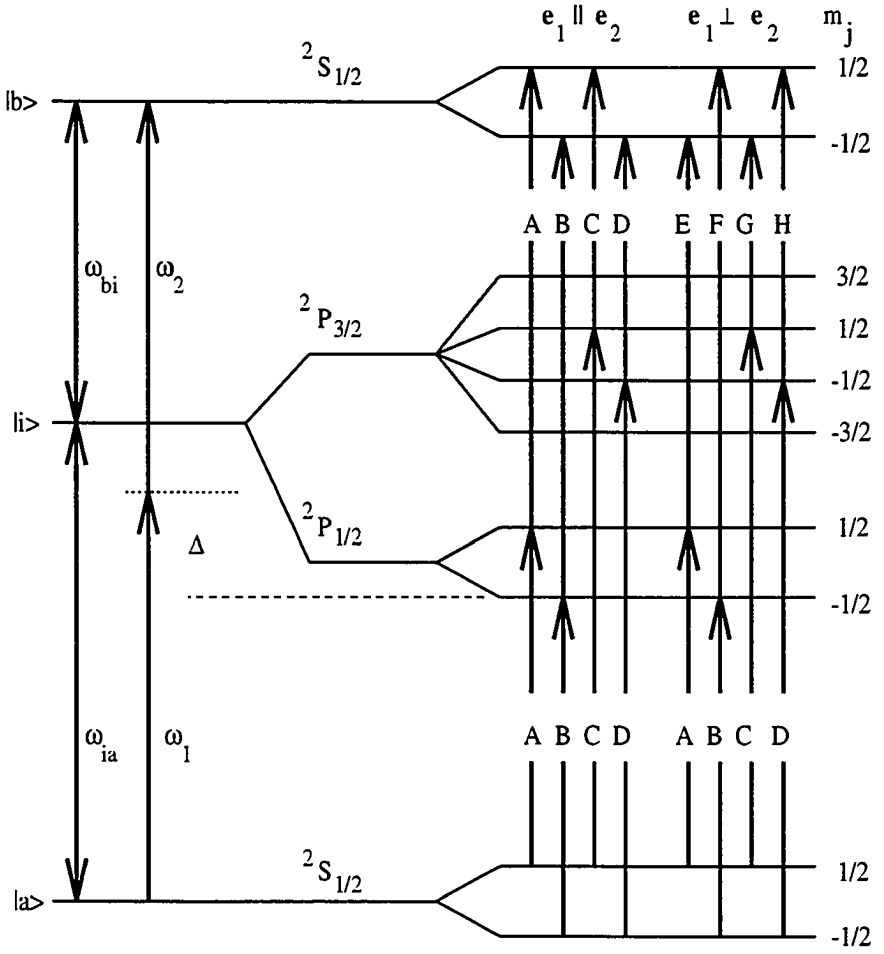

FIG. 2.3-2. Two-photon excitation scheme.

Reproduced with permission of the copyright owner. Further reproduction prohibited without permission.

The problem becomes a ten-level atom (eight levels contributing to the excitation scheme as shown in Fig. 2.3-2) in the coupled representation $|n\ell jm_j\rangle$ basis. In the weak-intermediate field regime the spin-orbit and magnetic perturbations must be treated simultaneously. The energy splittings are as given by Condon and Shortley [100]. After a straight-forward, but tedious, exercise in angular momentum algebra, the transition probability with the polarization vectors of the incident photons parallel is given by

$$\begin{aligned} W_{ba}^{\parallel} = KI_1I_2\Bigg\{\Bigg[&\frac{S_A(B)/S_A(0)}{\Delta\omega+\zeta/2+(R_+ + R_-)/4-\Delta}+\frac{S_A(B)/S_A(0)}{\mu_B B+(R_+ - R_-)/4+\Delta} \\ &+\frac{2S_C(B)/S_C(0)}{\Delta\omega+\zeta/2-(R_+ - R_-)/4-\Delta}+\frac{2S_C(B)/S_C(0)}{\mu_B B-(R_+ + R_-)/4+\Delta}\Bigg]^2 \\ &+\Bigg[\frac{S_B(B)/S_B(0)}{\Delta\omega-\mu_B B+\zeta/2+R_-/2-\Delta}+\frac{S_B(B)/S_B(0)}{\Delta} \\ &+\frac{2S_D(B)/S_D(0)}{\Delta\omega-\mu_B B+\zeta/2-\Delta}+\frac{2S_D(B)/S_D(0)}{-R_-/2+\Delta}\Bigg]^2\Bigg\} \end{aligned} \tag{2.3-4}$$

and the probability with the polarization vectors perpendicular is given by

$$\begin{aligned} W_{ba}^{\perp} = KI_1I_2\Bigg\{\Bigg[&\frac{(S_A(B)S_E(B)/S_A(0)S_E(0))^{1/2}}{\Delta\omega-2\mu_B B+\zeta/2+(R_+ + R_-)/4-\Delta} \\ &-\frac{(S_B(B)S_F(B)/S_B(0)S_F(0))^{1/2}}{\Delta} \\ &-\frac{(S_C(B)S_G(B)/S_C(0)S_G(0))^{1/2}}{\Delta\omega-2\mu_B B+\zeta/2-(R_+ - R_-)/4-\Delta}+\frac{(S_D(B)S_H(B)/S_D(0)S_H(0))^{1/2}}{-R_-/2+\Delta}\Bigg]^2 \\ &+\Bigg[\frac{(S_A(B)S_E(B)/S_A(0)S_E(0))^{1/2}}{\mu_B B+(R_+ - R_-)/4+\Delta}-\frac{(S_B(B)S_F(B)/S_B(0)S_F(0))^{1/2}}{\Delta\omega+\mu_B B+\zeta/2+R_-/2-\Delta} \\ &-\frac{(S_C(B)S_G(B)/S_C(0)S_G(0))^{1/2}}{\mu_B B-(R_+ + R_-)/4+\Delta} \\ &+\frac{(S_D(B)S_H(B)/S_D(0)S_H(0))^{1/2}}{\Delta\omega+\mu_B B+\zeta/2-(R_+ - R_-)/4-\Delta}\Bigg]^2\Bigg\} \end{aligned} \tag{2.3-5}$$

where μ_B is the Bohr magneton, Δ is the detuning of the second photon from resonance with the $^2P_{\frac{1}{2}}(m_j=-\frac{1}{2})$ state while ω_1 is held fixed at the $n_a s\ ^2S_{\frac{1}{2}}(m_j=-\frac{1}{2}) \rightarrow n_i p\ ^2P_{\frac{1}{2}}(m_j=-\frac{1}{2})$ frequency, $\Delta\omega=\omega_{bi}-\omega_{ia}$, $S_x(B)$ are the magnetic-field-dependent line strengths with $x=A,\ldots,H$ being labels for the transitions shown in Fig. 2.3-2, and

Reproduced with permission of the copyright owner. Further reproduction prohibited without permission.

$$R_{\pm} = (4\mu_B^2 B^2 \pm 4\zeta\mu_B B + 9\zeta^2)^{1/2}. \tag{2.3-6}$$

Relations for the line strengths can be found in Darwin [101] and the reduced matrix elements of the dipole operator are absorbed into the K' of Eq. (2.3-1) to give K in Eqs. (2.3-4) and (2.3-5). The probabilities $W_{ba}^{\parallel}$ and $W_{ba}^{\perp}$ are proportional to the fluorescence intensities $I_{\parallel}$ and $I_{\perp}$, respectively, which would be monitored in an experiment as shown in Fig. 2.3-1.

The linear degree of polarization is then given by

$$P_L = \frac{I_{\parallel} - I_{\perp}}{I_{\parallel} + I_{\perp}} = \frac{W_{ba}^{\parallel} - W_{ba}^{\perp}}{W_{ba}^{\parallel} + W_{ba}^{\perp}}. \tag{2.3-7}$$

2.3.2. Results and Discussion

Figures 2.3-3 and 2.3-4 display two-photon polarization spectra of an alkali atom for various scaled magnetic field strengths B/ζ for scaled detunings Δ/ζ near resonance with intermediate ^2P_j levels. The ζ-scaled spectra can be obtained since the only parameters in Eqs. (2.3-4) and (2.3-5) that depend on the atom's structure are ζ and $\Delta\omega$. $\Delta\omega$ has a negligible contribution.

We reproduce the usual polarization reversal for $B/\zeta = 0$ as obtained by Zei et al. [64] and others. This feature occurs at $\Delta/\zeta \sim \frac{1}{2}$. Two additional depolarization features become visible when a magnetic field is applied. The first appears near $\Delta/\zeta \sim 0$ for weak fields and is a result of interference among the anomalous Zeeman split components of the $^2P_{\frac{1}{2}}$ level. The depolarization increases and shifts to more negative detunings with increasing field strength as shown in Fig. 2.3-3. The second depolarization feature appears near $\Delta/\zeta \sim \frac{3}{2}$ and can be attributed to Zeeman split $^2P_{\frac{3}{2}}(m = \pm\frac{1}{2})$ levels. This depolarization feature also increases with field strength, but its detuning decreases to slightly less than $\frac{3}{2}$ for weak to intermediate field strengths before finally increasing for large fields.

Tam and Au [63] found that P_L in their Na ($\zeta \sim 11.5$ cm^{-1}) Rayleigh scattering experiment was unaltered for $B \sim 0.01$ T. It is clear from Fig. 2.3-3 that a resolved

Reproduced with permission of the copyright owner. Further reproduction prohibited without permission.

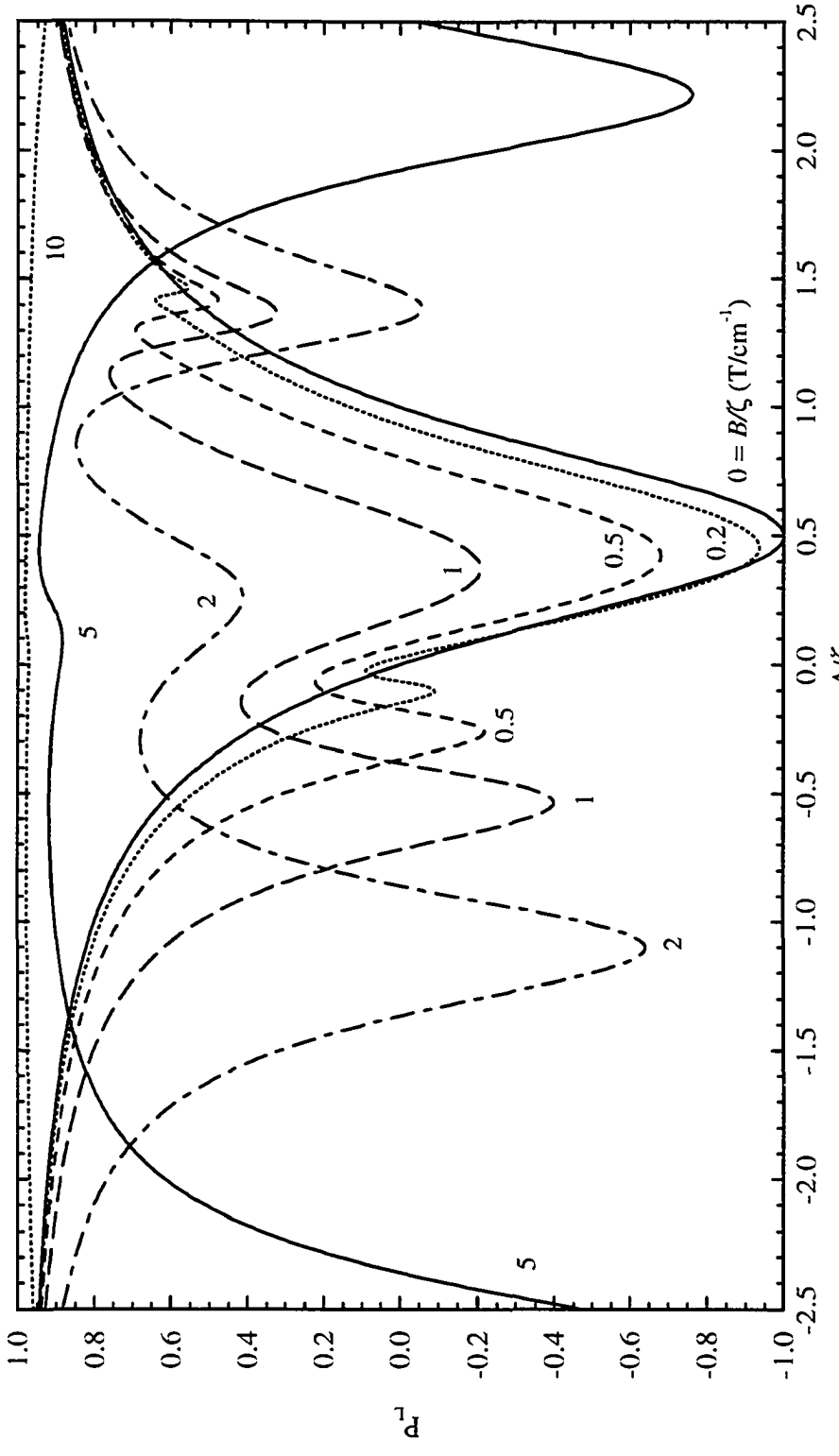

FIG. 2.3-3. Polarization spectra for two-photon $n_a s\ ^2S_{1/2} - n_b s\ ^2S_{1/2}$ absorption in near resonance with $n_k p\ ^2P_j$ levels for various scaled field strengths B(T)/ζ(cm^{-1}).

Reproduced with permission of the copyright owner. Further reproduction prohibited without permission.

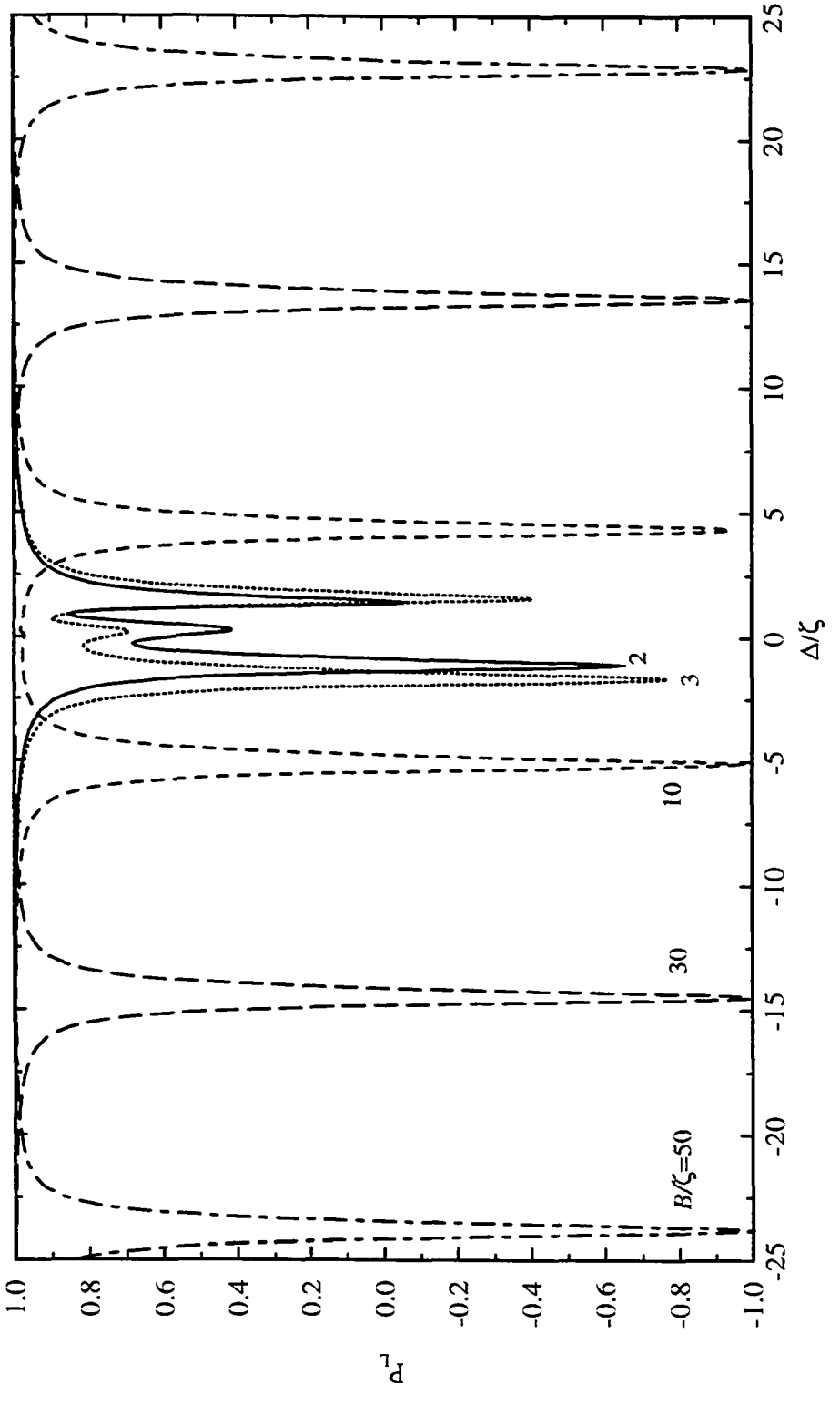

FIG. 2.3-4. Same as FIG. 2.3-3 but for larger detunings.

Reproduced with permission of the copyright owner. Further reproduction prohibited without permission.

depolarization feature will only be observable for $B > 1$ T. Even for Li where $\zeta \sim 0.224$ cm^{-1}, $B > 0.05$ T is required.

Depolarization near $\Delta \sim \frac{3}{2}\zeta$ in the absence of a field has been previously observed. In the work of Zei et al. [64], theory predicted $P_L \sim 60\%$ for $\Delta \sim \frac{3}{2}\zeta$, but their measurement revealed a dip to $P_L \sim 0\%$. Cook et al. [65] have recently attributed this depolarization to collisional processes occurring in the relatively high density ($\sim 10^{16}$ cm^{-3}) conditions of Zei et al.'s experiment. The depolarization may be the result of collisional disalignment of the $3p\ ^2P_{\frac{3}{2}}$ level. Cook et al. [65] performed a similar two-photon polarization experiment, but with a gas cell containing Na at a density of $\sim 10^{11}$ cm^{-3}. They obtained $P_L = 58\%$ at $\Delta = \frac{3}{2}\zeta$ (Note Cook et al. defined the detuning with respect to the $^2P_{\frac{3}{2}}$ level) in close agreement with theory. They next introduced Ar as a buffer gas in the Na cell and measured P_L as a function of pressure. A depolarization increase was observed at $\Delta \sim \frac{3}{2}\zeta$ with increasing Ar gas pressure. This suggests that to investigate the magnetic effects proposed here, densities of $\lesssim 10^{11}$ cm^{-3} would be necessary to minimize collisional depolarization. Collision induced transitions between ^2P_j Zeeman levels in strong magnetic fields have been previously investigated by Gay and Schneider [102].

In Figs. 2.3-3 and 2.3-4 the spin-orbit depolarization feature also reveals interesting magnetic-field-dependent behavior. The feature migrates toward $\Delta/\zeta = 0$ and decreases (polarization increase) with field strength, while near $B/\zeta = 30$ T/cm^{-1}, the feature has essentially vanished resulting in $P_L \sim 100\%$. This is not unexpected since at large fields the spin-orbit interaction becomes negligible in comparison with the magnetic interaction, the so-called Paschen-Back (PB) regime. But as displayed in Fig. 2.3-4 the anomalous Zeeman features continue to increase even at large fields. In a rigid application of the PB selection rules, P_L is identically 100% at all detunings. Nevertheless, the calculated Zeeman depolarization features persist into the PB region. The negative (positive) Δ feature corresponds to the $A - A$ and $A - E$

Reproduced with permission of the copyright owner. Further reproduction prohibited without permission.

($D - D$ and $D - H$) transitions which are forbidden in a strict PB formulation by the requirement that $S_A = 0$ ($S_D = 0$), but $S_A \to 0$ ($S_D \to 0$) only when $B \to \infty$. There remains some small strength in the transitions even at very large fields. This is shown in the intensity plot of Fig. 2.3-5. Whether this can be experimentally verified is questionable because of the weak strength of the "forbidden" lines, but the great utility of polarization measurements is to enhance small differences in intensity.

We now consider the hyperfine interaction. In the absence of a magnetic field, the shortest hyperfine precession times for the lowest $^2P_{\frac{3}{2}}$ and $^2P_{\frac{1}{2}}$ are 42 and 17 ns, 109 and 11 ns, and 20 and 5 ns for H, Li, and Na, respectively. Recent two-photon experiments (Cook et al. [65]) use lasers with short-pulses typically of ~ 0.5 ns. Thus negligible hyperfine precession can occur over the time scale of the experiment. If longer pulse lasers or continuous wave sources are used, hyperfine coherence will result in additional depolarization (Walkup et al. [103]). The application of a magnetic field will split the hyperfine F levels into the magnetic sublevels m_F, but the splitting will be of the order of the field-free hyperfine splittings. The multiplet will reorganize itself rapidly from a $|sIFm_F\rangle$ basis to a $|sIm_sm_I\rangle$ basis over a field range from zero to a few hundred gauss. The result will be m_s levels split only by the field-free dipole-dipole hyperfine term. We therefore suggest the hyperfine interaction, while worthy of investigation, will not contribute significantly for this application. Poustie and Dunn [104] have resolved hyperfine transitions in two-photon Na $3s\ ^2S_{\frac{1}{2}} \to 4d\ ^2D_j$ sum-frequency mixing experiments for $B < 0.4$ T.

2.3.3. Comments

Measurements of magnetic-field-dependent polarization spectra offer the interesting possibility of tracing the relative strength of the spin-orbit and magnetic interactions through the weak, intermediate, and PB regions at much higher precision than intensity measurements, which give uncertainties of $\sim 10\%$. This method also presents the opportunity to answer accurately the philosophical question: "At what

Reproduced with permission of the copyright owner. Further reproduction prohibited without permission.

Reproduced with permission of the copyright owner. Further reproduction prohibited without permission.

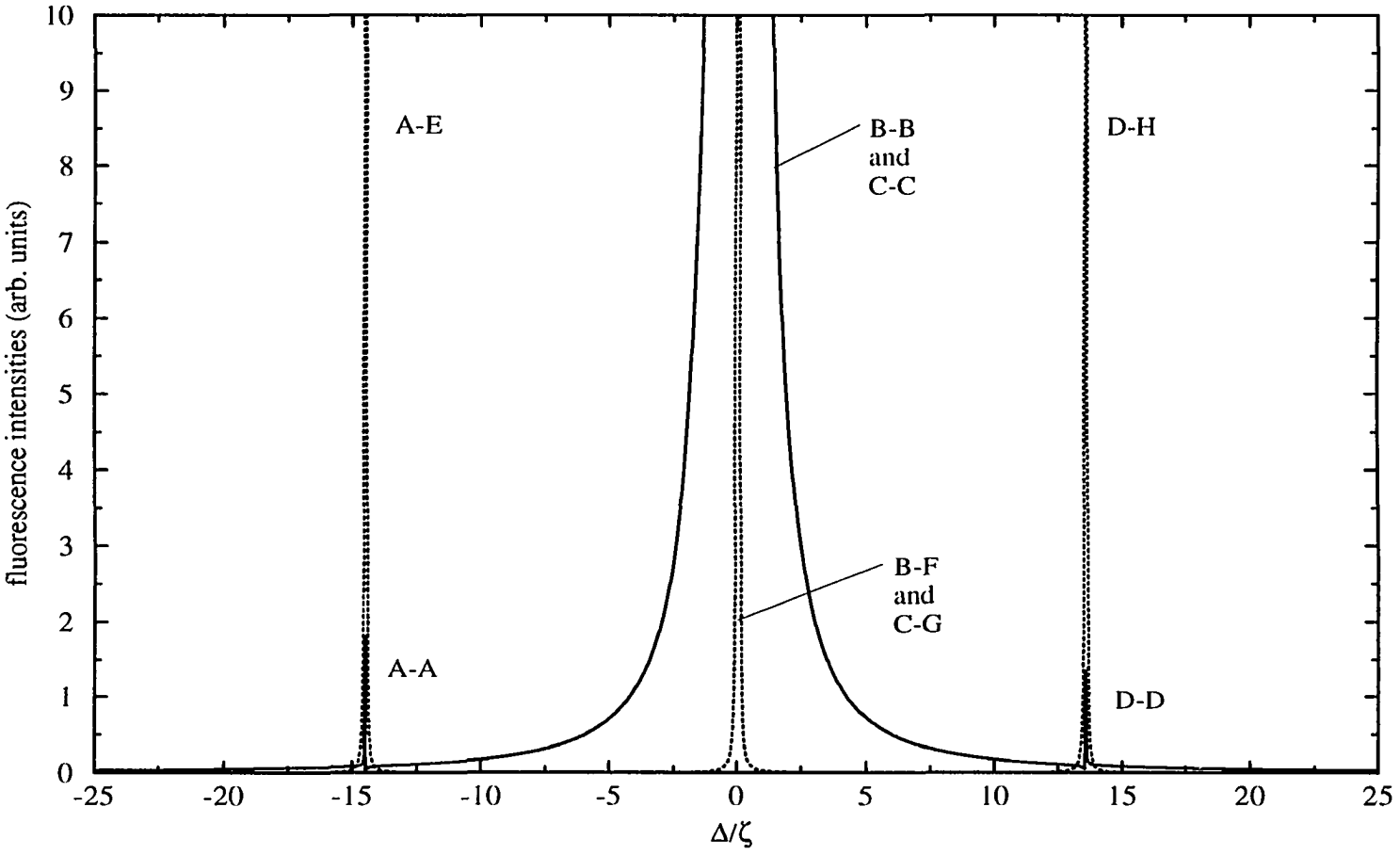

FIG. 2.3-5. Fluorescence intensity spectrum of two-photon excitation for B/ζ=30 T/cm^{-1}. The solid (dash) line is for parallel (perpendicular) photon polarization vectors. The transition labels correspond to those given in FIG. 2.3-2.

field strength is the PB criterion fully established?" The exact answer is for $B \rightarrow \infty$, but for practical applications Fig. 2.3-3 suggests that $B > 4$ T is sufficient for Li.

We comment that the Li $2s\ ^2S_{\frac{1}{2}} \rightarrow 4s\ ^2S_{\frac{1}{2}}$ scheme appears the best suited for such an investigation though its spin-orbit constant is small, $\zeta \sim 0.224$ cm^{-1}. The required excitation photon wavelengths are 670 and 497 nm, fluorescence from the $3p\ ^2P_j$ levels could be monitored at 323 nm, and the field range from weak to PB could be studied with $B < 6$ T.

Finally, this work shows that interesting magnetic-field-induced interference phenomena can occur in low-lying atomic states and without inclusion of the quadratic Zeeman effect.

Reproduced with permission of the copyright owner. Further reproduction prohibited without permission.

3. MOLECULAR CALCULATIONS

3.1. Radiative Association of He^+ and He and H^+ and H

The abundance of CO in the ejecta of supernova SN 1987A is controlled mainly through the level of element mixing and the dissociative charge exchange reaction [105]

$$He^+ + CO \rightarrow He + C^+ + O. \tag{3.1-1}$$

Lepp, Dalgarno, and McCray [105] investigated chemical models incorporating a complete mixing of the ejecta constituents and predicted CO abundances two orders of magnitude less than what is observed due to the high efficiency of process (3.1-1). A partially unmixed model involving CO clumps surrounded by He can reproduce the observed abundances by adjusting the volume fraction of the unmixed gas [106].

Removal of He^+ through radiative recombination, charge exchange, and the radiative association process

$$He^+ + He \rightarrow He_2^+(A\ ^2\Sigma_g^+) \rightarrow He_2^+(X\ ^2\Sigma_u^+) + h\nu \tag{3.1-2}$$

can reduce the effectiveness of reaction (3.1-1). The rate coefficient for process (3.1-2) has not been previously calculated, though the process has been assumed in the models of Lepp et al. [105] and Liu et al. [106] to be unimportant. They took the rate coefficient to be approximately equal to the corresponding process for hydrogen

$$H^+ + H \rightarrow H_2^+(A\ ^2\Sigma_u^+) \rightarrow H_2^+(X\ ^2\Sigma_g^+) + h\nu. \tag{3.1-3}$$

In this section, we present a calculation of the rate coefficient for the radiative association process (3.1-2) over a range of temperatures. We also give the energy-dependent cross sections calculated using a fully quantum-mechanical method for reactions (3.1-2) and (3.1-3). Published results from this section appear in Stancil,

Reproduced with permission of the copyright owner. Further reproduction prohibited without permission.

Babb, and Dalgarno [107] including the implications of process (3.1-2) to the ejecta of supernova SN 1987A, the abundance of He_2^+ in the planetary nebula NGC 7027, and the chemistry of the early universe.

3.1.1. Theory

The direct radiative association of two atomic species to form a molecule can occur when the species approach with a relative energy E in an excited electronic state of the molecule. The particles, initially in the vibrational continuum of the excited electronic state, decay to a bound rotational-vibrational (RV) level of a lower bound electronic state through spontaneous emission thereby forming a molecule.

We will be considering only the $^2\Sigma^+$ states which obey the rules of Hund's case (b) [108]. The electronic spin **S** and the internuclear axis are not coupled so that the total angular momentum **J** is related to the nuclear angular momentum **N** through the relation $J = N + S, N + S - 1, \ldots, |N - S|$.

The initial state with momentum $\hbar k'$ can be described as a superposition of partial waves characterized by N', where $k'^2 = 2\mu E/\hbar$ and μ is the reduced mass of the colliding system. The final RV levels are labeled by the vibrational quantum number v'' and $N'' = N' \pm 1$. The photon energy $E_{\rm ph} = h\nu = E + E_{v''N''}$, where ν is the photon frequency and $E_{v''N''}$ is the binding energy of the $v''N''$ RV level.

The quantum-mechanical radiative association cross section is given by [109]

$$\sigma(E) = \sum_{N'} \sum_{v''} \sigma_{N'}(v'', E), \tag{3.1-4}$$

where

$$\sigma_{N'}(v'', E) = \frac{64}{3} \frac{\pi^5}{c^3} \frac{\nu^3}{k'^2} p[N' M^2_{v'',N'-1;k',N'} + (N'+1) M^2_{v'',N'+1;k',N'}] \tag{3.1-5}$$

is the partial cross section and

$$M_{v'',N'';k',N'} = \int \chi^*_{v'',N''}(R) D_{fi}(R) \chi_{k'N'}(R) dR \tag{3.1-6}$$

is the matrix element of the transition dipole moment given by

Reproduced with permission of the copyright owner. Further reproduction prohibited without permission.

$$D(R) = \int \psi_f^*(\mathbf{r}|R)\ \mathbf{d}\ \psi_i(\mathbf{r}|R)d\mathbf{r}. \tag{3.1-7}$$

ψ_i is the initial continuum electronic wave function, ψ_f the final bound electronic wave function, R the internuclear distance, $\mathbf{d}$ the dipole operator, and p the probability of approach in the initial electronic state. The final bound RV wave function $\chi_{v''N''}(R)$ and the initial continuum RV wave function $\chi_{k'N'}(R)$ are solutions of the appropriate radial nuclear Schrödinger equation (for a review see Kirby and van Dishoeck [110]) with the bound wave function normalized to unity and the continuum wave function having the asymptotic form

$$\chi_{k'N'}(R) \sim \left(\frac{2\mu}{\pi k'}\right)^{\frac{1}{2}} \sin(k'R - \frac{1}{2}N'\pi + \eta_{N'}), \tag{3.1-8}$$

where $\eta_{N'}$ is a phase shift. The energy eigenvalues $E_{v''N''}$ are obtained by solution of the Schrödinger equation through Numerov techniques [111].

For the systems considered here, He_2^+ and H_2^+, the transition is from the first excited electronic state to the ground electronic state, $X\ ^2\Sigma^+ \leftarrow A\ ^2\Sigma^+$, and p is $\frac{1}{2}$. Using the reduced masses $\mu(H_2^+) = 918.3263$ and $\mu(He_2^+) = 3647.8995$ and the appropriate constants, Eq. (3.1-5) may be written as

$$\sigma_{N'}(v'', E) = c_1(\mathrm{x})\frac{E_{\mathrm{ph}}^3}{E}p[N'M^2_{v'',N'-1;k',N'} + (N'+1)M^2_{v'',N'+1;k',N'}], \tag{3.1-9}$$

with $c_1(H_2^+) = 5.56845 \times 10^{-9}$ and $c_1(He_2^+) = 1.40182 \times 10^{-9}$.

The rate coefficient at a temperature T is given by

$$\alpha(T) = \left(\frac{8}{\mu\pi}\right)^{\frac{1}{2}}\left(\frac{1}{k_\mathrm{b}T}\right)^{\frac{3}{2}}\int_0^\infty E\sigma(E)\exp(-E/k_\mathrm{b}T)dE \tag{3.1-10}$$

or

$$\alpha(T) = c_2(\mathrm{x})T^{-\frac{3}{2}}\int_0^\infty E\sigma(E)\exp(-E/k_\mathrm{b}T)dE\ \ \mathrm{cm^3s^{-1}}, \tag{3.1-11}$$

where k_b is the Boltzmann constant, $c_2(H_2^+) = 5.72431 \times 10^{-2}$, and $c_2(He_2^+) = 2.87210 \times 10^{-2}$.

Reproduced with permission of the copyright owner. Further reproduction prohibited without permission.

3.1.2. Molecular Data

3.1.2.1. The Hydrogen Molecular Ion. The exact nonrelativistic Born-Oppenheimer potentials for the initial $A\ ^2\Sigma_u^+$ and final $X\ ^2\Sigma_g^+$ states were obtained using the code of Power [112] and the $X \leftarrow A$ transition dipole moment using other methods out to a internuclear distance of 50 [113]. The results were checked using available tabulations [114,115]. Beyond $R = 50$, the long range form of the potentials, $-\alpha_d/2R^4$, and the dipole moment, $\frac{1}{2}R$, were used. The dipole polarizability α_d is equal to 4.5 for hydrogen [116]. The integration for the continuum wave function was carried out over the interval $R = 0.3$ to $R = 100$. The potentials and transition moment are displayed in Figs. 3.1-1 and 3.1-2, respectively.

3.1.2.2. The Helium Molecular Ion. The potentials of Metropoulos et al. [117] were used between $R = 0.8$ and $R = 4$ for both the X and A states. Data between $R = 5$ and $R = 100$ as well as extrema and asymptotes for the two potentials were taken from the "uncorrected" curves of Ackermann and Hogreve [118]. Supplemental data for the ground state between $R = 6$ and $R = 15$ were taken from Metropoulos and Nicolaides [119] and Bauschlicher, Partridge, and Ceperley [120] and similarly for the excited state between $R = 4.6$ and $R = 6$ from Metropoulos, Nicolaides, and Buenker [121]. All of the above cited potentials were obtained using *ab initio* multireference configuration-interaction (MRD-CI) methods and therefore justify the compilation. Additional short range points between $R = 0.378$ and $R = 0.75$ from the early *ab initio* calculation of Gupta and Matsen [122] were included in both states.

The long range form was adopted from the model potential of Peach [123] with the inclusion of the van der Waals term and is given by

$$V_L(R) = \mu' R^4 \exp(-\lambda' R) - \frac{\alpha_d}{2R^4} - \frac{\alpha_q'}{2R^6} - \frac{C_6}{R^6}, \qquad (3.1\text{-}12)$$

where C_6 is the van der Waals constant, which was determined [113] using the effective transition energies and oscillator strengths for He^+ and He given by Johnson, Epstein,

Reproduced with permission of the copyright owner. Further reproduction prohibited without permission.

Reproduced with permission of the copyright owner. Further reproduction prohibited without permission.

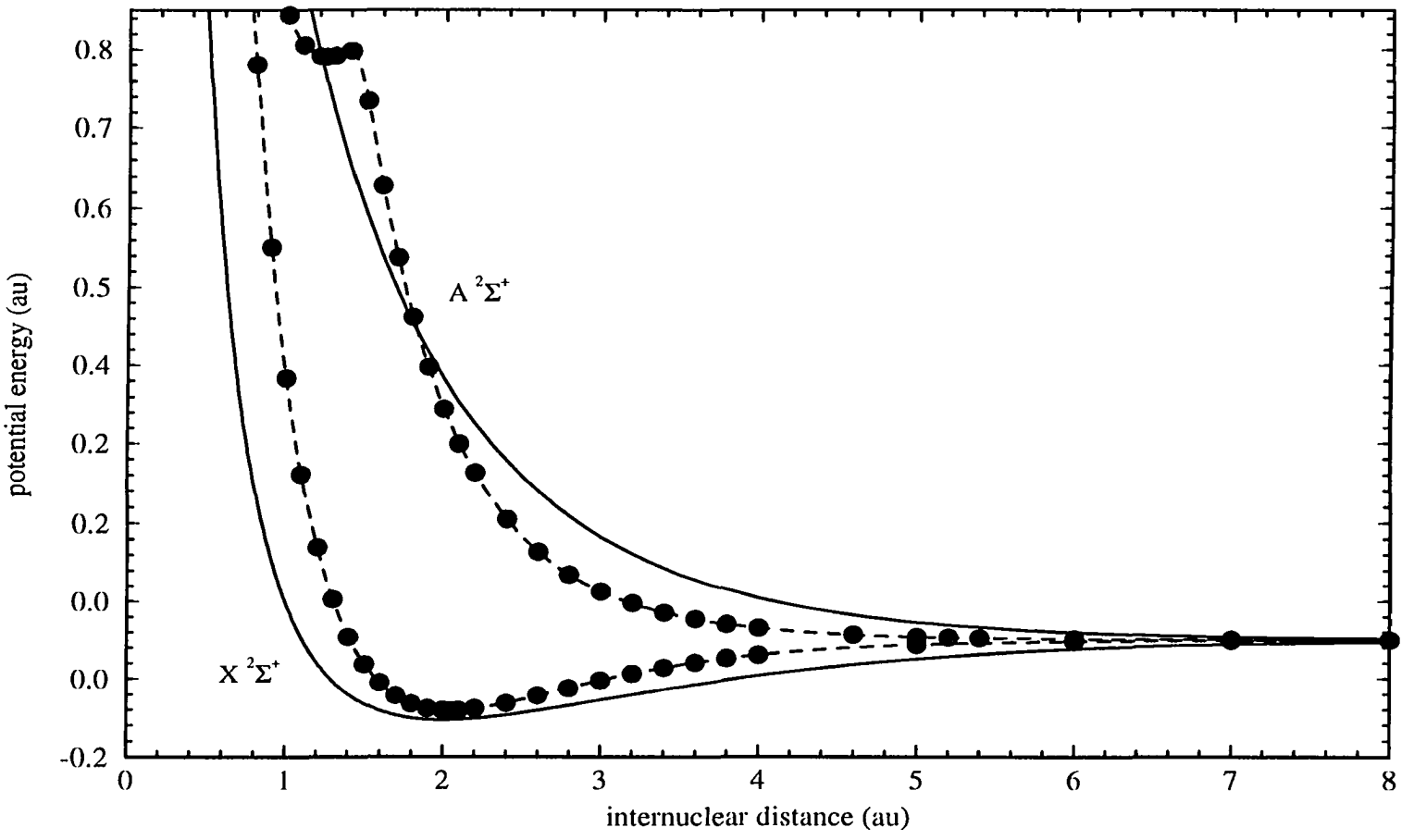

FIG. 3.1-1. Born-Oppenheimer potentials. H_2^+ is given by the full lines. The filled circles are ab initio data for He_2^+. See text. A spline fit is given by the dashed lines for He_2^+.

Reproduced with permission of the copyright owner. Further reproduction prohibited without permission.

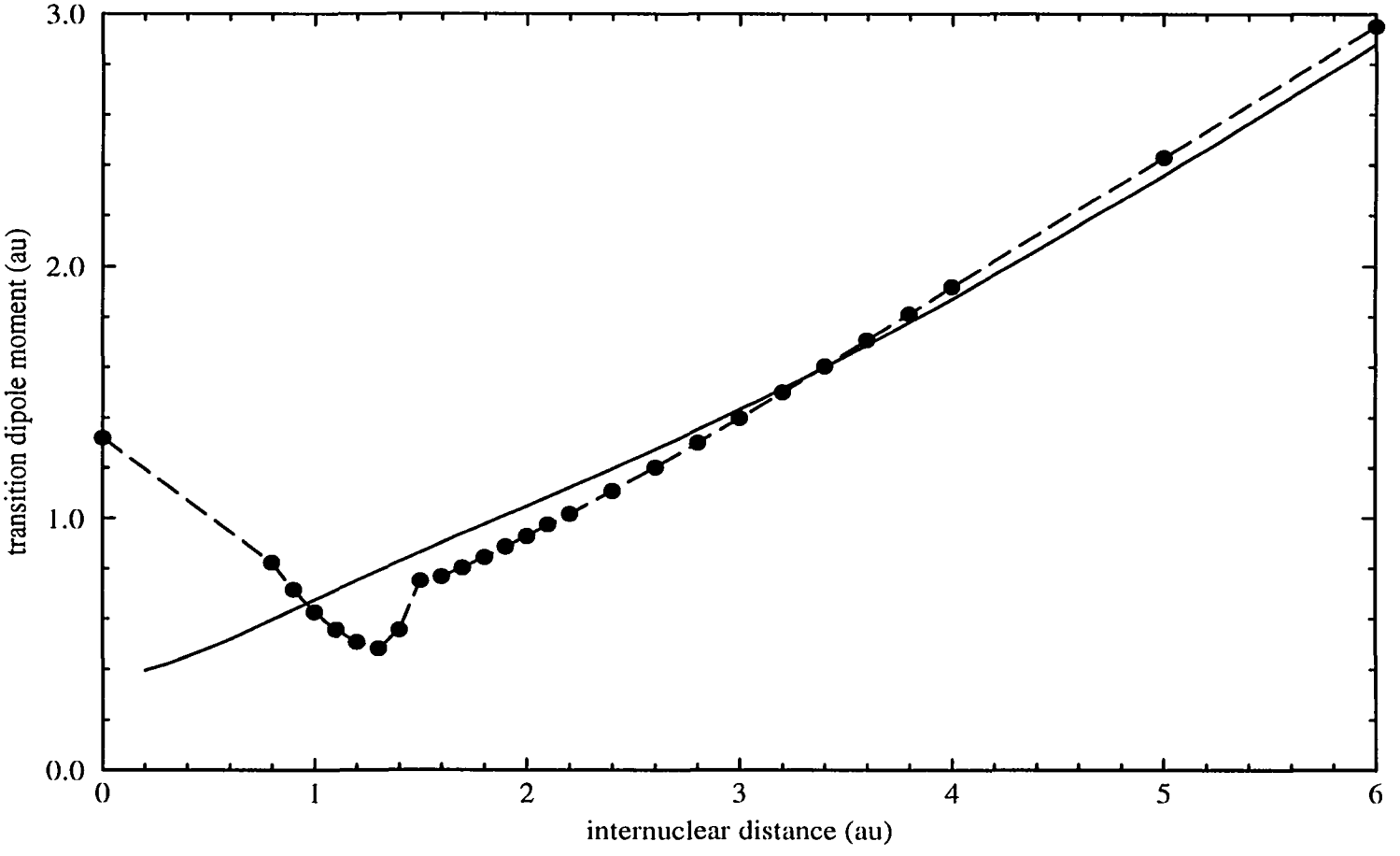

FIG. 3.1-2. X $^2\Sigma^+$- A $^2\Sigma^+$ transition dipole moment. H_2^+ is given by the full line. The filled circles are ab initio data for He_2^+. See text. A spline fit is given by the dashed line.

and Meath [124]. The parameters α_q', μ', and λ' were determined by Peach [123] and are reproduced in Table 3.1-1. The long range form was matched to the *ab initio* data at $R = 12$. The adopted potentials are displayed in Fig 3.1-1.

The transition dipole moment data of Metropoulos et al. [117] cover the interval from $R = 0.8$ to $R = 4$. They were extended to $R = 10$ using the results of McLaughlin et al. [125]. The Be^+ moment of 1.32, derived from data of Wiese, Smith, and Glennon [126], was used at $R = 0$, the united atom limit [113]. Beyond $R = 10$, the dipole moment has the long range form $\frac{1}{2}R$. As for the H_2^+ case, the integration over the continuum wave function extended from $R = 0.5$ to $R = 100$. The adopted transition moment is shown in Fig. 3.1-2. The discontinuity of the transition moment near $R = 1.5$ is due to an avoided crossing of the $A\ ^2\Sigma_g^+$ and $2^2\Sigma_g^+$ states [117].

The $X\ ^2\Sigma_u^+$ potential was tested by computing for $^3He^4He^+$ the frequencies of the $(v'' = 1, N'') \leftarrow (v'' = 0, N'' - 1)$ RV transitions and comparing them to the experimentally measured values of Yu and Wing [127]. The discrepancy was within 4 cm^{-1} or 0.2% for all transitions. A similar comparison cannot be made for the $A\ ^2\Sigma_g^+$ state since it is essentially repulsive.

The ^4He nucleus has nuclear spin zero and obeys Bose statistics which require the total nuclear wave function to be symmetric. The nuclear spin wave function is symmetric. For the $X\ ^2\Sigma_u^+$ state the nuclear coordinate wave function is symmetric for odd N'' and antisymmetric for even N''. The even N'' levels are unpopulated and since $N' = N'' \pm 1$ the sum in Eq. (3.1-4) is only taken over even N' [128].

3.1.3. Results

The radiative association cross sections $\sigma(E)$ given by Eq. (3.1-4) are shown in Fig. 3.1-3 for reactions (3.1-2) and (3.1-3). To my knowledge, no other published cross sections for these two systems exist. The similarity in the shape of the cross sections is related to the potentials and transition dipole moments of the two systems. The ground states for both molecules are attractive with minima near $R = 2$, while

Reproduced with permission of the copyright owner. Further reproduction prohibited without permission.

the excited states are essentially repulsive.

The maximum cross section occurs at a relative energy of 5.5 eV for both systems and is due to the large density of final RV states at energies corresponding to vertical transitions at the $R = 2$ minimum. The cross sections quickly drop for energies greater than about 10 eV as the bound RV states become inaccessible due to the vanishing Franck-Condon overlap. The cross section minimum occurs at 3 meV for both systems.

Enhancements occur at 0.14 meV and 0.34 meV for H_2^+ and He_2^+, respectively. These are attributed to orbiting of the atomic species within a rotationally-enhanced van der Waals well of the excited state. The particles approach at an energy E slightly above a rotational barrier produced by the potential $N'(N'+1)/2\mu R^2$. After reaching the turning point of the nuclear repulsive wall, there is a probability that the particles will be turned again at the rotational barrier. They may then "bounce around" for some time within the well before escaping over the barrier and flying apart. The interaction time of the particles is increased which in turn increases the

TABLE 3.1-1. Parameters used in the long range potentials of He_2^+.

α_d	1.38309[a]
α'_q	2.11380[b]
C_6	0.374[c]
$X\ ^2\Sigma_u^+$:	
μ'	−0.314918[b]
λ'	2.12809[b]
$A\ ^2\Sigma_g^+$:	
μ'	4.19449[b]
λ'	2.88960[b]

[a]From Ref. [116]
[b]From Ref. [123]
[c]Determined using data Ref. [124]

Reproduced with permission of the copyright owner. Further reproduction prohibited without permission.

Reproduced with permission of the copyright owner. Further reproduction prohibited without permission.

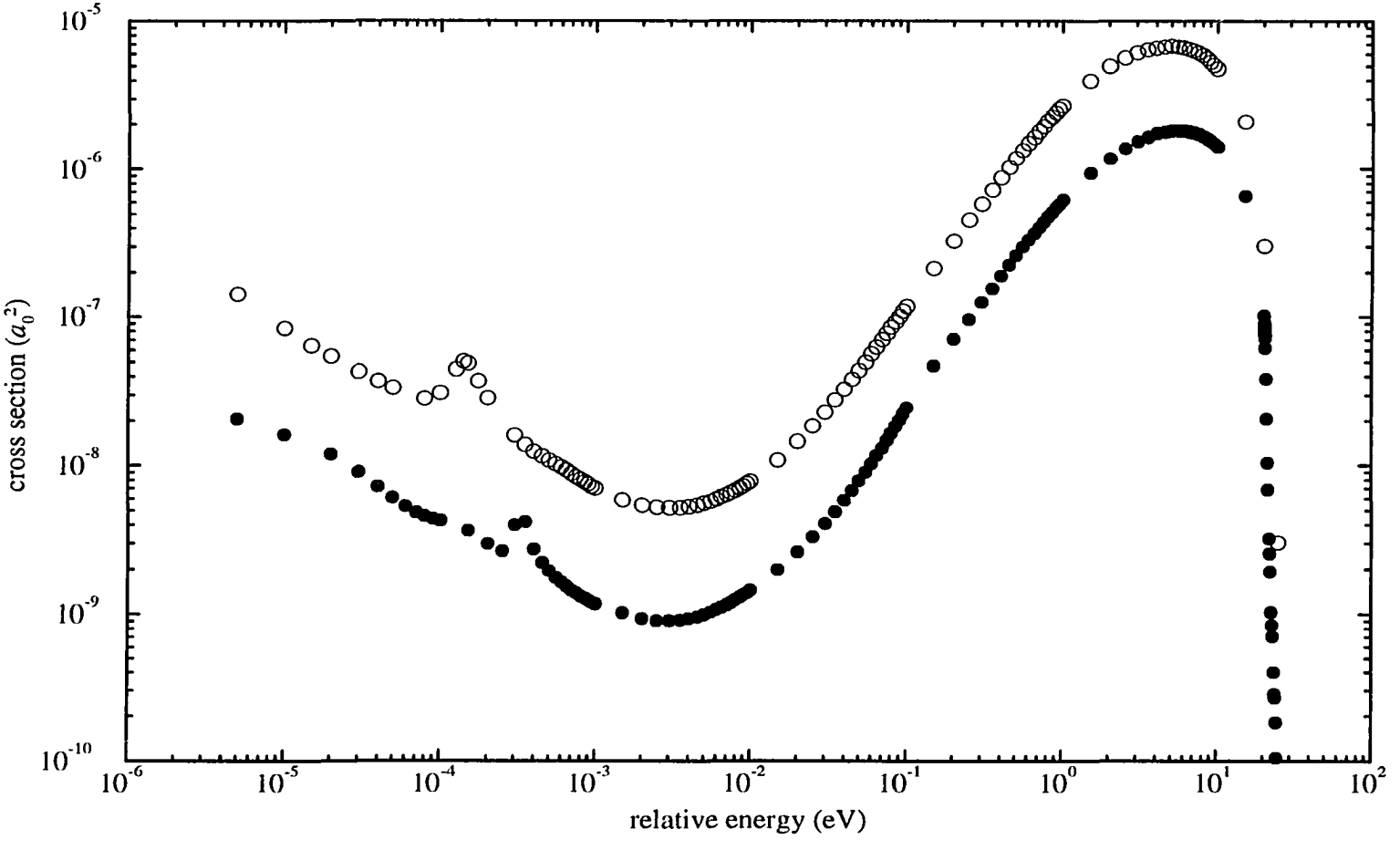

FIG. 3.1-3. The cross sections for radiative association as a function of relative energy. Reaction (3.1-2), $He^+ + He$, is given by the filled circles, while reaction (3.1-3), $H^+ + H$, is given by the open circles.

probability of a spontaneous emission and therefore enhances the cross section. The difference in the energy of the features between H_2^+ and He_2^+ is related to the internuclear distance where the van der Waals minima occur: 12.55 and 8.85, respectively. For H_2^+, the enhancement is caused primarily by the $N' = 3$ barrier which contributes 66.7% of the total cross section at the resonance energy with some contribution from $N' = 2$ (15.1%) and $N' = 1$ (12.6%). About 58% of the cross section resonance arises from only four transitions originating from $N' = 3$: $v'' = 17, N'' = 2$ (18.9%); $v'' = 17, N'' = 4$ (14.8%); $v'' = 16, N'' = 2$ (14.0%); and $v'' = 16$, $N'' = 2$ (10.2%). The major contributor for the He_2^+ enhancement is $N' = 6$ (59.3%) with additional contribution from $N' = 4$ (19.1%) and $N' = 2$ (17.4%). The four major transitions, which originate from $N' = 6$, are $v'' = 21, N'' = 5$ (14.9%); $v'' = 21, N'' = 7$ (7.5%); $v'' = 20, N'' = 5$ (11.5%); and $v'' = 20$, $N'' = 7$ (11.4%). Figures 3.1-4 and 3.1-5 display the major contributing potential barriers for H_2^+ and He_2^+, respectively. There are hints of additional structure in the low-energy cross section of reaction (3.1-2), but due to the uncertainties in the coefficients used for the long range form of the potentials given by Eq. (3.1-12) further investigation is deemed unwarranted.

One would expect an additional enhancement in the cross section to appear as a shape resonance in He_2^+ near the avoided crossing in the $A\ ^2\Sigma_g^+$ state at $R = 1.395$ corresponding to a transition energy of 20.35 eV. It is absent because this internuclear distance is located within the continuum of the $X\ ^2\Sigma_u^+$ state. This is clearly seen in the high energy drop of the cross section.

The result that the H_2^+ radiative association cross section is greater than that of He_2^+ is primarily related to the different reduced masses of the two systems. From Eq. (3.1-5), the cross section scales with reduced mass as

$$\sigma_{He_2^+} \approx \sigma_{H_2^+} \frac{\mu(H_2^+)}{\mu(He_2^+)} \tag{3.1-13}$$

or $\sigma_{He_2^+} \approx \sigma_{H_2^+}/4$. The qualitative differences between the H_2^+ and He_2^+ also contribute to the larger magnitude of the H_2^+ cross section. The difference in energy between the

Reproduced with permission of the copyright owner. Further reproduction prohibited without permission.

Reproduced with permission of the copyright owner. Further reproduction prohibited without permission.

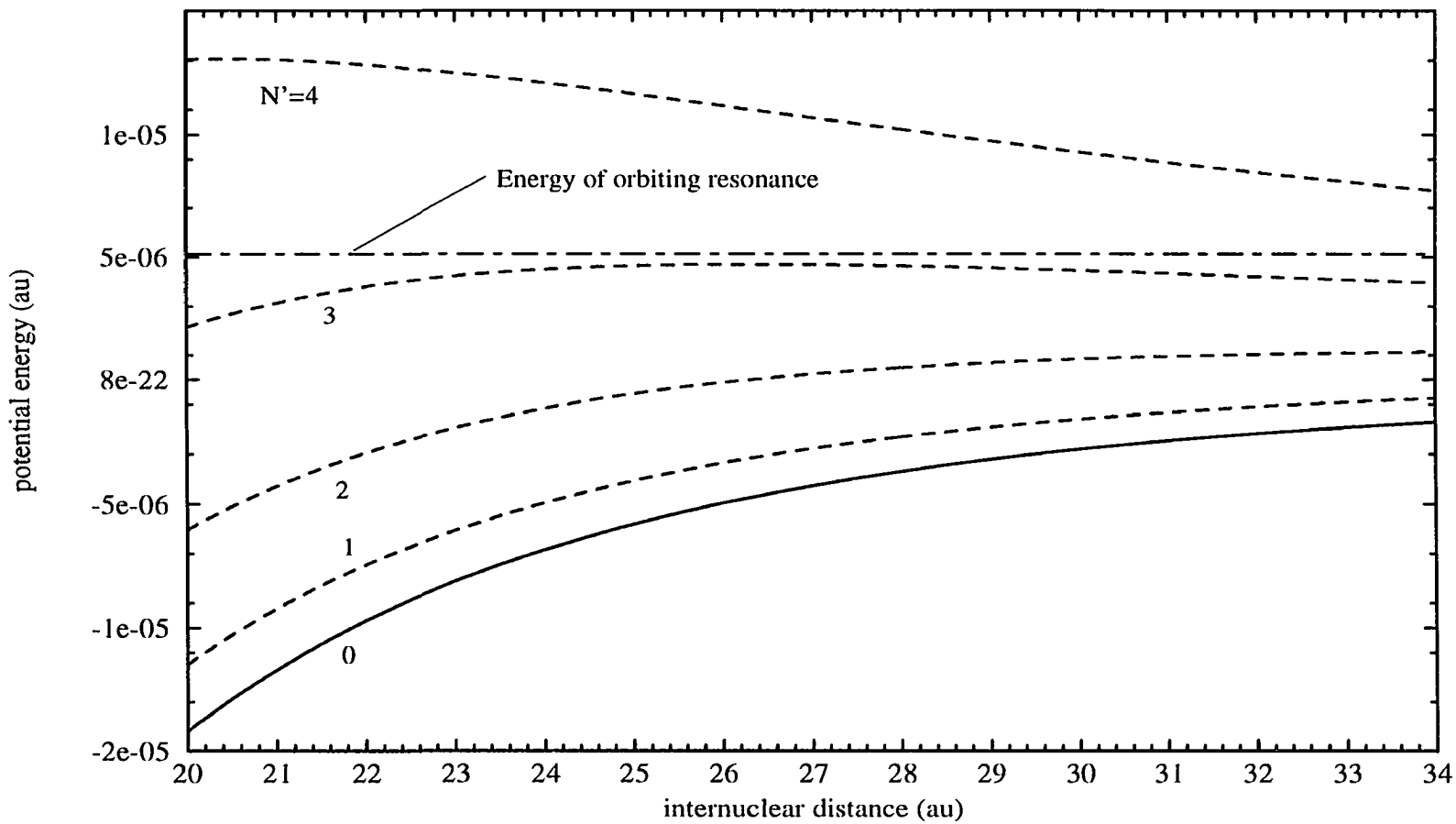

FIG. 3.1-4. Born-Oppenheimer plus rotational potentials for the $A\ ^2\Sigma_u^+$ state of H_2^+.

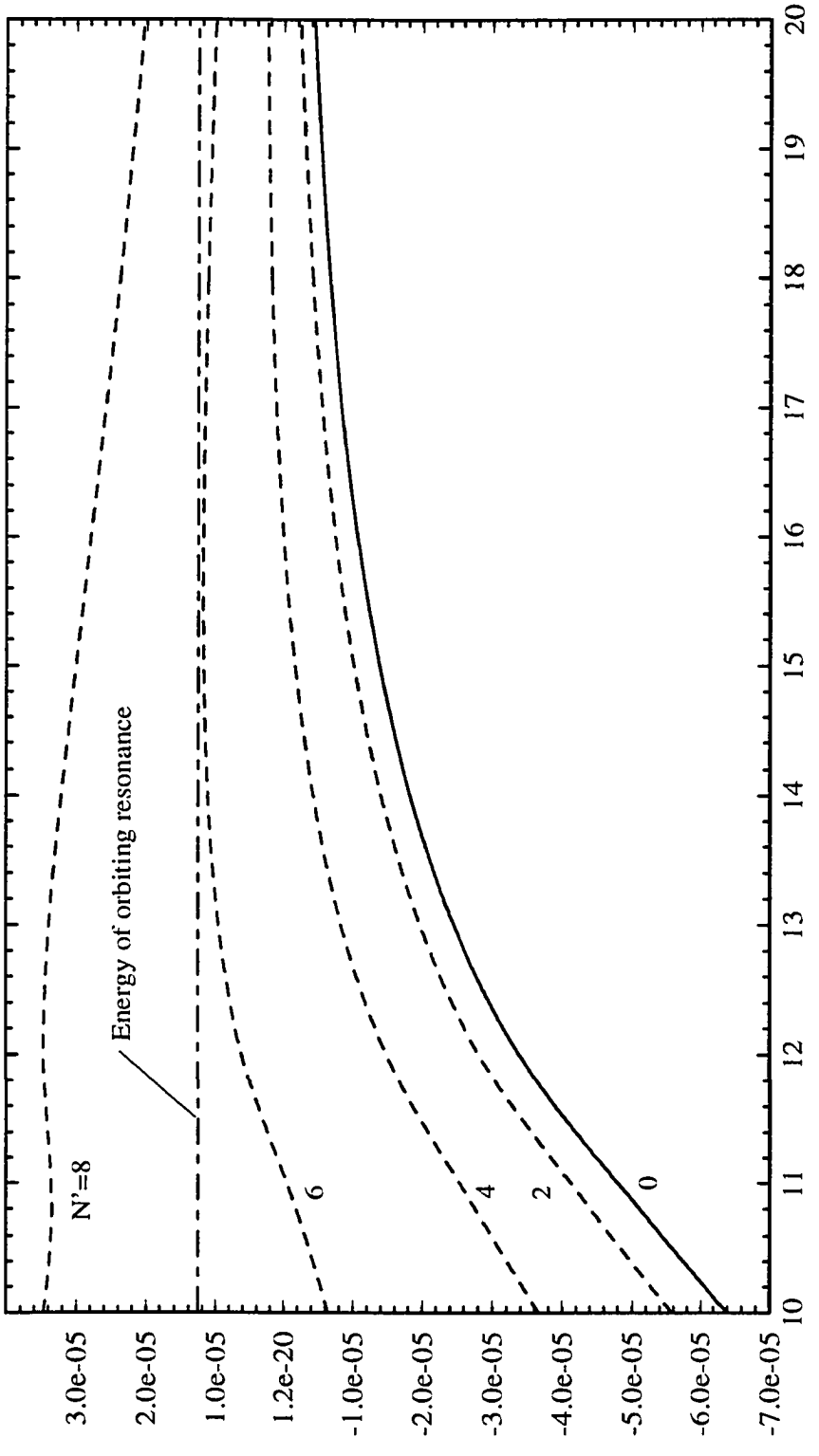

FIG. 3.1-5. Born-Oppenheimer plus rotational potentials for the $A\,^2\Sigma_g^+$ state of He_2^+.

Reproduced with permission of the copyright owner. Further reproduction prohibited without permission.

He_2^+ potentials is generally less than for the H_2^+ potentials causing the photon energy E_{ph} to be less for He_2^+ and as a consequence $\sigma_{He_2^+}$ is reduced.

Since the even N'' levels of He_2^+ are not populated one might expect the cross section to be further reduced. This does not play a role because there are a comparable number of populated RV levels in the ground states of the systems: 423 for H_2^+ and 411 for He_2^+. As noted by Ramaker and Peek [129], the $v'' = 19, N'' = 0$ state of H_2^+ is a major contributor to the cross section for energies less than ~ 0.1 meV. At high energies for both systems, we observe that the cross section contributions tend to equalize among the individual RV states so that it becomes important to ensure that all states are accounted for. Table 3.1-2 gives the maximum N'' for each v'' included in the calculations.

The cross sections are averaged over a Maxwellian velocity distribution as in equation (3.1-10) to give the rate coefficients. The integration is performed by Gauss-Legendre quadrature [71]. The results for He_2^+, reaction (3.1-2), and H_2^+, reaction (3.1-3), are shown in Figure 3.1-6 with some numerical values given in Table 3.1-3. Our calculated rate coefficients for H_2^+ agree to within 3% with those given by Ramaker and Peek [129] for temperatures above 20 K. Temperatures below 20 K were investigated, but the coefficients given by Ramaker and Peek were as much as 25% larger. The origin of the discrepancy is unclear but may be due to adiabatic corrections presumably incorporated in Ref. [129], though we do include the same number of RV states.

An analytic fit to the coefficients for reaction (3.1-3) gives to within 25%

$$\alpha_{H_2^+}(T) = 1.9 \times 10^{-20} T^{-0.064} \exp(-T/45) + 3.5 \times 10^{-23} T^{1.7} \exp(-T/28800) \text{ cm}^3\text{s}^{-1} \quad (3.1\text{-}14)$$

which is applicable for the temperature range 20 K to 50,000 K. This can be compared to the relation $3.4 \times 10^{-22} T^{1.5}$ cm^3s^{-1} given by Dalgarno and Lepp [130].

The rate coefficient for He_2^+ has a temperature dependence similar to H_2^+, but it

Reproduced with permission of the copyright owner. Further reproduction prohibited without permission.

TABLE 3.1-2. Maximum rotational quantum numbers N''_{max} for each vibrational quantum number v'' of the ground state used in the calculations.

Molecule	v''											
	0	1	2	3	4	5	6	7	8	9	10	11
H_2^+	35	34	33	31	30	28	27	25	24	22	20	19
He_2^+	57	57	53	51	51	49	47	45	43	41	39	37
	v''											
	12	13	14	15	16	17	18	19	20	21	22	23
H_2^+	17	15	13	11	9	6	3	1	-	-	-	-
He_2^+	33	31	29	27	23	21	19	15	11	9	5	5

Reproduced with permission of the copyright owner. Further reproduction prohibited without permission.

Reproduced with permission of the copyright owner. Further reproduction prohibited without permission.

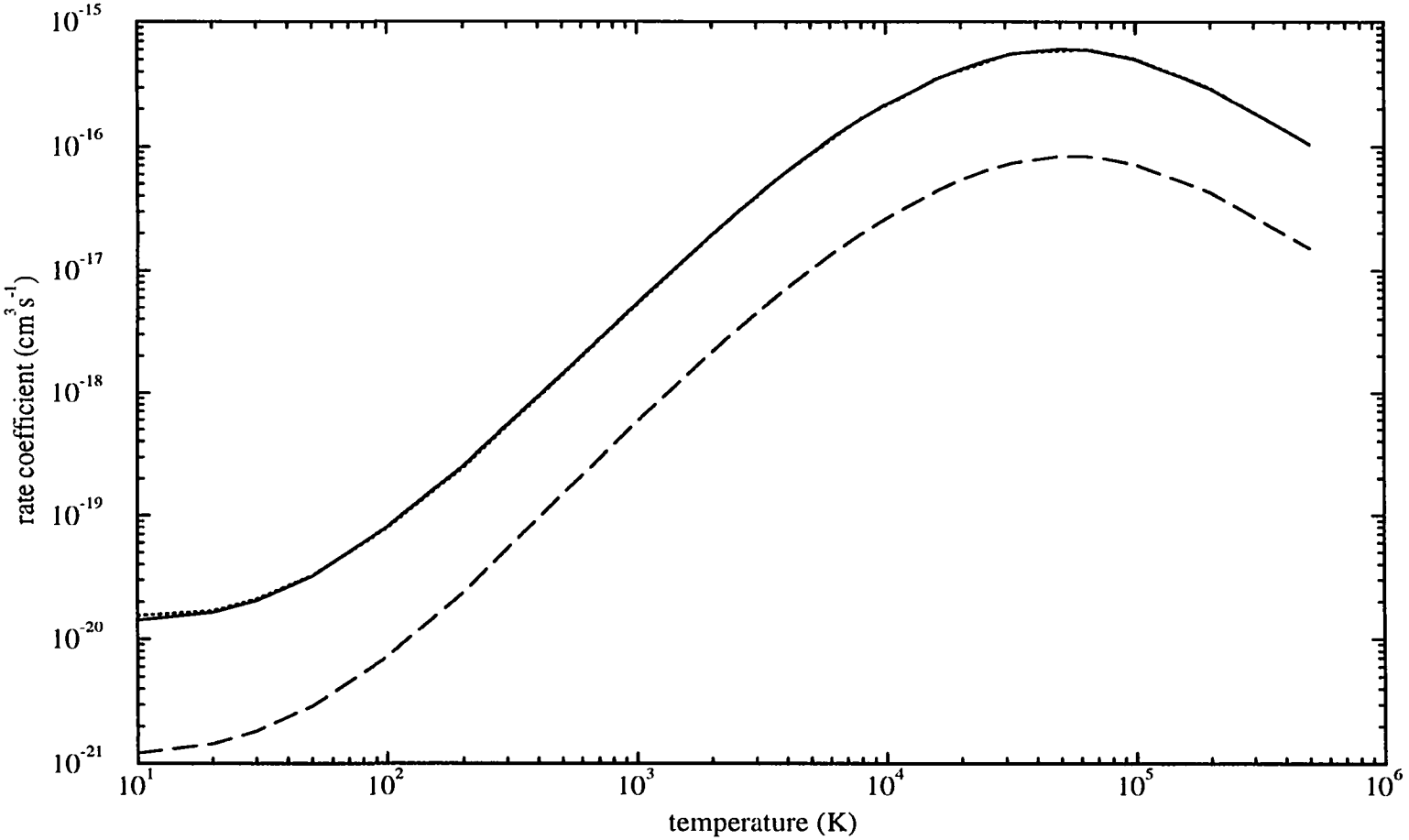

FIG. 3.1-6. The rate coefficient for radiative association as a function of temperature. Reaction (3.1-2), $He^+ + He$, is given by the dashed line, while reaction (3.1-3), $H^+ + H$, is given by the full line. The results of Ramaker and Peek are given by the dotted line for comparison.

TABLE 3.1-3. Rate coefficients for the radiative association process $x^+ + x \rightarrow x_2^+ + h\nu$.

T(K)	$\alpha(T)$ cm^3s^{-1}		
	x=H[a]	x=H[b]	x=He[b]
20	1.69-20[c]	1.65-20	1.44-21
30	2.10-20	2.05-20	1.83-21
50	3.25-20	3.22-20	2.91-21
100	7.85-20	7.95-20	7.18-21
200	2.46-19	2.52-20	2.36-20
500	1.39-18	1.42-18	1.48-19
1000	5.27-18[d]	5.41-18	5.82-19
2000	1.93-17[d]	1.95-17	2.16-18
2500	2.88-17	2.88-17	3.22-18
3000	-	3.92-17	4.42-18
4000	6.20-17[d]	6.22-17	7.13-18
6000	-	1.13-16	1.33-17
8000	1.67-16	1.66-16	1.98-17
10000	-	2.17-16	2.62-17
16000	3.53-16	3.49-16	4.39-17
20000	-	4.18-16	5.36-17
25000	-	4.85-16	6.34-17
32000	5.55-16	5.48-16	7.30-17
50000	-	6.04-16	8.29-17
64000	5.96-16[d]	5.91-16	8.23-17
100000	5.05-16[d]	5.01-16	7.11-17
200000	2.96-16[d]	2.93-16	4.24-17
500000	1.04-16[d]	1.03-16	1.51-17

[a]From Ref. [129]

[b]Present results

[c]The notation 1.69-20 corresponds to 1.69×10^{-20}

[d]Semiclassical results

Reproduced with permission of the copyright owner. Further reproduction prohibited without permission.

is approximately an order of magnitude less. This difference is related to the reduced mass ratio as previously discussed for the cross section giving the scaling relation

$$\alpha_{He_2^+} \approx \alpha_{H_2^+} \left[\frac{\mu(H_2^+)}{\mu(He_2^+)} \right]^{\frac{1}{2}} \tag{3.1-15}$$

or $\alpha_{He_2^+} \approx \alpha_{H_2^+}/8$. Equation (3.1-15) is slightly modified for high and low temperatures. Between 20 K and 50,000 K, the rate coefficient may be represented to within 25% by

$$\alpha_{He_2^+}(T) = 1.3 \times 10^{-21} T^{-0.008} \exp(-T/67) + 2.1 \times 10^{-24} T^{1.8} \exp(-T/22800) \text{ cm}^3\text{s}^{-1}. \tag{1}$$

The radiative association spectra for H_2^+ and He_2^+ at an energy of 0.75 eV are shown in Fig. 3.1-7. The spectra appear in the near infrared with maxima near 1150 nm. The lines are due to transitions to individual RV levels where the intensities are given by the partial cross section of Eq. (3.1-5). Spectra obtained at the energies of the orbiting features are shown in Fig. 3.1-8 and are dominated by four lines in the infrared between 20 and 250 μm and arise from transitions to high-lying RV levels as discussed above.

Reproduced with permission of the copyright owner. Further reproduction prohibited without permission.

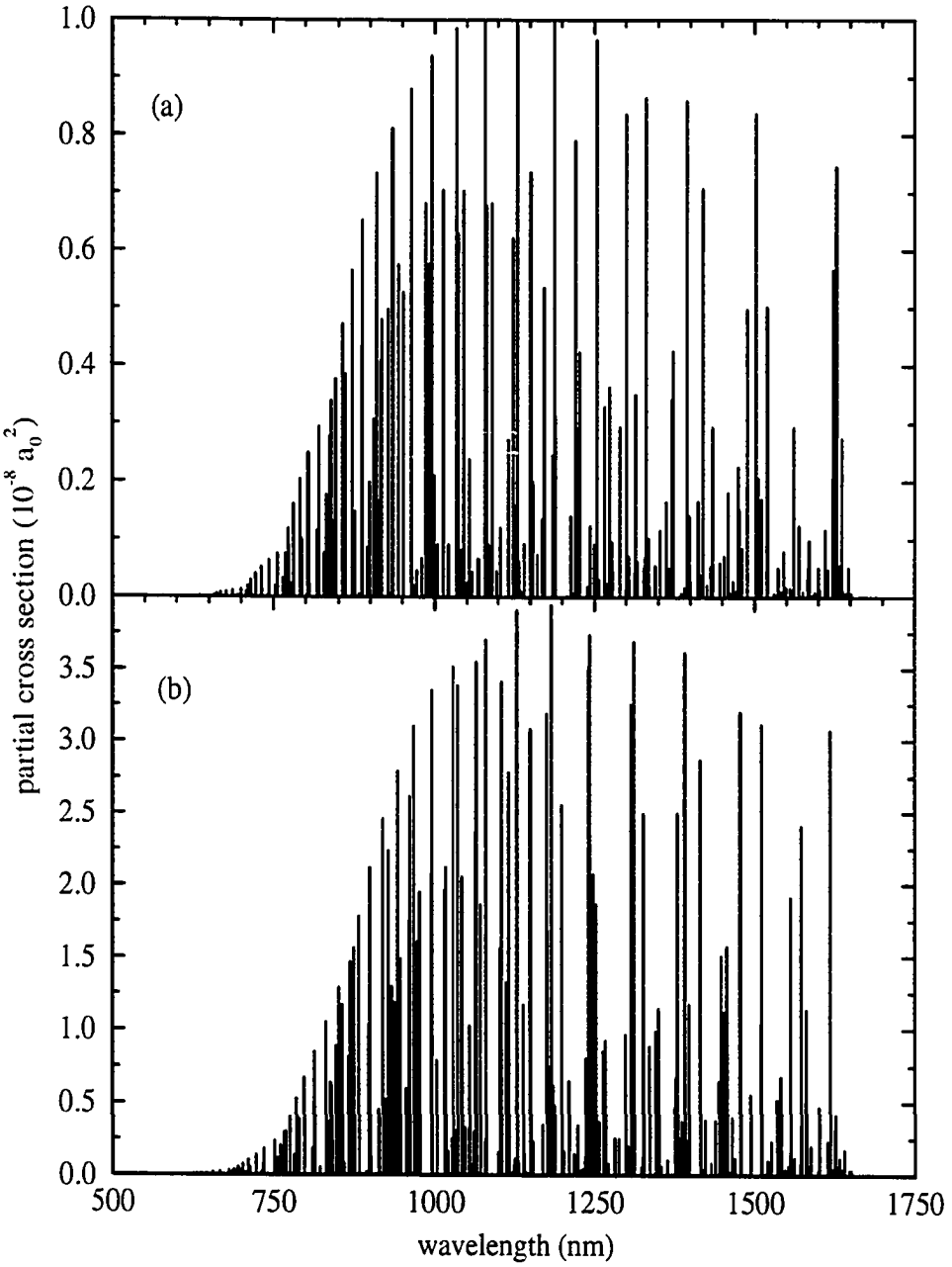

FIG. 3.1-7. Radiative association spectra at a relative energy of 0.75 eV. (a) is reaction (3.1-2), $He^+ + He$, while (b) is reaction (3.1-3), $H^+ + H$.

Reproduced with permission of the copyright owner. Further reproduction prohibited without permission.

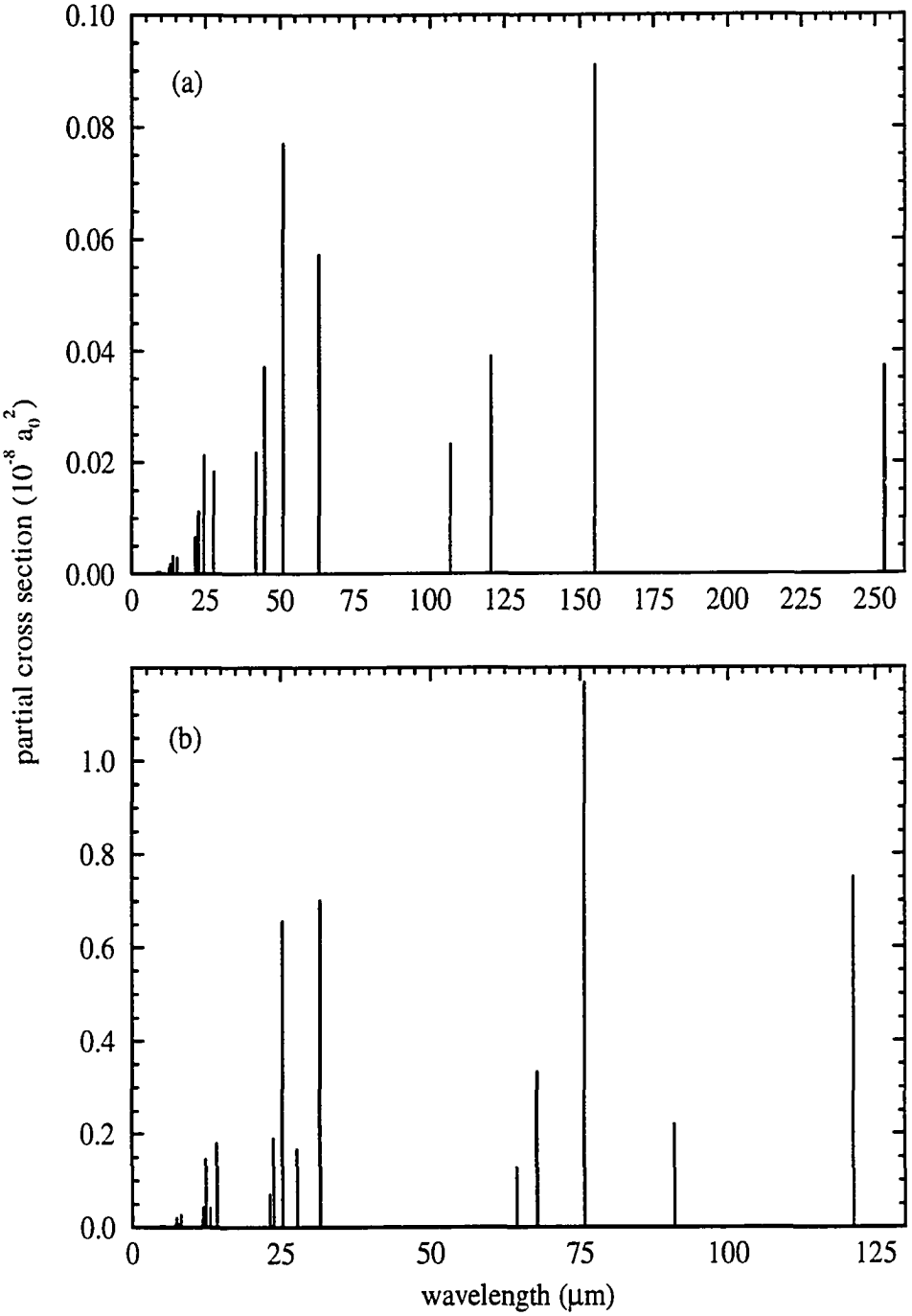

FIG. 3.1-8. Radiative association spectra at the orbiting resonance energy. (a) is reaction (3.1-2), $He^+ + He$, at 0.34 meV, while (b) is reaction (3.1-3), $H^+ + H$, at 0.14 meV.

Reproduced with permission of the copyright owner. Further reproduction prohibited without permission.

3.2. Photodissociation and Free-Free Absorption by He_2^+ and H_2^+

In the previous section, the formation of He_2^+ by radiative association was investigated. We continue our studies of this rare molecule by investigating its destruction through the photodissociation process

$$He_2^+(X\ ^2\Sigma_u^+) + h\nu \rightarrow He_2^+(A\ ^2\Sigma_g^+) \rightarrow He^+ + He, \tag{3.2-1}$$

where ν is the photon frequency. In addition, the corresponding destruction reaction for H_2^+,

$$H_2^+(X\ ^2\Sigma_g^+) + h\nu \rightarrow H_2^+(A\ ^2\Sigma_u^+) \rightarrow H^+ + H \tag{3.2-2}$$

is revisited. The wavelength- and temperature-dependent cross sections and absorption coefficients calculated using a fully quantum-mechanical method are presented for reactions (3.2-1) and (3.2-2) within the Born-Oppenheimer approximation.

In addition, absorption coefficients for the free-free processes

$$(He^+ + He)(X\ ^2\Sigma_u^+) + h\nu \rightarrow (He^+ + He)(A\ ^2\Sigma_g^+) \tag{3.2-3}$$

and

$$(H^+ + H)(X\ ^2\Sigma_g^+) + h\nu \rightarrow (H^+ + H)(A\ ^2\Sigma_u^+) \tag{3.2-4}$$

are obtained through semiclassical methods. Published results from this section are given in Ref. [131].

3.2.1. Theory and Calculations

The direct photodissociation of a molecule can occur through the absorption of a photon of wavelength λ. The molecule, initially in a bound rotational-vibrational (RV) level of the ground electronic state i, is promoted to the vibrational continuum

Reproduced with permission of the copyright owner. Further reproduction prohibited without permission.

of an excited electronic state f. The promotion can occur to a repulsive state or to the repulsive wall of an attractive state resulting in the break-up of the molecule into its constituent particles separating with relative energy E.

Following the notation of Sec. 3.1, the initial RV levels are labeled v'' and $N'' = N' \pm 1$. The photon energy $E_{\rm ph} = h\nu = hc/\lambda = E + E_{v''N''}$, where $E_{v''N''}$ is the binding energy of the $v''N''$ level.

The total quantum-mechanical cross section for photodissociation as a function of both temperature and wavelength in local thermodynamic equilibrium (LTE) is given by [132]

$$\sigma(\lambda,T) = \frac{\sum_{v''}\sum_{N''} g_{iv''N''}\exp[-(E_g - E_{v''N''})/k_{\rm b}T]\sigma_{v''N''}(\lambda)}{Q_{X_2^+}(T)}, \tag{3.2-5}$$

where [110]

$$\sigma_{v''N''}(E_{\rm ph}) = \frac{2}{3}\frac{\pi e^2}{mc}E_{\rm ph}M^2_{k'N',v''N''} \tag{3.2-6}$$

is the partial cross section from the $v''N''$ level, $g_{iv''N''}$ is the total electronic-vibrational-rotational statistical weight, $E_{\rm g}$ is the binding energy of the lowest RV level, $Q_{X_2^+}(T)$ is the partition function given by

$$Q_{X_2^+}(T) = \sum_{v''}\sum_{N''} g_{iv''N''}\exp[-(E_g - E_{v''N''})/k_{\rm b}T] \tag{3.2-7}$$

for the molecule x_2^+, where x=He or H.

The statistical weight is given by

$$g_{iv''N''} = (2 - \delta_{0,\Lambda''})(2S+1)(2N''+1)g'_{\rm nuc}, \tag{3.2-8}$$

where for the ground states of the molecules considered in this work

$$g'_{\rm nuc} = \begin{cases} (2I+1)(I+1)/g_{\rm nuc}, & \text{odd } N'', \\ (2I+1)I/g_{\rm nuc}, & \text{even } N'', \end{cases} \tag{3.2-9}$$

I is the nuclear spin, and $g_{\rm nuc} = (2I+1)^2$ is the nuclear spin statistical weight. It is convention to divide by $g_{\rm nuc}$ in the partition function definition [133].

Reproduced with permission of the copyright owner. Further reproduction prohibited without permission.

For the case of He_2^+, as discussed in Sec. 3.1.2.2, only odd N'' levels can be populated in $^4He_2^+$ so that the sums in Eq. (3.2-5) and (3.2-7) are taken only over odd N'' and $E_g(He_2^+) = E_{01}$. This can be seen from Eq. (3.2-9) since $I(He_2^+) = 0$.

If both the matrix element and the photon energy are given in atomic units, the partial cross section of Eq. (3.2-6) can be written as

$$\sigma_{v''N''}(E_{ph}) = 2.69 \times 10^{-18} E_{ph} M^2_{k'N',v''N''} \ \text{cm}^2. \tag{3.2-10}$$

The photodissociation absorption coefficient is given by

$$a(\lambda, T) = \frac{\sigma(\lambda, T)}{K(T)} \ \text{cm}^5, \tag{3.2-11}$$

where

$$\begin{aligned} K(T) &= \frac{n(\text{x})n(\text{x}^+)}{n(\text{x}_2^+)} \\ &= \left(\frac{2\pi\mu k_b T}{h^2}\right)^{\frac{3}{2}} \frac{Q_\text{X} Q_{\text{X}^+}}{Q_{\text{X}_2^+}} \exp(-D_e/k_b T) \end{aligned} \tag{3.2-12}$$

is the dissociation equilibrium constant, $n(\text{x})$ is the number density in cm^{-3}, Q_X and Q_{X^+} are the partition functions of the atom x and ion x^+ given analogous to Eq. (3.2-7), and D_e is the molecular dissociation energy.

The above derivation has neglected stimulated emission which becomes an important process for long wavelengths and high temperatures. Eqs. (3.2-3) or (3.2-11) should be multiplied by $[1 - \exp(-h\nu/k_b T)]$, the so-called LTE stimulated emission correction factor [134].

Transition dipole moments and nonrelativistic Born-Oppenheimer potentials were incorporated for both molecular ions as detailed in Sec. 3.1.2. The maximum rotational quantum numbers $N''_{\max}$ used in the sum of equations (3.2-5) and (3.2-7) were 57 and 35 giving a total of 411 and 423 RV states for He_2^+ and H_2^+ as shown in Table 3.1-2.

Reproduced with permission of the copyright owner. Further reproduction prohibited without permission.

The molecular partition functions and equilibrium constants were determined as discussed below in Sec. 3.3. The atomic partition functions incorporated in Eq. (3.2-12) are taken from Ref. [133].

3.2.2. Results

The partial photodissociation cross sections $\sigma_{v''N''}(E_{\rm ph})$ given by Eq. (3.2-10) are shown in Fig. 3.2-1 for reactions (3.2-1) and (3.2-2) for the first vibrational level and various N''. The reaction (3.2-2) cross sections agree with those given by Argyros [132].

Fig. 3.2-2 and 3.2-3 display the total cross sections $\sigma(\lambda, T)$ of Eq. (3.2-5) for processes (3.2-1) and (3.2-2), respectively, with the individual cross sections given for convenient values of θ where $\theta = 5040/T$. Numerical data are given in Tables 3.2-1 and 3.2-2. The individual cross section curves in Fig. 3.2-2 show to the author's knowledge the first quantum-mechanical calculation of He_2^+ photodissociation.

Previous work on H_2^+ by Argyros [132] incorporated only the first nine rotational levels and presumably only 166 RV levels. Using only $N''_{\rm max} = 8$, we reproduced Argyros's results which are similar to Fig. 3.2-3 (see Argyros's Fig. 6). The low-temperature $N''_{\rm max} = 8$ cross sections have a peak near 115 nm which shifts slightly to larger wavelengths with increasing temperature. For example, at 12,600 K the peak occurs at $\sim$ 140 nm. Inclusion of the higher lying rotational levels results in a more pronounced temperature-dependent wavelength shift of the peak as can be seen in Fig. 3.2-3. We obtain a peak at $\sim$ 210 nm for $T = 12,600$ K. In addition, the cross section amplitude for $\lambda \geq 200$ nm is increased and the long-wavelength oscillations for $T \geq 8400$ K found by Argyros are practically removed. It is clear, different from the assumption of Argyros, that the upper envelope of the $N''_{\rm max} = 8$ cross section does not give the correct result, but as pointed out by Buckingham, Reid, and Spence [135], all RV levels must be included. Their calculation at $T = 2500$ K includes vibrational

Reproduced with permission of the copyright owner. Further reproduction prohibited without permission.

Reproduced with permission of the copyright owner. Further reproduction prohibited without permission.

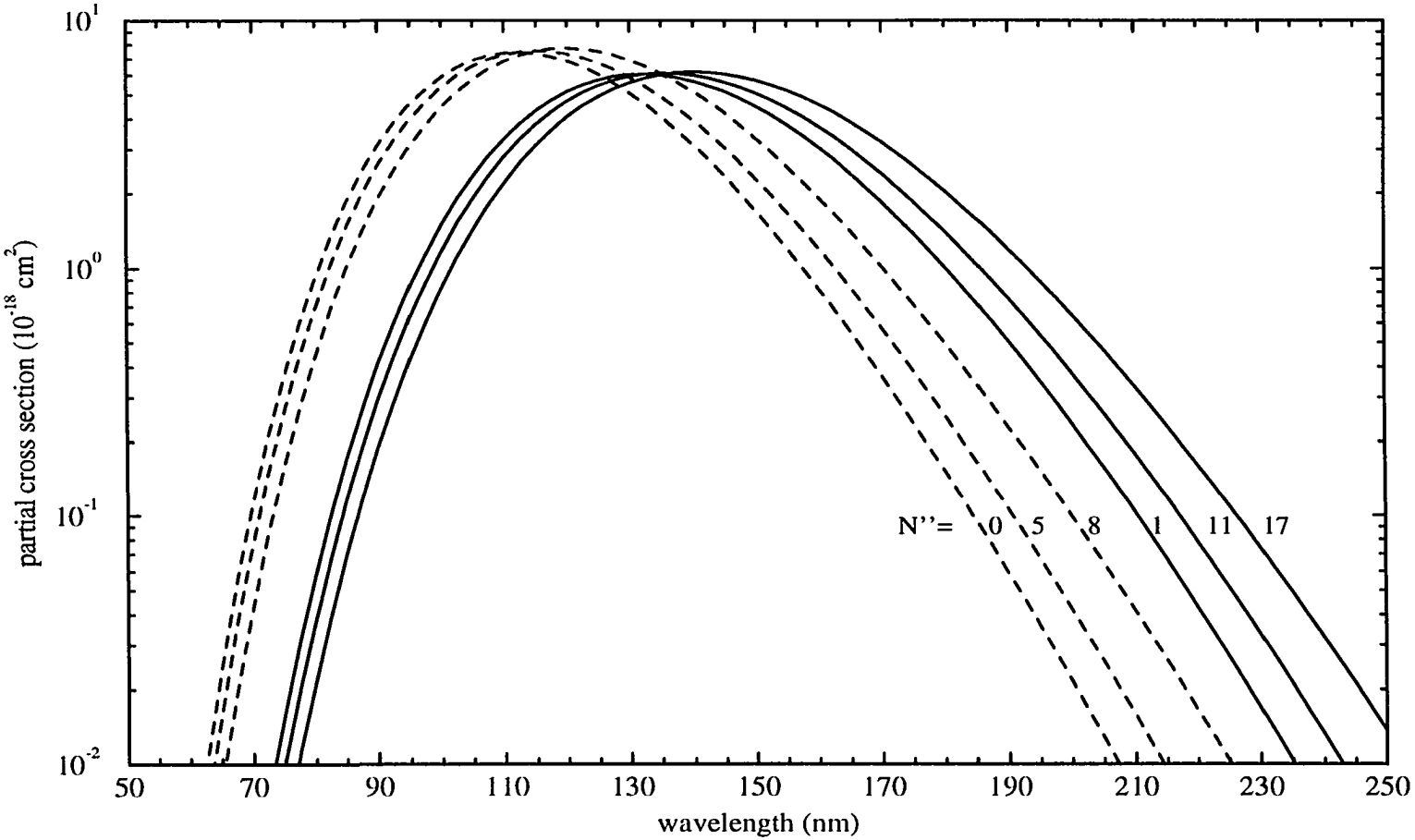

FIG. 3.2-1. Partial photodissociation cross sections for the ground vibrational level and various rotational levels. He_2^+, reaction (3.2-1), is given by the full lines, while H_2^+, reaction (3.2-2), is given by the dashed lines.

Reproduced with permission of the copyright owner. Further reproduction prohibited without permission.

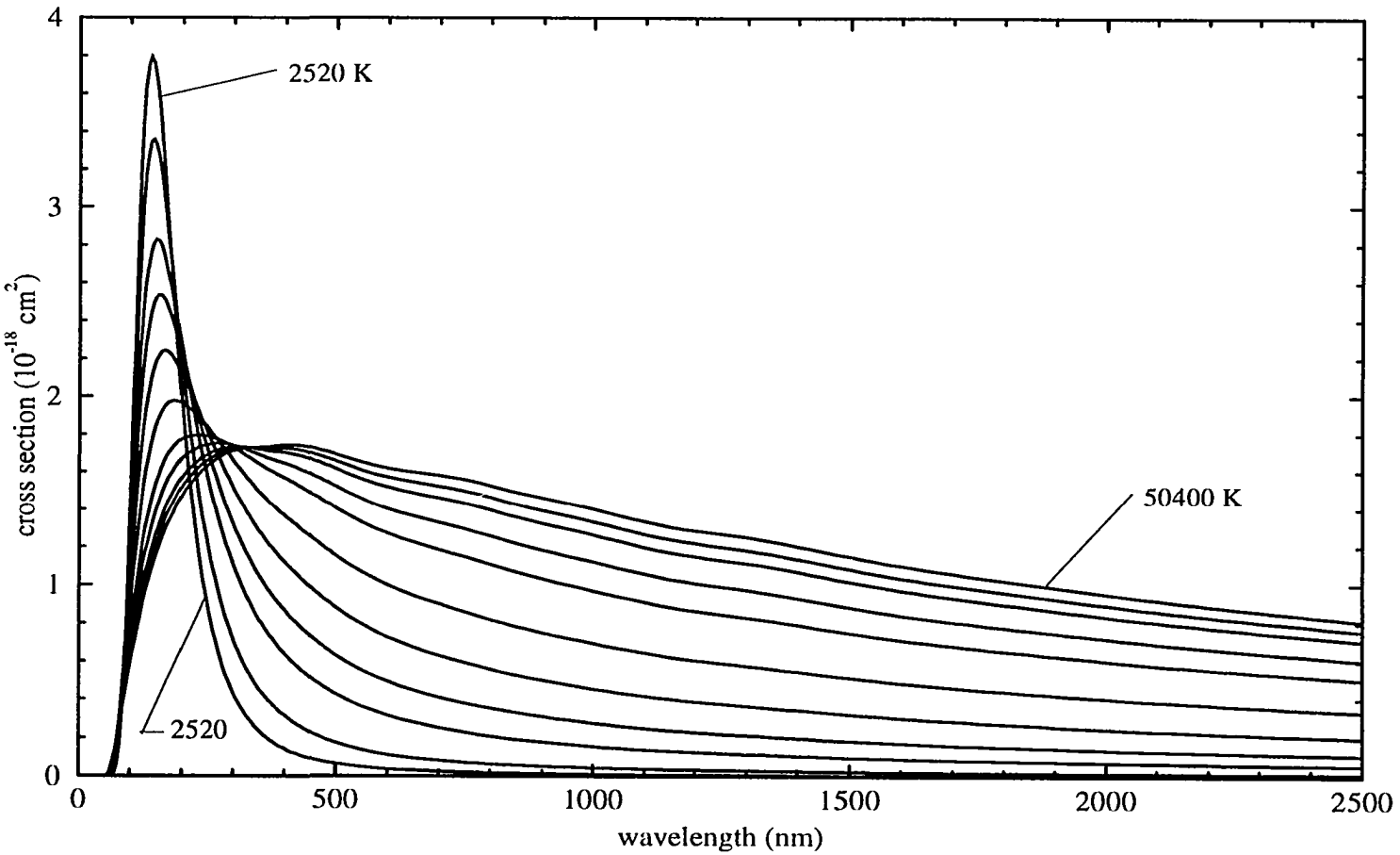

FIG. 3.2-2. Total He_2^+ photodissociation cross sections for T = 2520, 3150, 4200, 5040, 6300, 8400, 12 600, 16 800, 25 200, 33 600, and 50 400 K from bottom to top at λ = 500 nm.

Reproduced with permission of the copyright owner. Further reproduction prohibited without permission.

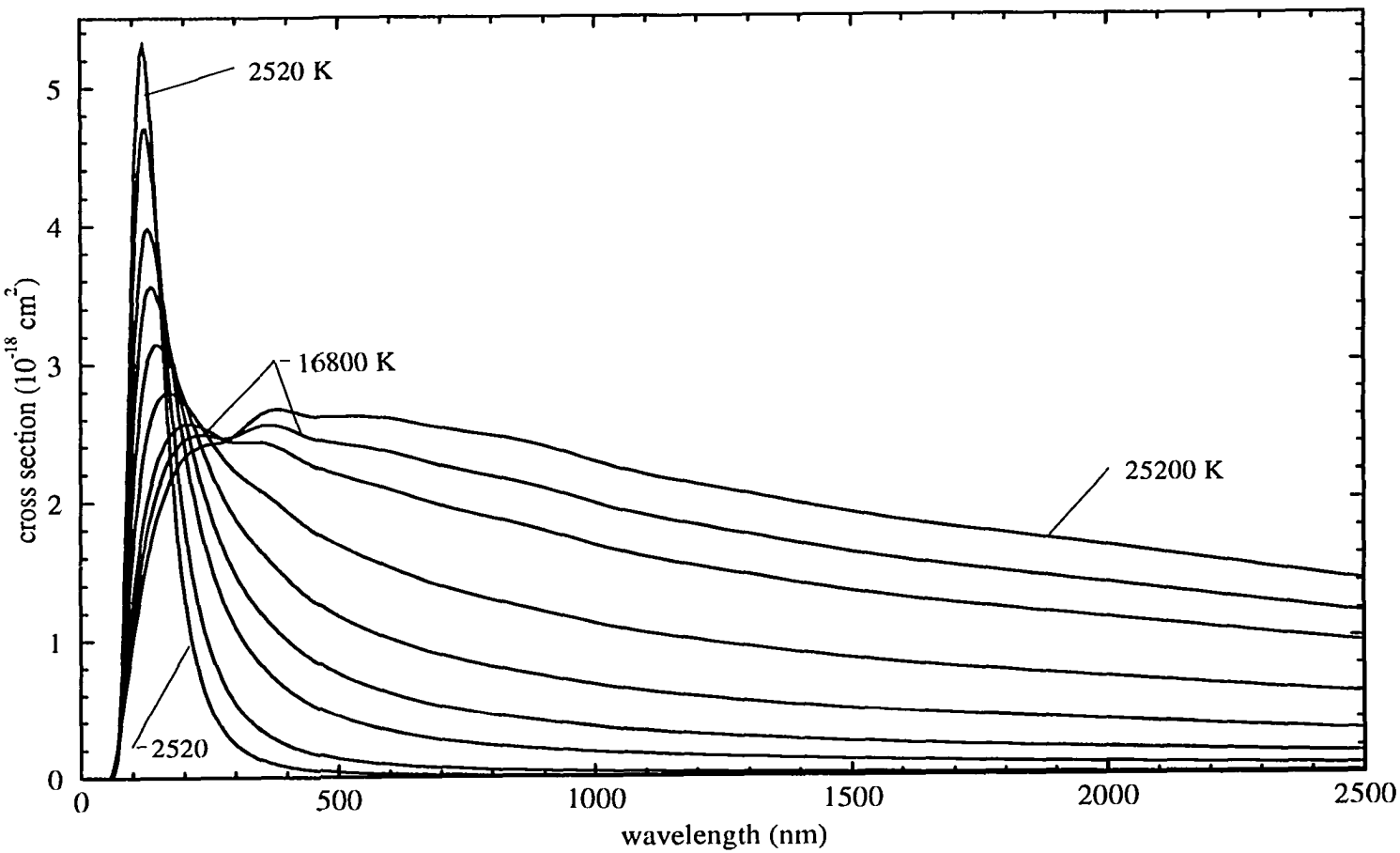

FIG. 3.2-3. Total H_2^+ photodissociation cross sections for T = 2520, 3150, 4200, 5040, 6300, 8400, 12 600, 16 800, and 25 200 K from bottom to top at λ = 500 nm.

TABLE 3.2-1. Photodissociation cross sections $\sigma(10^{-18}\ \mathrm{cm}^2)$ for reaction (3.2-1), $He_2^+ + h\nu \rightarrow He^+ + He$.

λ	T (K)							
(nm)	4200	6300	8400	12600	16800	25200	33600	50400
50	5.99-6[a]	1.15-5	1.50-5	1.86-5	2.62-5	2.18-5	2.25-5	2.31-5
60	4.31-2	8.49-3	0.0112	0.0140	0.0153	0.0165	0.0171	0.0176
70	0.0523	0.0816	0.0973	0.1108	0.1166	0.1213	0.1232	0.1249
80	0.2503	0.2883	0.2956	0.2927	0.2876	0.2809	0.2770	0.2729
90	0.6587	0.6169	0.5716	0.5169	0.4869	0.4584	0.4446	0.4313
100	1.2197	1.0054	0.8757	0.7493	0.6879	0.6333	0.6081	0.5842
110	1.7949	1.3801	1.1630	0.9667	0.8758	0.7973	0.7617	0.7285
120	2.2739	1.6955	1.4083	1.1557	1.0409	0.9426	0.8984	0.8573
130	2.5948	1.9282	1.5999	1.3121	1.1816	1.0701	1.0200	0.9734
140	2.7699	2.0876	1.7438	1.4385	1.2986	1.1784	1.1241	1.0735
150	2.8293	2.1868	1.8478	1.5389	1.3950	1.2699	1.2129	1.1596
160	2.7978	2.2354	1.9185	1.6198	1.4775	1.3523	1.2948	1.2407
170	2.7012	2.2420	1.9582	1.6787	1.5418	1.4194	1.3625	1.3087
180	2.5652	2.2185	1.9747	1.7208	1.5924	1.4754	1.4203	1.3678
190	2.4108	2.1766	1.9764	1.7532	1.6360	1.5269	1.4750	1.4250
200	2.2515	2.1226	1.9663	1.7752	1.6702	1.5701	1.5217	1.4748
210	2.0956	2.0615	1.9468	1.7873	1.6944	1.6034	1.5586	1.5146
220	1.9478	1.9976	1.9221	1.7934	1.7127	1.6310	1.5899	1.5492
230	1.8099	1.9334	1.8946	1.7958	1.7275	1.6553	1.6182	1.5809
240	1.6822	1.8694	1.8646	1.7945	1.7382	1.6756	1.6425	1.6087
250	1.5643	1.8060	1.8322	1.7894	1.7449	1.6919	1.6628	1.6326
260	1.4557	1.7438	1.7985	1.7817	1.7488	1.7054	1.6805	1.6541
270	1.3561	1.6834	1.7641	1.7720	1.7506	1.7168	1.6962	1.6736
280	1.2648	1.6249	1.7291	1.7601	1.7497	1.7253	1.7088	1.6901
290	1.1815	1.5685	1.6935	1.7458	1.7457	1.7302	1.7177	1.7026
300	1.1056	1.5144	1.6579	1.7297	1.7391	1.7320	1.7234	1.7119
350	0.8192	1.2864	1.4950	1.6420	1.6905	1.7188	1.7266	1.7304
400	0.6390	1.1210	1.3675	1.5665	1.6448	1.7017	1.7233	1.7406
450	0.5156	0.9900	1.2562	1.4893	1.5890	1.6678	1.7003	1.7283
500	0.4267	0.8818	1.1552	1.4080	1.5221	1.6161	1.6566	1.6927
600	0.3145	0.7275	1.0010	1.2736	1.4051	1.5195	1.5711	1.6187
700	0.2506	0.6309	0.9016	1.1870	1.3314	1.4619	1.5226	1.5799
800	0.2079	0.5578	0.8202	1.1078	1.2583	1.3977	1.4638	1.5271
900	0.1772	0.4991	0.7498	1.0327	1.1842	1.3269	1.3955	1.4618
1000	0.1551	0.4541	0.6941	0.9710	1.1219	1.2660	1.3360	1.4041
2000	0.0716	0.2458	0.4036	0.6028	0.7194	0.8366	0.8958	0.9549
3000	0.0454	0.1634	0.2743	0.4207	0.5041	0.5919	0.6368	0.6820
4000	0.0344	0.1268	0.2151	0.3334	0.4015	0.4738	0.5110	0.5486
5000	0.0290	0.1088	0.1861	0.2908	0.3516	0.4165	0.4501	0.4841
11000	0.0134	0.0517	0.0900	0.1429	0.1742	0.2080	0.2257	0.2437
15000	0.0104	0.0408	0.0711	0.1134	0.1384	0.1656	0.1798	0.1943
20000	8.88-3	0.0349	0.0611	0.0976	0.1194	0.1430	0.1554	0.1681

[a]The notation 5.99-6 corresponds to 5.99×10^{-6}.

Reproduced with permission of the copyright owner. Further reproduction prohibited without permission.

TABLE 3.2-2. Photodissociation cross sections σ (10^{-18} cm^2) for reaction (3.2-2), $H_2^+ + h\nu \rightarrow H^+ + H$.

λ	T (K)							
(nm)	3150	4200	5040	6300	8400	12600	16800	25200
50	7.34-5	1.43-4	2.04-4	2.87-4	3.89-4	4.97-4	5.49-4	5.98-4
60	0.0100	0.0150	0.0186	0.0230	0.0276	0.0319	0.0337	0.0353
70	0.1676	0.1965	0.2105	0.2215	0.2266	0.2246	0.2211	0.2163
80	0.8477	0.8199	0.7797	0.7183	0.6376	0.5477	0.5037	0.4622
90	2.1113	1.8166	1.6135	1.3823	1.1403	0.9157	0.8176	0.7313
100	3.4427	2.8069	2.4213	2.0136	1.6137	1.2616	1.1129	0.9845
110	4.3470	3.5155	3.0224	2.5070	2.0062	1.5685	1.3846	1.2262
120	4.6981	3.8841	3.3806	2.8402	2.3019	1.8203	1.6147	1.4358
130	4.6169	3.9763	3.5361	3.0358	2.5120	2.0239	1.8096	1.6202
140	4.2811	3.8840	3.5476	3.1272	2.6535	2.1858	1.9729	1.7809
150	3.8331	3.6850	3.4660	3.1434	2.7388	2.3082	2.1033	1.9138
160	3.3624	3.4344	3.3301	3.1098	2.7840	2.4020	2.2106	2.0287
170	2.9167	3.1670	3.1662	3.0438	2.7985	2.4707	2.2958	2.1244
180	2.5172	2.9031	2.9909	2.9573	2.7898	2.5175	2.3610	2.2019
190	2.1697	2.6538	2.8149	2.8600	2.7657	2.5495	2.4128	2.2682
200	1.8726	2.4243	2.6444	2.7573	2.7300	2.5682	2.4516	2.3222
210	1.6208	2.2160	2.4821	2.6522	2.6843	2.5725	2.4748	2.3597
220	1.4085	2.0289	2.3297	2.5473	2.6314	2.5653	2.4852	2.3839
230	1.2295	1.8617	2.1883	2.4453	2.5755	2.5517	2.4889	2.4012
240	1.0785	1.7129	2.0581	2.3479	2.5188	2.5347	2.4885	2.4144
250	0.9508	1.5804	1.9387	2.2553	2.4622	2.5145	2.4840	2.4230
260	0.8424	1.4623	1.8293	2.1680	2.4063	2.4920	2.4762	2.4277
270	0.7501	1.3568	1.7296	2.0865	2.3530	2.4701	2.4687	2.4327
280	0.6712	1.2626	1.6392	2.0118	2.3045	2.4525	2.4660	2.4433
290	0.6033	1.1783	1.5577	1.9443	2.2620	2.4415	2.4707	2.4626
300	0.5448	1.1029	1.4843	1.8834	2.2256	2.4369	2.4825	2.4901
350	0.3477	0.8233	1.2037	1.6442	2.0832	2.4343	2.5567	2.6400
400	0.2412	0.6469	1.0069	1.4533	1.9363	2.3659	2.5349	2.6658
450	0.1782	0.5283	0.8605	1.2951	1.7920	2.2630	2.4604	2.6222
500	0.1389	0.4487	0.7547	1.1780	1.6859	2.1963	2.4228	2.6179
600	0.0927	0.3396	0.6120	1.0109	1.5255	2.0874	2.3564	2.6031
700	0.0685	0.2749	0.5175	0.8894	1.3923	1.9700	2.2587	2.5323
800	0.0542	0.2335	0.4534	0.8033	1.2940	1.8800	2.1824	2.4760
900	0.0448	0.2041	0.4046	0.7334	1.2067	1.7876	2.0941	2.3965
1000	0.0382	0.1813	0.3635	0.6701	1.1194	1.6816	1.9827	2.2828
2000	0.0159	0.0901	0.1982	0.3951	0.7108	1.1448	1.3953	1.6590
3000	0.0100	0.0596	0.1325	0.2699	0.4954	0.8132	1.0003	1.1999
4500	6.88-3	0.0425	0.0962	0.1994	0.3723	0.6216	0.7710	0.9325
5000	6.41-3	0.0400	0.0908	0.1889	0.3540	0.5932	0.7371	0.8932
10000	3.56-3	0.0229	0.0526	0.1110	0.2109	0.3582	0.4479	0.5463
15000	2.50-3	0.0161	0.0373	0.0790	0.1506	0.2567	0.3216	0.3929
20000	1.90-3	0.0123	0.0286	0.0607	0.1161	0.1982	0.2487	0.3042

Reproduced with permission of the copyright owner. Further reproduction prohibited without permission.

levels up to $v'' = 7$ with $N'' = 0$, 4, and 8. Our calculation agrees to within 20% since the high-lying states are unimportant at this temperature.

The photodissociation absorption coefficients for processes (3.2-1) and (3.2-2) can be obtained from the data in Tables 3.2-1 and 3.2-2 for He_2^+ and H_2^+, respectively. In addition, the free-free absorption coefficients are given in Tables 3.2-3 and 3.2-4 for reactions (3.2-3) and (3.2-4). The free-free coefficients were calculated using the method of Bates [136] (see his Eqs. (12) and (18)), who in the now classic semiclassical calculation investigated jointly the free-free process (3.2-4) with the photodissociation (or bound-free) process of reaction (3.2-2). Recently, Mihajlov & Dimitrijević ([137] hereafter MD1; [138] MD2), within a less accurate semiclassical formalism studied the combination of reactions (3.2-2) and (3.2-4) as well as process (3.2-1) and (3.2-3). MD1 and MD2 assumed the transition occurs near the resonant internuclear distance and approximated the dipole matrix element. Fortunately, both authors provide a means to extract the bound-free processes from the total. Note that Bates's [136] coefficients include LTE stimulated emission while this work and that of MD1 and MD2 do not.

The He_2^+ photodissociation results of MD2 agree with our absorption coefficients for intermediate wavelengths and low temperatures to within a few percent, but for $T \geq 8000$ K and/or $\lambda \geq 1000$ nm their coefficients deviate significantly and have the wrong long-wavelength behavior of increasing with wavelength. We give new results for $T < 30,000$ K with $50 \leq \lambda \leq 200$ nm and $2 \leq \lambda \leq 20$ μm. We also present additional coefficients for 33,600 K and 50,400 K.

Our H_2^+ bound-free coefficients agree with Bates [136] to within a few percent for the wavelength range $385 \leq \lambda \leq 20,000$ nm and temperature range $2500 \leq T \leq 12,000$ K previously investigated. We also agree well with the Buckingham et al. [135] results for $\lambda \leq 455$ nm at 2500 K. We extend the available coefficients to $\lambda = 50$ nm and $T = 25,200$ K. The work of MD1 and MD2 deviate in a manner similar

Reproduced with permission of the copyright owner. Further reproduction prohibited without permission.

TABLE 3.2-3. Free-free absorption coefficients a (10^{-39} cm^5) for reaction (3.2-3), $He^+ + He + h\nu \rightarrow He^+ + He$.

λ	T (K)							
(nm)	4200	6300	8400	12600	16800	25200	33600	50400
70	7.08-3	6.05-3	5.45-3	4.78-3	4.41-3	3.99-3	3.75-3	3.50-3
80	0.0103	8.76-3	7.84-3	6.79-3	6.20-3	5.52-3	5.15-3	4.74-3
90	0.0134	0.0113	0.0101	8.66-3	7.87-3	6.97-3	6.48-3	5.91-3
100	0.0165	0.0139	0.0124	0.0106	9.65-3	8.52-3	7.89-3	7.19-3
110	0.0196	0.0165	0.0147	0.0126	0.0114	0.0101	9.30-3	8.47-3
120	0.0226	0.0190	0.0169	0.0145	0.0131	0.0116	0.0107	9.72-3
130	0.0259	0.0217	0.0193	0.0166	0.0150	0.0132	0.0122	0.0111
140	0.0288	0.0242	0.0215	0.0185	0.0167	0.0147	0.0136	0.0124
150	0.0317	0.0267	0.0237	0.0204	0.0185	0.0163	0.0151	0.0137
160	0.0347	0.0292	0.0260	0.0223	0.0203	0.0179	0.0165	0.0151
170	0.0377	0.0317	0.0283	0.0243	0.0220	0.0195	0.0180	0.0164
180	0.0405	0.0341	0.0304	0.0262	0.0237	0.0210	0.0195	0.0178
190	0.0433	0.0365	0.0326	0.0280	0.0254	0.0225	0.0209	0.0191
200	0.0460	0.0388	0.0346	0.0298	0.0271	0.0240	0.0223	0.0204
210	0.0487	0.0411	0.0367	0.0316	0.0288	0.0255	0.0237	0.0217
220	0.0514	0.0434	0.0387	0.0335	0.0304	0.0270	0.0251	0.0230
230	0.0540	0.0457	0.0408	0.0352	0.0321	0.0285	0.0266	0.0244
240	0.0567	0.0479	0.0429	0.0371	0.0338	0.0301	0.0280	0.0257
250	0.0593	0.0502	0.0449	0.0389	0.0354	0.0316	0.0294	0.0271
260	0.0619	0.0524	0.0469	0.0407	0.0371	0.0331	0.0308	0.0284
270	0.0645	0.0546	0.0489	0.0424	0.0387	0.0346	0.0323	0.0297
280	0.0669	0.0567	0.0508	0.0441	0.0403	0.0360	0.0336	0.0310
290	0.0693	0.0587	0.0527	0.0457	0.0418	0.0374	0.0350	0.0323
300	0.0716	0.0607	0.0545	0.0474	0.0433	0.0388	0.0363	0.0335
350	0.0825	0.0702	0.0632	0.0551	0.0506	0.0455	0.0427	0.0396
400	0.0934	0.0798	0.0719	0.0630	0.0580	0.0524	0.0494	0.0460
450	0.1036	0.0887	0.0802	0.0706	0.0651	0.0591	0.0558	0.0522
500	0.1122	0.0964	0.0873	0.0771	0.0714	0.0650	0.0615	0.0577
600	0.1280	0.1106	0.1006	0.0894	0.0831	0.0762	0.0724	0.0683
700	0.1446	0.1255	0.1146	0.1024	0.0956	0.0882	0.0841	0.0797
800	0.1573	0.1371	0.1257	0.1129	0.1058	0.0980	0.0938	0.0892
900	0.1673	0.1465	0.1347	0.1215	0.1143	0.1063	0.1020	0.0973
1000	0.1787	0.1570	0.1448	0.1312	0.1237	0.1155	0.1111	0.1064
2000	0.2615	0.2361	0.2221	0.2067	0.1984	0.1894	0.1847	0.1796
3000	0.3078	0.2825	0.2687	0.2537	0.2456	0.2371	0.2325	0.2278
4000	0.3556	0.3301	0.3162	0.3014	0.2934	0.2850	0.2806	0.2760
5000	0.4175	0.3909	0.3766	0.3612	0.3531	0.3445	0.3400	0.3353
11000	0.5835	0.5607	0.5487	0.5360	0.5294	0.5225	0.5190	0.5153
15000	0.6620	0.6406	0.6293	0.6176	0.6114	0.6051	0.6018	0.5985
20000	0.7563	0.7359	0.7252	0.7140	0.7083	0.7023	0.6992	0.6961

Reproduced with permission of the copyright owner. Further reproduction prohibited without permission.

TABLE 3.2-4. Free-free absorption coefficients a (10^{-39} cm^5) for reaction (3.2-4), $H^+ + H + h\nu \rightarrow H^+ + H$.

λ	T (K)							
(nm)	3150	4200	5040	6300	8400	12600	16800	25200
70	0.0174	0.0154	0.0142	0.0130	0.0116	0.0100	9.10-3	8.08-3
80	0.0280	0.0246	0.0227	0.0207	0.0184	0.0158	0.0143	0.0126
90	0.0394	0.0346	0.0319	0.0290	0.0257	0.0220	0.0199	0.0175
100	0.0514	0.0451	0.0416	0.0378	0.0336	0.0287	0.0259	0.0227
110	0.0640	0.0562	0.0519	0.0471	0.0418	0.0357	0.0322	0.0283
120	0.0770	0.0676	0.0624	0.0567	0.0504	0.0431	0.0389	0.0341
130	0.0903	0.0794	0.0733	0.0666	0.0592	0.0506	0.0457	0.0401
140	0.1040	0.0914	0.0843	0.0767	0.0682	0.0584	0.0527	0.0464
150	0.1177	0.1035	0.0956	0.0869	0.0773	0.0663	0.0599	0.0527
160	0.1317	0.1158	0.1070	0.0973	0.0866	0.0743	0.0672	0.0592
170	0.1456	0.1281	0.1184	0.1078	0.0960	0.0824	0.0746	0.0658
180	0.1597	0.1405	0.1299	0.1183	0.1054	0.0906	0.0821	0.0725
190	0.1737	0.1530	0.1414	0.1288	0.1149	0.0988	0.0896	0.0793
200	0.1877	0.1654	0.1529	0.1394	0.1243	0.1071	0.0972	0.0861
210	0.2017	0.1777	0.1644	0.1499	0.1338	0.1154	0.1048	0.0930
220	0.2156	0.1901	0.1759	0.1605	0.1433	0.1237	0.1125	0.0998
230	0.2294	0.2023	0.1873	0.1709	0.1527	0.1319	0.1201	0.1068
240	0.2431	0.2145	0.1987	0.1814	0.1622	0.1402	0.1277	0.1137
250	0.2568	0.2266	0.2099	0.1917	0.1716	0.1485	0.1354	0.1206
260	0.2703	0.2387	0.2211	0.2020	0.1809	0.1567	0.1430	0.1276
270	0.2836	0.2506	0.2322	0.2123	0.1902	0.1649	0.1506	0.1345
280	0.2969	0.2624	0.2433	0.2225	0.1994	0.1731	0.1582	0.1414
290	0.3100	0.2741	0.2542	0.2325	0.2086	0.1812	0.1657	0.1483
295	0.3165	0.2799	0.2596	0.2376	0.2131	0.1853	0.1695	0.1518
300	0.3230	0.2857	0.2650	0.2425	0.2177	0.1893	0.1732	0.1552
350	0.3858	0.3419	0.3176	0.2913	0.2621	0.2290	0.2103	0.1894
400	0.4451	0.3952	0.3677	0.3378	0.3048	0.2674	0.2463	0.2228
450	0.5011	0.4457	0.4152	0.3821	0.3456	0.3044	0.2812	0.2555
500	0.5539	0.4935	0.4603	0.4243	0.3848	0.3401	0.3150	0.2873
600	0.6511	0.5821	0.5442	0.5032	0.4583	0.4078	0.3795	0.3484
700	0.7388	0.6625	0.6207	0.5756	0.5262	0.4710	0.4402	0.4064
800	0.8186	0.7362	0.6911	0.6425	0.5895	0.5303	0.4975	0.4615
900	0.8918	0.8042	0.7563	0.7049	0.6488	0.5864	0.5518	0.5141
1000	0.9596	0.8675	0.8173	0.7633	0.7047	0.6395	0.6036	0.5644
2000	1.4600	1.3450	1.2830	1.2170	1.1460	1.0680	1.0260	0.9815
3000	1.8050	1.6820	1.6170	1.5470	1.4740	1.3940	1.3510	1.3060
4500	2.2000	2.0750	2.0090	1.9390	1.8650	1.7860	1.7450	1.7000
5000	2.3130	2.1880	2.1220	2.0520	1.9790	1.9010	1.8590	1.8160
10000	3.1800	3.0620	3.0000	2.9360	2.8690	2.7980	2.7610	2.7230
15000	3.8110	3.7000	3.6420	3.5820	3.5200	3.4560	3.4220	3.3870
20000	4.3230	4.2180	4.1640	4.1080	4.0500	3.9900	3.9580	3.9260

Reproduced with permission of the copyright owner. Further reproduction prohibited without permission.

to that found for their He_2^+ values, as discussed above, and are typically a factor of two too small. Though they used the same potentials as Bates, the approximation of a classical transition is less accurate at large R resulting in the long wavelength deviation.

Argyros [132] extended Bates's [136] semiclassical formalism to shorter wavelengths and found significant discrepancies for $T > 5000$ K and $\lambda < 2000$ nm with his quantum mechanical results. In contrast, we find excellent agreement between the quantum and semiclassical methods at all temperatures with $\lambda > 90$ and 70 nm for H_2^+ and He_2^+, respectively, except for H_2^+ at high temperatures. For example, the semiclassical coefficients at 25,200 K are $\sim 20\%$ too large in the range $100 < \lambda < 5000$ nm. Figs. 3.2-4 and 3.2-5 compare the quantum mechanical and semiclassical photodissociation absorption coefficients for He_2^+ and H_2^+, respectively.

Figs. 3.2-6 and 3.2-7 display the total semiclassical absorption coefficients for He_2^+ and H_2^+ including stimulated emission with comparison to the results of MD2 in Fig. 3.2-6 and to Bates [136], Buckingham et al. [135], and MD2 in Fig. 3.2-7. The results of MD1 and MD2 were corrected for stimulated emission. For H_2^+, our results, Buckingham et al., and Bates agree. The slight differences between our work and that of Bates can probably be attributed to round-off error in the earlier calculation. The results of MD1 and MD2 are again consistently lower than Bates's and our absorption coefficients, but contrary to their photodissociation values, their total absorption coefficients display the correct long-wavelength behavior. This can be attributed to the dominance of stimulated emission at long wavelengths. Similar considerations apply for He_2^+ shown in Fig. 3.2-6.

Reproduced with permission of the copyright owner. Further reproduction prohibited without permission.

Reproduced with permission of the copyright owner. Further reproduction prohibited without permission.

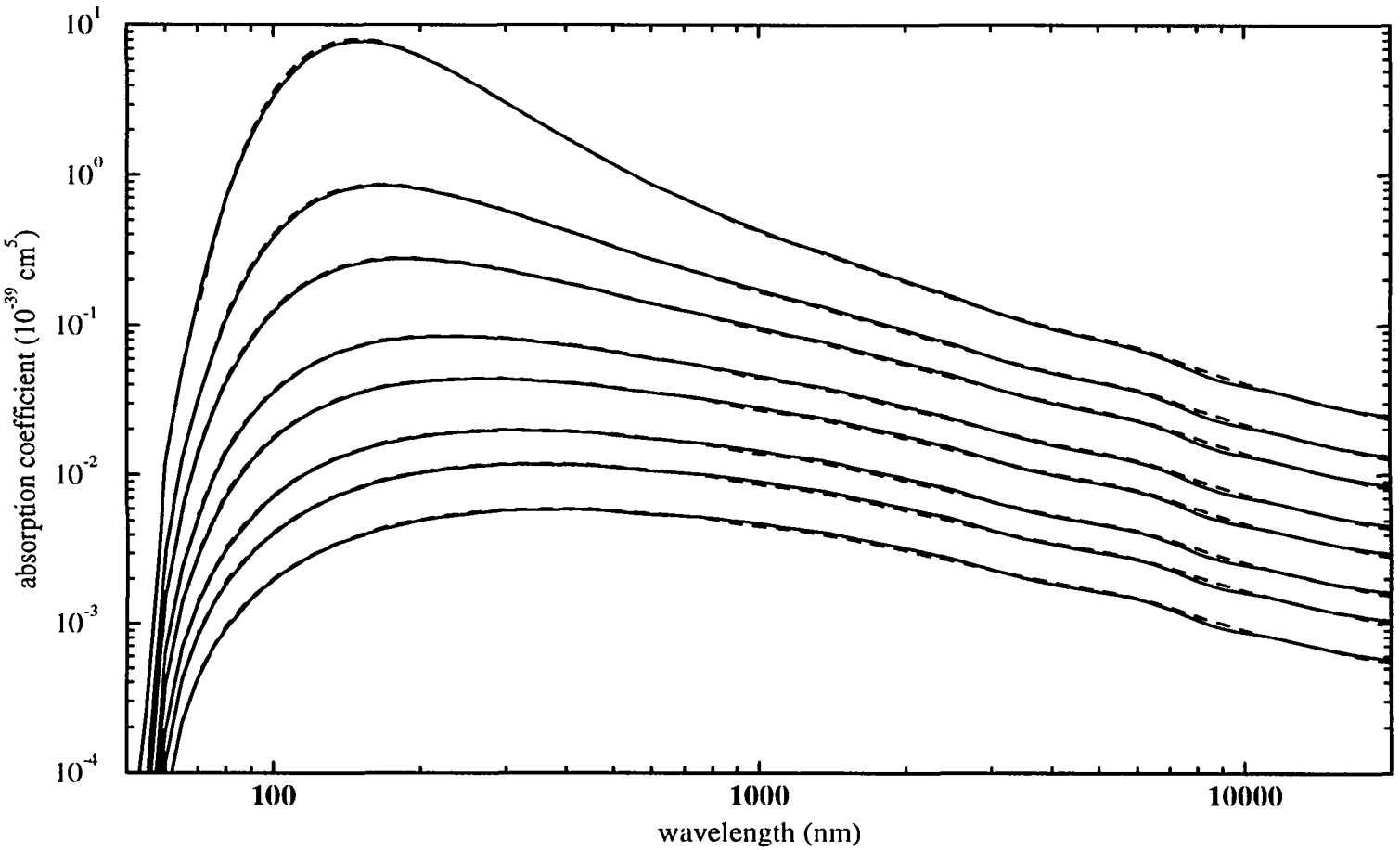

FIG. 3.2-4. Comparison of quantum mechanical (full lines) and semiclassical (dashed lines) photodissociation absorption coefficients for He_2^+ for T = 4200, 6300, 8400, 12 600, 16 800, 25 200, 33 6000, and 50 400 K from top to bottom.

Reproduced with permission of the copyright owner. Further reproduction prohibited without permission.

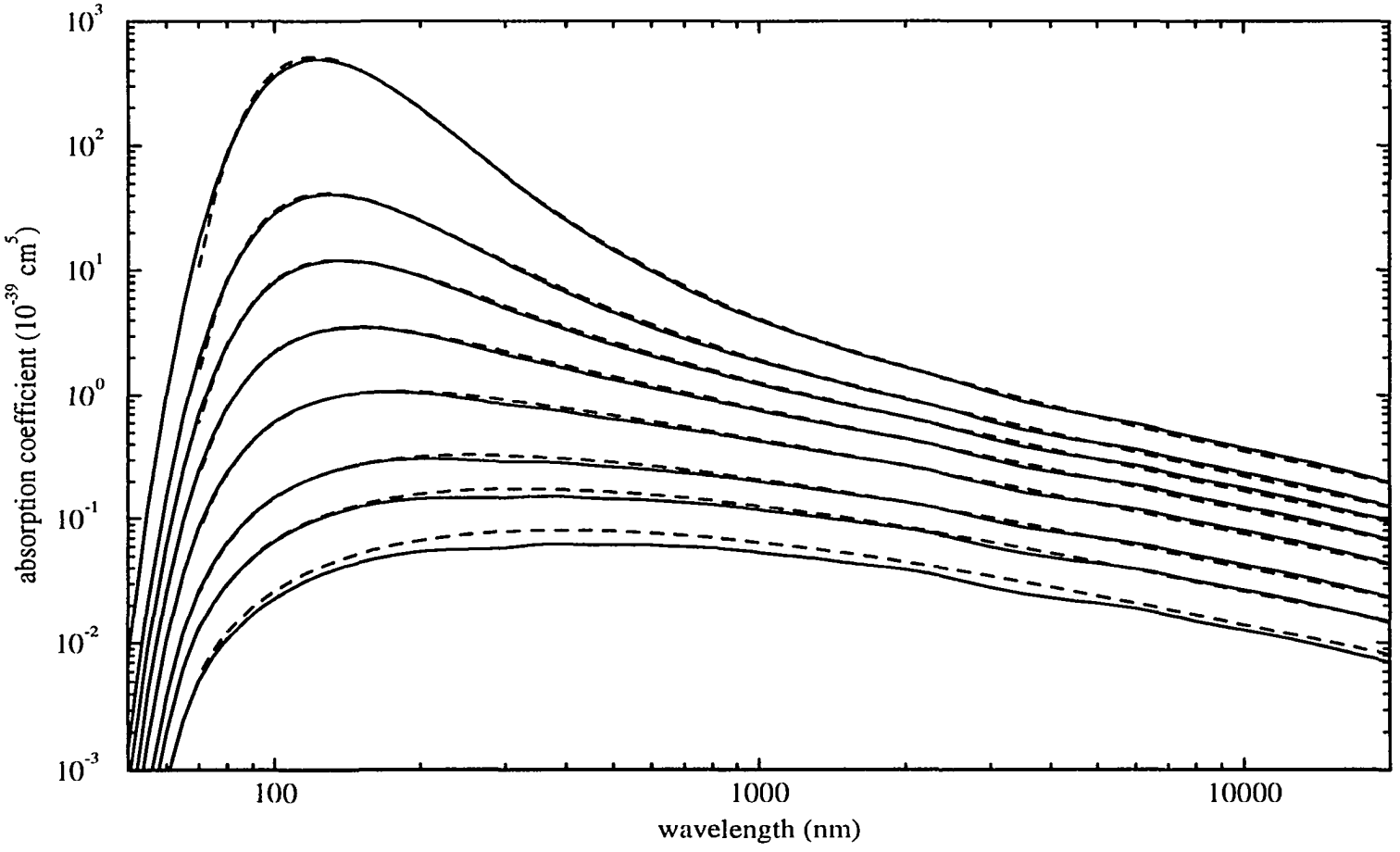

FIG. 3.2-5. Comparison of quantum mechanical (full lines) and semiclassical (dashed lines) photodissociation absorption coefficients for H_2^+ for T = 3150, 4200, 5040, 6300, 8400, 12 600, 16 800, and 25 2000 K from top to bottom.

Reproduced with permission of the copyright owner. Further reproduction prohibited without permission.

FIG. 3.2-6. Total He_2^+ absorption coefficients. This work is given by the full lines for T = 3000, 4000, 6000, 8000, 10 000, 15 000, 20 000, 25 000, 30 000, and 50 000 K from top to bottom. The results of Mihajlov and Dimitrijevic are given by the dashed lines.

Reproduced with permission of the copyright owner. Further reproduction prohibited without permission.

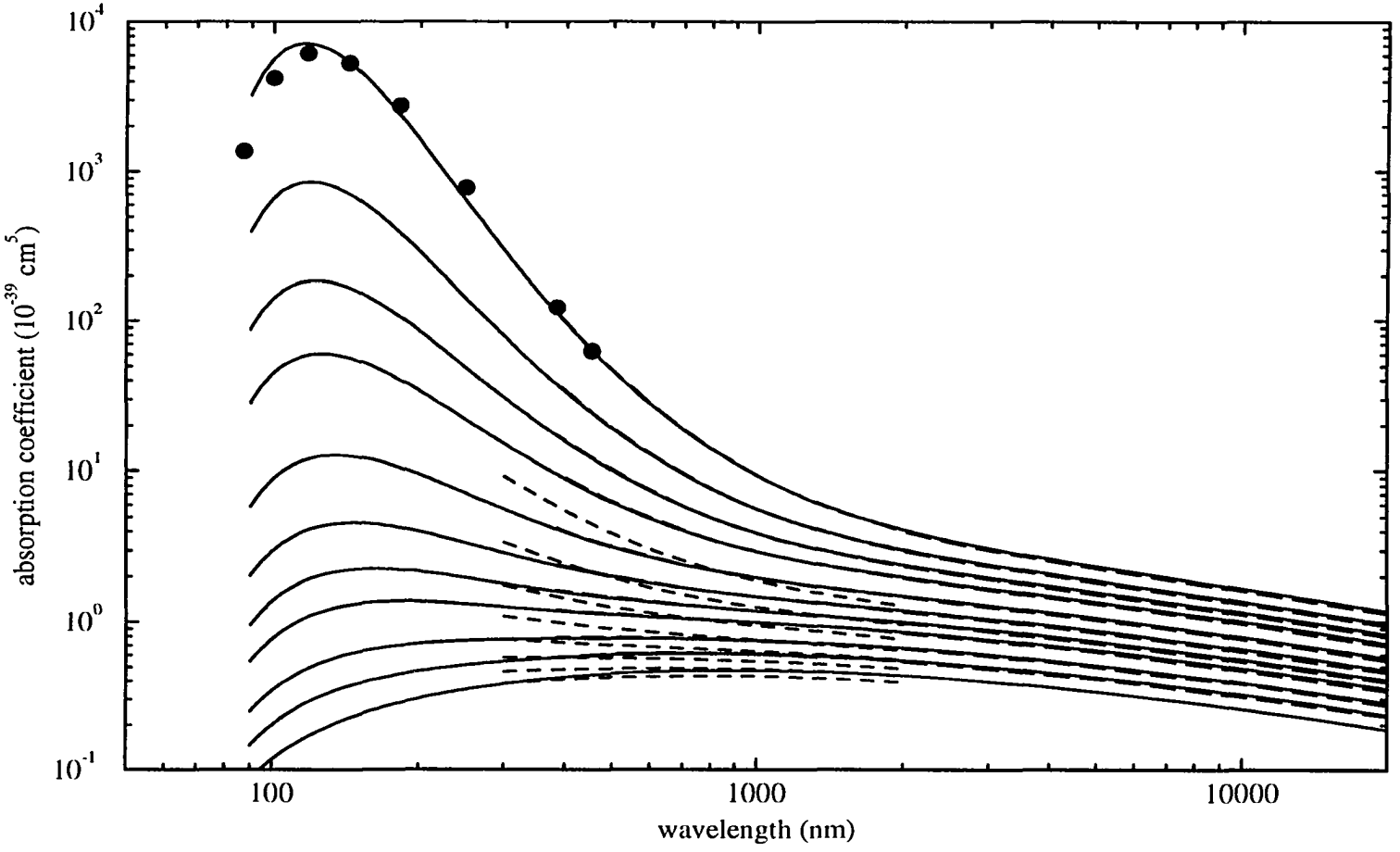

FIG. 3.2-7. Total H_2^+ absorption coefficients. This work is given by the full lines for T = 2500, 3000, 3500, 4000, 5000, 6000, 7000, 8000, 10 000, 12 000, and 15 000 K from top to bottom. The results of Bates are given by the long dashed lines except for T = 15 000 K, Mihajlov and Dimitrijevic by the short dashed lines for T = 4000 (1000) 11 000 K, and Buckingham et al. by the filled circles for T = 2500 K.

3.3. Partition Functions and Dissociation Equilibrium Constants for H_2^+ and He_2^+

During the course of the work in Sec. 3.2, discrepancies between the molecular partition functions obtained quantum-mechanically and the polynomial expansions of Sauval and Tatum [139] were found. Sauval and Tatum [139] give tabulations for 300 diatomic molecules and though we agree with their premise that a standard set of molecular equilibrium constants should be used for all model atmosphere calculations to prevent differences in molecular data from obscuring improvements in astrophysical insight, it becomes important for cases where only a small number of elements are considered, to use the most accurate values available. Such situations occur in white dwarfs where only H, He, C, and O are typically considered. Accurate constants are particularly important when attempting to match model fluxes to observations and in the determination of absorption coefficients. Thus we give a new tabulation of partition functions and equilibrium constants for H_2^+ and He_2^+. Published results appear in Ref. [140].

3.3.1. Theory and Calculations

The molecular partition function $Q_{X_2^+}(T)$ is given by Eq. (3.2-7) while the dissociation equilibrium constant in terms of partial pressures is given by

$$
\begin{aligned}
{}^{p}K(T) &= \frac{p(\mathrm{x})p(\mathrm{x}^+)}{p(\mathrm{x}_2^+)} \\
&= \left(\frac{2\pi\mu k_\mathrm{b}T}{h^2}\right)^{\frac{3}{2}} k_\mathrm{b}T\frac{Q_\mathrm{X}Q_{\mathrm{X}^+}}{Q_{\mathrm{X}_2^+}}\exp(-D_\mathrm{e}/k_\mathrm{b}T)\ \mathrm{dyne/cm^2} \qquad (3.3\text{-}1)
\end{aligned}
$$

where $p(\mathrm{x})$ is the partial pressure in dyne/cm^2 and the remaining notation follows that from Secs. 3.1 and 3.2. The equilibrium constant in terms of number density is given simply by

Reproduced with permission of the copyright owner. Further reproduction prohibited without permission.

$$^{n}K(T) = \frac{^{p}K(T)}{k_b T} \tag{3.3-2}$$

where $^{n}K(T)$ is given in Eq. (3.2-12).

To obtain the energies of the RV states, we numerically solve the radial nuclear Schrödinger equation [110,111] using nonrelativistic Born-Oppenheimer potentials for the ground states $X\ ^2\Sigma_g^+$ and $X\ ^2\Sigma_u^+$ of H_2^+ and He_2^+, respectively. The potentials used are discussed in Sec. 3.1.2. We find all 423 RV levels of H_2^+ given in Table 3.1-2 and the tabulation of Hunter, Yau, and Pritchard [141] to which our energies agree to within 10 cm^{-1}. For the He_2^+ ground state, all 411 levels were included as in Table 3.1-2. Dissociation energies and reduced masses are as given in Huber and Herzberg [142]. The atomic partition functions were taken from Irwin [133].

3.3.2. Results and Discussion

Tables 3.3-1 and 3.3-2 display the molecular partition functions and dissociation equilibrium constants for H_2^+ and He_2^+, respectively. The results are extended beyond the temperature range 1000 to 9000 K previously given in Ref. [139]. In addition, some results are given for convenient values of θ where $\theta = 5040/T$. Our results differ for both Q and ^{p}K by 43% and 19% for H_2^+ and He_2^+, respectively, at 9000 K. This discrepancy can be attributed to the approximation

$$Q_{\text{rot}} = \frac{k_b T}{hcB_v} \tag{3.3-3}$$

used by Sauval and Tatum [139] (see for example Tatum [143] and Herzberg [108]). Q_{rot} is the rotational portion of the partition function assuming a separation of electronic, vibrational, and rotational motions and B_v is the rotational constant. Eq. 3.3-3 can only be used when B_v is small, say ~ 2 cm^{-1} as is found for heavy molecules, but $B_v = 30.2$ and 7.2 cm^{-1} for H_2^+ and He_2^+, respectively. This brings into question the accuracy of all the H-containing molecular constants in Ref. [139] especially H_2 which has $B_v = 60.8$ cm^{-1}.

Reproduced with permission of the copyright owner. Further reproduction prohibited without permission.

TABLE 3.3-1. Partition functions and dissociation equilibrium constants for H_2^+.

T(K)	Q	${}^pK$ (dyne/cm^2)	T(K)	Q	${}^pK$ (dyne/cm^2)
1500	4.3648+01	4.6007+01	12500	1.9453+03	1.4292+10
2000	6.6212+01	1.0475+04	12600	1.9682+03	1.4700+10
2500	9.4708+01	2.7724+05	13000	2.0594+03	1.6404+10
2520	9.5983+01	3.0769+05	13500	2.1723+03	1.8701+10
3000	1.3002+02	2.4778+06	14000	2.2838+03	2.1190+10
3150	1.4207+02	4.1753+06	14500	2.3938+03	2.3881+10
3500	1.7299+02	1.1854+07	15000	2.5021+03	2.6781+10
4000	2.2429+02	3.8316+07	15500	2.6087+03	2.9899+10
4200	2.4723+02	5.6644+07	16000	2.7134+03	3.3244+10
4500	2.8427+02	9.5399+07	16500	2.8164+03	3.6825+10
5000	3.5288+02	1.9810+08	16800	2.8773+03	3.9091+10
5040	3.5874+02	2.0874+08	17000	2.9175+03	4.0653+10
5500	4.2977+02	3.6103+08	17500	3.0166+03	4.4737+10
6000	5.1431+02	5.9740+08	18000	3.1139+03	4.9088+10
6300	5.6837+02	7.7934+08	18500	3.2093+03	5.3718+10
6500	6.0570+02	9.1875+08	19000	3.3028+03	5.8637+10
7000	7.0306+02	1.3351+09	19500	3.3944+03	6.3859+10
7500	8.0549+02	1.8551+09	20000	3.4841+03	6.9396+10
8000	9.1210+02	2.4867+09	20500	3.5720+03	7.5261+10
8400	9.9984+02	3.0771+09	21000	3.6581+03	8.1469+10
8500	1.0221+03	3.2369+09	21500	3.7424+03	8.8032+10
9000	1.1346+03	4.1126+09	22000	3.8249+03	9.4967+10
9500	1.2490+03	5.1202+09	22500	3.9057+03	1.0229+11
10000	1.3646+03	6.2660+09	23000	3.9848+03	1.1001+11
10080	1.3832+03	6.4625+09	23500	4.0623+03	1.1816+11
10500	1.4810+03	7.5563+09	24000	4.1382+03	1.2674+11
11000	1.5977+03	8.9975+09	24500	4.2125+03	1.3578+11
11500	1.7141+03	1.0596+10	25000	4.2852+03	1.4530+11
12000	1.8301+03	1.2359+10	25200	4.3138+03	1.4924+11

Reproduced with permission of the copyright owner. Further reproduction prohibited without permission.

TABLE 3.3-2. Partition functions and dissociation equilibrium constants for He_2^+.

T(K)	Q	${}^pK$ (dyne/cm^2)	T(K)	Q	${}^pK$ (dyne/cm^2)
2000	3.0514+02	9.4540+04	35000	2.0106+04	7.6482+11
3000	6.1339+02	1.2563+07	36000	2.0415+04	8.2602+11
4000	1.0601+03	1.4693+08	37000	2.0712+04	8.9007+11
4200	1.1668+03	2.0908+08	38000	2.0999+04	9.5700+11
5000	1.6488+03	6.5088+08	39000	2.1274+04	1.0269+12
5040	1.6751+03	6.8266+08	40000	2.1540+04	1.0997+12
6000	2.3595+03	1.7910+09	41000	2.1796+04	1.1755+12
6300	2.5919+03	2.2902+09	42000	2.2043+04	1.2544+12
7000	3.1604+03	3.7785+09	43000	2.2282+04	1.3364+12
8000	4.0190+03	6.7729+09	44000	2.2512+04	1.4215+12
8400	4.3721+03	8.2817+09	45000	2.2735+04	1.5097+12
9000	4.9074+03	1.0901+10	46000	2.2950+04	1.6012+12
10000	5.8045+03	1.6270+10	47000	2.3158+04	1.6959+12
10080	5.8761+03	1.6756+10	48000	2.3360+04	1.7939+12
11000	6.6945+03	2.2975+10	49000	2.3555+04	1.8953+12
12000	7.5669+03	3.1104+10	50000	2.3744+04	1.9999+12
12600	8.0788+03	3.6700+10	50400	2.3818+04	2.0428+12
13000	8.4146+03	4.0740+10	51000	2.3927+04	2.1080+12
14000	9.2330+03	5.1959+10	52000	2.4105+04	2.2195+12
15000	1.0020+04	6.4836+10	53000	2.4277+04	2.3345+12
16000	1.0774+04	7.9440+10	54000	2.4445+04	2.4530+12
16800	1.1353+04	9.2414+10	55000	2.4607+04	2.5750+12
17000	1.1495+04	9.5841+10	56000	2.4765+04	2.7006+12
18000	1.2184+04	1.1410+11	57000	2.4918+04	2.8297+12
19000	1.2841+04	1.3429+11	58000	2.5067+04	2.9626+12
20000	1.3468+04	1.5646+11	59000	2.5212+04	3.0991+12
21000	1.4065+04	1.8068+11	60000	2.5353+04	3.2393+12
22000	1.4635+04	2.0701+11	61000	2.5490+04	3.3832+12
23000	1.5178+04	2.3549+11	62000	2.5623+04	3.5309+12
24000	1.5697+04	2.6619+11	63000	2.5753+04	3.6825+12
25000	1.6192+04	2.9916+11	64000	2.5880+04	3.8378+12
25200	1.6288+04	3.0603+11	65000	2.6003+04	3.9971+12
26000	1.6665+04	3.3446+11	66000	2.6124+04	4.1602+12
27000	1.7117+04	3.7212+11	67000	2.6241+04	4.3273+12
28000	1.7549+04	4.1222+11	68000	2.6355+04	4.4984+12
29000	1.7962+04	4.5478+11	69000	2.6467+04	4.6734+12
30000	1.8358+04	4.9987+11	70000	2.6576+04	4.8525+12
31000	1.8737+04	5.4753+11	71000	2.6682+04	5.0356+12
32000	1.9101+04	5.9781+11	72000	2.6786+04	5.2229+12
33000	1.9449+04	6.5076+11	73000	2.6888+04	5.4142+12
33600	1.9652+04	6.8382+11	74000	2.6987+04	5.6097+12
34000	1.9784+04	7.0641+11	75000	2.7083+04	5.8094+12

Reproduced with permission of the copyright owner. Further reproduction prohibited without permission.

Finally, our equilibrium constants are dependent upon the atomic partition functions of Irwin [133] who chose an arbitrary binding energy cut-off of 0.1 eV in the partition function sum. The cut-off is actually dependent on the atom's environment [144]. We determined partition functions for H in situations typical of cool hydrogen-rich white dwarfs and found that Irwin's [133] results differed by no greater than 3% (see Sec. 4.2.1). Consequently, we retain the use of atomic partition functions from Ref. [133] to facilitate easy correction of our equilibrium constants by partition functions for particular environments which maybe obtained in the future.

Reproduced with permission of the copyright owner. Further reproduction prohibited without permission.

4. APPLICATIONS TO WHITE DWARFS

White dwarfs are the final evolutionary stage of all low-mass stars. For main-sequence stars the upper limit is approximately $7M_{\odot}$ where $M_{\odot}$ is a solar mass. Stars with larger mass become neutron stars while black holes may result from still more massive objects. Formation of a white dwarf generally occurs near the completion of nuclear burning. The core contracts gravitationally and the outer envelope is lost either by ejection into a thin expanding shell eventually to become a planetary nebula or by accretion to a companion. What remains is a dense, hot, compact core with typically a $0.013R_{\odot}$ ($\sim 10^4$ km) radius, a $0.7M_{\odot}$ mass, and a large surface gravity of log $g = 8$. Because all thermonuclear reactions have ceased, only stored internal heat can be radiated resulting in generally low luminosity. Over the next billion or so years the star cools until it becomes a dark cinder know as a black dwarf.

White dwarfs can be broadly divided into two groups according to their optical spectra. The first, which makes up $\sim$ 80% of the known white dwarfs, have strong hydrogen features and are classified DA. D refers to degenerate, or dwarf, while A indicates a spectrum similar to main-sequence A-type stars which display H I Balmer line absorption. The second group lacks H I lines and may have no features, i.e. a continuous spectrum, or absorption lines of other elements. These stars may be loosely referred to as non-DA. The absorption results from a thin atmosphere with a depth of typically no more than 100 m. DAs are presumed to have hydrogen-dominated atmospheres while non-DAs are usually helium-rich. One must be cautious since this may not always be the case. Lines form in white dwarf spectra for effective stellar temperatures T_{eff} above 5000 K for H I, 13,000 K for He I, and 30,000 K for He II. A star with T_{eff} = 10,000 K will display strong H I Balmer lines if a significant fraction of its atmosphere contains hydrogen. The line identifications, though, are not enough

Reproduced with permission of the copyright owner. Further reproduction prohibited without permission.

to exclude helium as a significant and possibly dominant atmospheric constituent. Nevertheless, the star is classified DA.

A sophisticated classification scheme has been worked out by the white dwarf community and is explained in Sion et al. [145] and Wesemael et al. [146]. Ref. [146] also gives typical spectra of each of the classes. Classifications of the stars investigated in this chapter only will be discussed.

The first letter is always D while the second indicates the primary optical spectroscopic feature. A for H I, B for He I, O for He II, Q for carbon, Z for metals, and C for featureless or continuous. Additional letters may refer to secondary or tertiary spectral features or other properties. Of interest here is P for polarized magnetic, H for a magnetic star lacking polarization, and X for an unclassifiable or peculiar object. Finally a numerical index at the end corresponds to the effective temperature where #=50,400/T_{eff}. For example, the star Feige 7 is classified DBAP3 which indicates a polarized magnetic white dwarf with $T_{eff} \sim$ 17,000 K and a spectrum with strong He I and weak H I features. Two groups of these stars, namely magnetic and cool white dwarfs will be investigated below with the aid of some of the atomic and molecular data given in Chapters 2 and 3.

4.1. Magnetic White Dwarfs

Of the approximately six hundred observable white dwarfs, a small group of 32 are currently known to be highly magnetic. Typically one or two new stars may be discovered or reclassified each year. The field strengths range from a few MG to as high as $\sim$ 700 MG and may vary by a factor of two from the pole to the equator for a centered dipole distribution. A higher surface field variation may result from other field geometries. Their magnetic nature is inferred from broad-band continuum polarization measurements or Zeeman splitting of the H I Balmer lines. The lower limit is an observational effect. Below 1 MG, the Zeeman splitting is unresolvable

Reproduced with permission of the copyright owner. Further reproduction prohibited without permission.

in flux spectra. Recently, the limit has been pushed to below 0.1 MG by measuring high precision circular polarization spectra [147,148]. Polarization reversals appear at Balmer line wavelengths if the star is polarized magnetic. At the upper limit, the field strengths of the stars are generally uncertain, but must be quite large due to significant measured polarization. The uncertainty in the field strength is related to unidentifiable spectral features. The four largest field strength stars are probably GD 229 (WD 2010+310), Grw +70°8247 (WD 1900+705), PG 1031+234 [149], and one component of the newly discovered binary LB 11146 [150]. The spectral features of Grw +70°8247 [151,152,72,46] and PG 1031+234 [153] have only recently been identified as H I classifying them as DAP with field strengths of $\sim$ 320 MG and 200-500 MG, respectively. The identifications are a direct result of the strong field atomic structure calculations of the Tübingen [20,21] and LSU [8,11,12] groups. Conversely, the presence of strong fields in white dwarfs as well as neutron stars has been the main impetus for investigating atomic structure in such extreme conditions. As discussed in Sec. 2.1, the effort applicable to white dwarfs has concentrated on bound H I transitions. The remaining two stars, GD 229 and LB 11146, have features which cannot be reconciled by H I and therefore presumably are He I though little atomic data exist to attempt an interpretation.

4.1.1. Grw +70°8247

The peculiar though now understood spectrum of this famous white dwarf was first observed by Minkowski [154] in 1938. Over the years many explanations have been put forth to account for the unusual features at 413.5 and 583.5 nm including Zeeman-shifted He I and C I lines. As mentioned above, the strong field H I calculations finally resolved the mystery. The field strength (320±20 MG) and effective temperature ($\sim$ 14,000 K) have been further constrained by the synthetic spectra calculation of Wickramasinghe and Ferrario [46] (hereafter WF). WF determined a field-free atmosphere but incorporated the Tübingen and LSU H I calculations into

Reproduced with permission of the copyright owner. Further reproduction prohibited without permission.

line opacities for the radiative transfer calculations. Their synthetic spectra agree well for the wavelength region 300-620 nm, but are poor for 200-300 nm and 620-900 nm. WF also note some discrepancies between the Tübingen and LSU calculations and with the observations. These discrepancies served as the motivation for the new calculations described in Sec. 2.1. Each of these is discussed in turn below.

The $1s \rightarrow 2p_{-1}$ *(Ly*α σ^-*) transition.* Greenstein and Oke [155] obtained UV spectra of this star with the *International Ultraviolet Explorer* (IUE) and observed a fairly sharp absorption peak at 134.7 nm. Greenstein [151] later interpreted the line as H I Lyα σ^- in a field near 350 MG using the early LSU [8] calculations but noted the maximum theoretical wavelength was 133.5 nm. A more detailed computation by Henry and O'Connell [11] found a maximum wavelength of 134.26 nm but at 560 MG. Various calculations of the wavelength for the transition versus field strength are given in Figure 2.1-1. Inclusion of gravitational and Stark-induced redshifts may increase the wavelength by no more than 0.1 nm. Greenstein, Henry, and O'Connell [152] suggest the 0.4 nm shift may be due to observational error. Finally, the synthetic spectra of WF, which match the observed line positions and widths in the visible for $B = 320$ MG, predict a line core at 132.5 nm, increasing the discrepancy to 2 nm, and a line strength an order of magnitude larger than observed. The synthetic spectra of WF and the observed spectrum are shown in Figure 4.1-1. The synthetic line position and depth persist regardless of reasonable field strength, magnetic axis viewing orientation, and effective temperature variation. WF note their use of a field-free atmosphere may have caused deviations at low optical depths but this is unlikely to account for the 2 nm difference. In addition, they suggest the 134.7 nm observation may not be Lyα σ^-.

The energies determined from the nonrelativistic infinite proton mass Hamiltonian of Eq. (2.1-1) with the mixed Slater-Landau basis functions of Eq. (2.1-2) give Lyα σ^- transitions wavelengths that agree (after correcting for the finite proton mass) with

Reproduced with permission of the copyright owner. Further reproduction prohibited without permission.

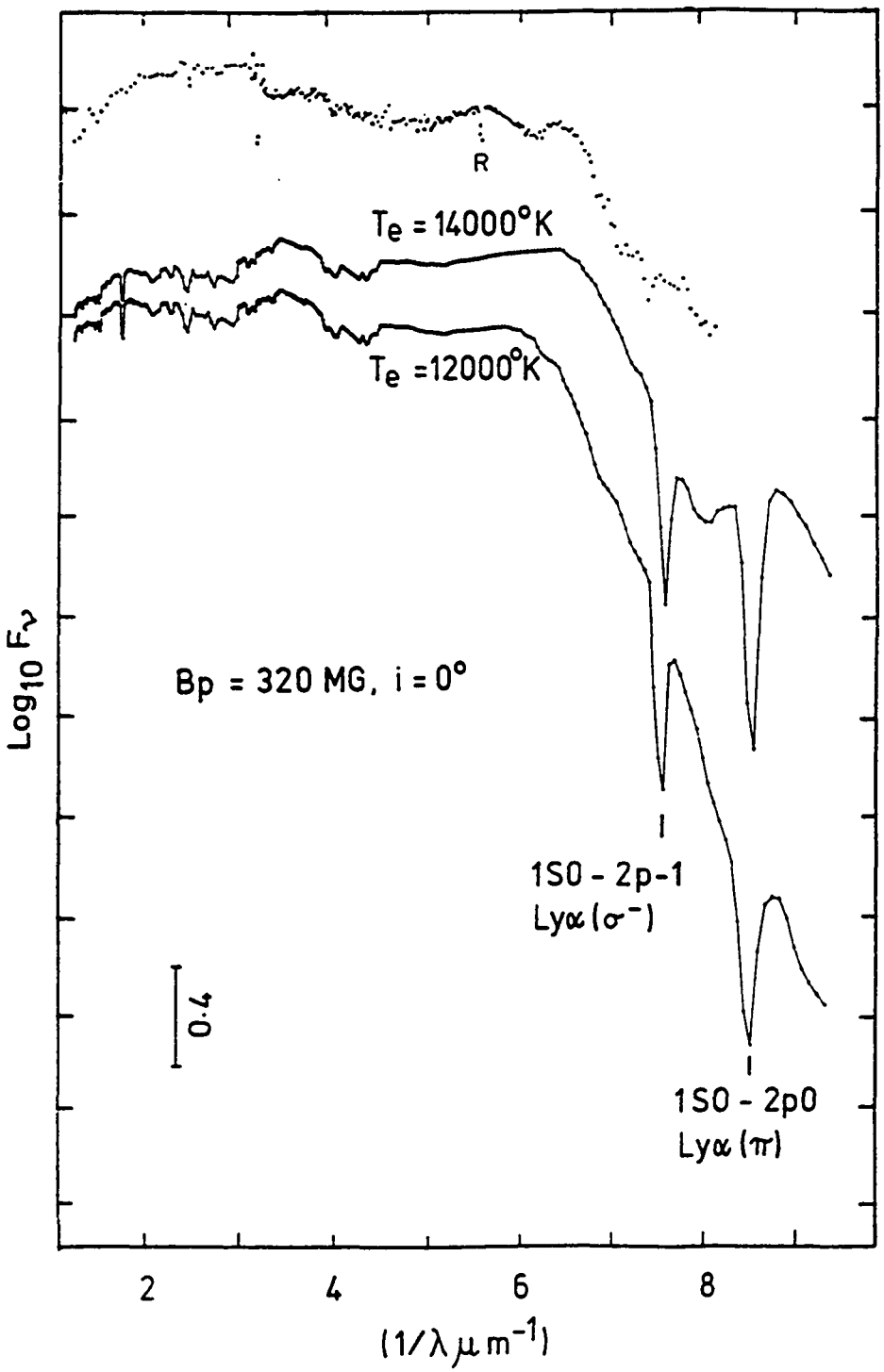

FIG. 4.1-1. Observed and modeled spectra of Grw +70°8247 from Ref. [46]. The top curve is the observed spectrum and the bottom two are models.

Reproduced with permission of the copyright owner. Further reproduction prohibited without permission.

the results of Forster et al. [21] to their reported four significant figure accuracy and with the computations of Henry and O'Connell [11] confirming the previous calculations and the 2 nm discrepancy. One might suggest that relativistic effects could account for some or all of the difference, but Henry and O'Connell [11] estimate its influence to be only $\sim 10^{-3}$ nm. In the absence of a magnetic field, relativistic corrections increase the binding energy and examination of Table 2.1-2 shows that this binding increase is larger for the ground state than excited states resulting in a shorter transition wavelength. Taking the relativistic energies determined by Chen and Goldman [37] and the nonrelativistic energies of Sec. 2.1 or Rösner et al. [20] near 235 MG ($B = 1$ au) gives a relativistic correction of -0.0021 nm in agreement with Henry and O'Connell [11]. The variational relativistic correction computations performed in Sec. 2.1.4 and tabulated in Appendix B show that the correction is on the above order for applicable field strengths.

The origin of the discrepancy appears to be not in the magnetic field dependent atomic structure calculations, but possibly in the other environmental factor peculiar to white dwarfs, namely high density. Clues for this interpretation come from another mystery in DA white dwarfs provided by the *IUE*, the famous 140.4 and 162.3 nm features. These features have been identified [156,157] as Lyα satellites due to H-H^+ [158] and H-H [159,160] collisions. Allard and Kielkopf [161] have investigated the temperature and density dependence of the satellites while Allard and Koester [162] have produced synthetic spectra longward of Lyα for DAs of various effective temperatures. The *IUE* spectra of Grw +70°8247 contain previously undiscussed features at 140.8 and 164 nm with profiles that compare reasonably well to the synthetic spectrum of Ref. [162] for $T_{eff} = 13{,}000$ K (see their Fig. 7). Shifting of the 140.4 and 162.3 features by the magnetic field is certainly a seductive explanation. Magnetic-field-dependent computations of the Lyα satellites have not been performed, but one can get a rough idea of the expected shifting by examining the associated molecular

Reproduced with permission of the copyright owner. Further reproduction prohibited without permission.

potentials.

According to Steward, Peek, and Cooper [158] there are actually three satellites on the red wing of Lyα due to H-H^+ collisions which are given in Table 4.1-1 with wavelengths of 123.4, 124.0, and 140.4 nm and result from the molecular transitions $1s\sigma_g \leftarrow 4f\sigma_u$, $1s\sigma_g \leftarrow 2p\pi_u$, and $2p\sigma_u \leftarrow 3d\sigma_g$, respectively. The first two satellites are not observed in white dwarfs due to weaker absorption coefficients and close proximity to the Lyα core. Both the $4f\sigma_u$ and $3d\sigma_g$ correlate to $H(2p_0)+H^+$ in the separated atom limit while the $2p\pi_u$ is degenerate and correlates to $H(2p_{\pm 1})+H^+$. The magnetic field will remove the $2p\pi_u$ degeneracy giving a total of four transitions to consider.

Peek and Katriel [163] have determined the equilibrium distance R_e and dissociation energy for all H_2^+ states listed above for $B = 0$, 100, and 500 MG. Table 4.1-1 displays estimates of the location of the Lyα satellites for the various given field strengths using atomic energies from Sec. 2.1 and the dissociation energies of Ref. [163]. All the satellites remain redshifted from the atomic lines though the 123.4 and 124.0 ($m = 1$) satellites blueshift to wavelengths less than 120 nm, below the *IUE* spectral range. Interestingly, the 140.4 satellite appears to remain relatively stationary shifting only to 140.5 nm at 100 MG and may therefore be responsible for the 140.8 feature. The 124.0 ($m = -1$) feature is also redshifted but to near 130 nm for 100 MG. Inspection of the *IUE* spectra given in Greenstein [152] (see his Fig. 1) reveals a shallow depression near 130 nm which may possibly be explained by the shifted 124.0 ($m = -1$) satellite.

Little can be inferred about the H-H satellite since the H_2 potentials have not been investigated at these field strengths, though some speculation can be given by inspecting the field-free curves. According to Sando, Doyle, and Dalgarno [159] the 162.3 nm satellite results from the $X\,^1\Sigma_g^+ \leftarrow B\,^1\Sigma_u^+$ transition which occurs at closest approach near $R = 4$ a_o. Now, the equilibrium distances of the X and B states are

Reproduced with permission of the copyright owner. Further reproduction prohibited without permission.

1.40 and 2.44 a_o, respectively indicating that the transition occurs closer to the R_e of the B state and on the shoulder of the X state. A magnetic field has the effect of increasing the binding energy. One would expect the binding increase at the transition distance to be larger for the B state resulting in longer wavelength absorption which may account for the shift to 164 nm.

Finally, if the identification of the 141 and 164 nm features as Zeeman-shifted Lyα satellites is correct, it has profound implications for the line center and line strength of the Lyα σ^-. The total oscillator strength for the Lyα transition must be conserved. The satellites obtain their strength by borrowing from the line core. The strength of these satellites increase with density. Allard and Kielkopf [161] show the Lyα line strength is reduced by an order of magnitude as the density is increased from 10^{21} to 2.5×10^{21} cm^{-3} (see their Fig. 10). While white dwarfs typically have densities of 10^{20} cm^{-3} at optical depth $\tau = 1$, Grw +70°8247 is believe to be one of the most massive white dwarfs [155] and may actually have a higher density.

In summary it is proposed that the observed redshift and strength reduction of the Lyα σ^- line from theoretical atomic structure and radiative transfer computations is a consequence of the collisions of hydrogen atoms with protons and other hydrogen atoms in the strong magnetic field and high density environment of Grw +70°8247.

TABLE 4.1-1. Approximate wavelengths of the Lyα satellites at various magnetic field strengths. Lyα components are given for comparison.

B (MG)	λ (nm)			
	$1s\sigma_g \leftarrow 2p\pi_u(m=-1)$	$1s \leftarrow 2p_{-1}$	$1s\sigma_g \leftarrow 2p\pi_u(m=1)$	$1s \leftarrow 2p_1$
0	124.0	121.5	124.0	121.5
100	130.0	127.0	116.5	114.2
500	144.0	134.0	88.0	84.5
	$2p\sigma_u \leftarrow 3d\sigma_g$	$1s\sigma_g \leftarrow 4f\sigma_u$	$1s \leftarrow 2p_0$	
0	140.4	123.4	121.5	
100	140.5	119.0	121.0	
500	139.3	116.0	112.5	

Reproduced with permission of the copyright owner. Further reproduction prohibited without permission.

The $2p_0 \rightarrow 3d_{-1}$ *transition.* A feature at 842.0 nm is observed with a broad linewidth of $\sim$ 1.5 nm. The wavelength agrees with the previous structure calculations of the Tübingen and LSU groups. The synthetic spectra computation of WF shown in Figure 4.1-2 predicts the correct transition wavelength, but gives a much narrower linewidth of $\sim$ 0.5 nm and $\sim \frac{1}{3}$ the strength.

This transition was recalculated in Sec 2.1. The new results give excellent agreement with the Forster et al. calculation to the four significant figure accuracy quoted in Ref. [21] for both the wavelength and transition probability. The feature may be a blend of other undetermined lines.

The $3d'_0 \rightarrow 5p'_0$ *transition.* A deep absorption feature at 720 nm is observed in the spectrum of Grw +70°8247. The synthetic spectra of WF predict a feature at 662 nm due to the $3d'_0 \rightarrow 5p'_0$ transition which is not observed and no feature at 720 nm using the LSU data. Conversely, use of the Tübingen data gives a 720 nm feature for the $3d'_0 \rightarrow 5p'_0$ and no 662 nm feature indicating a $\sim$ 60 nm error in the LSU calculation.

We have recalculated this transition and obtain agreement with the Tübingen wavelengths confirming the error in the LSU values.

The $3d'_0 \rightarrow 4p'_0$ *transition.* Using the transition data of Henry and O'Connell [12], the model of WF predicts a strong and sharp feature at 883.0 nm due to the $3d'_0 \rightarrow 4p'_0$ transition which is not apparent in the observed spectrum (see Figure 4.1-2). WF suggest this is an error in the LSU group calculation of Henry and O'Connell and that the transition may actually be shifted $\sim$ 30 nm to the blue to aid in reconciling the large width of the 842 nm feature.

The transition is not presented in the Tübingen group calculation of Forster et al. [21], but the required energies are given in Rösner et al. [20]. One can obtain the wavelengths of 893.2 $\pm$ 1.4, 891.4 $\pm$ 0.7, and 944.25 $\pm$ 0.34 nm for 235, 329, and 470 MG, respectively. This appears to reaffirm the LSU calculation. The wavelength uncertainties are due to poor convergence of the $4p'_0$ energies to only two or three

Reproduced with permission of the copyright owner. Further reproduction prohibited without permission.

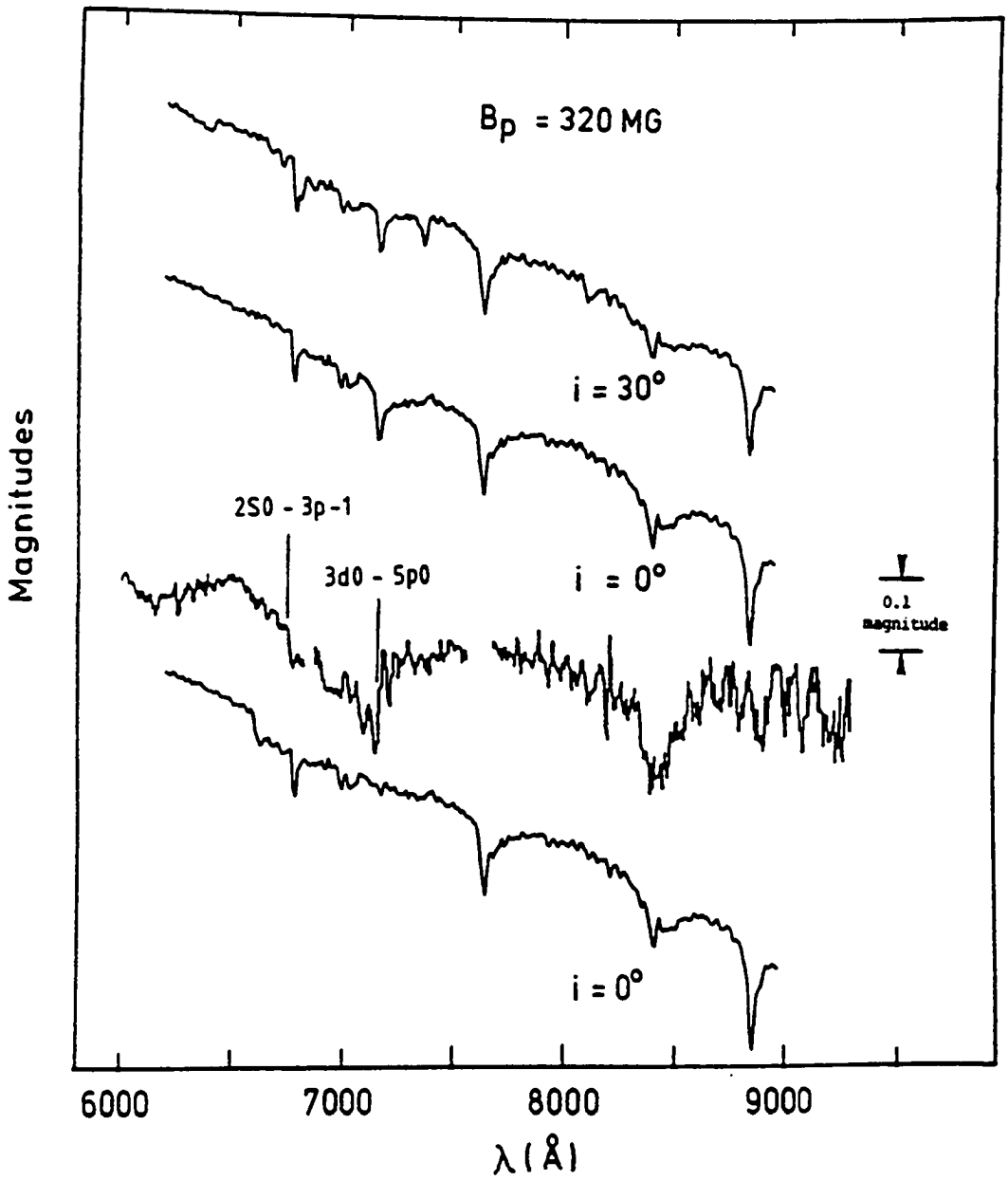

FIG. 4.1-2. Observed and modeled infrared spectra of Grw +70°8247 from Ref. [46]. The top two curves are models using Tübingen group calculations [21], the third from the top is the observed spectrum, and the bottom is a model using LSU computations [12].

Reproduced with permission of the copyright owner. Further reproduction prohibited without permission.

figures at the indicated field strengths.

The transition is computed in Sec. 2.1. We also find convergence of the $4p_0'$ state difficult for the field strengths of interest, but obtain a wavelength of 890 nm at 320 MG and longer wavelengths for weaker fields. Since WF determine that the maximum field on the stellar surface is $\sim$ 320 MG, our calculation and that of Rösner et al. indicate that this transition cannot contribute any absorption less than $\sim$ 890 nm and therefore Henry and O'Connell's data, of which no numerical values have been published, appear to be in error by $\sim$ 7 nm in the opposite direction suggested by WF. This shift is in better agreement with the observations and may account for an absorption feature at $\sim$ 890 nm with comparable depth and width.

Implications of hydrogen photoionization in a strong magnetic field. The most pressing issue for the modeling of magnetic white dwarfs is the lack of hydrogen bound-free opacities in strong fields. These are expected to be important in the UV, visible, and possibly the near infrared regions of the spectrum. WF, in their modeling of Grw +70°8247, use the approximation of Lamb and Sutherland [164] to estimate the continuum opacities from zero-field hydrogen cross sections using the relation

$$\sigma(E_{\rm ph}, B) = \frac{E_{\rm ph}}{E_{\rm ph} - E_{\rm s}} \sigma(E_{\rm ph} - E_{\rm s}, B = 0) \qquad (4.1\text{-}1)$$

where $E_{\rm s} = E(B) - E(B = 0)$. This procedure splits and shifts the photoionization threshold in a fashion analogous to the splitting and shifting of the bound state energies. Apparently, WF include only the Balmer continuum opacity which splits into four components. They obtain good agreement with the observed flux spectrum for the 300-620 nm range, but above 620 nm there are significant discrepancies between the model and observations as shown in Figure 4.1-2 presumably due to the approximations for the bound-free opacities. In particular, for the wavelength range 760-920 nm, a forest of deep absorption features appear in the observed spectrum, but are not predicted by the model. More telling are synthetic spectra of linear and circular polarization which show little agreement with observed optical polarization spectra.

Reproduced with permission of the copyright owner. Further reproduction prohibited without permission.

Later, Jordan [47] improved the approximation by determining the threshold energy as the difference between the bound state energy and the lowest Landau level assessible by a particular Δm transition. This splits the Balmer threshold into twelve components with eight independent wavelengths. While this approach appears to account for the proper end-points of the transition, synthetic polarization spectra computed by Jordan [47] show no improvement over the results of WF.

The major difficulty with this approximation is that much of the interesting atomic physics of the problem is ignored. It is well known that in the absence of a magnetic field a progression or manifold of Rydberg states exists just below the ionization limit. As $n \rightarrow \infty$, the manifold merges into the continuum. When a magnetic field is applied, an infinite set of Rydberg manifolds is projected out of the field-free continuum, but with each progression having a Landau level as its series limit and its ground state just above the next lower Landau level. The energy of a Landau level is given by

$$E_N^m(B) = \left(N + \frac{|m| + m + 1}{2}\right)B \qquad (4.1\text{-}2)$$

above the field-free ionization limit. Therefore, each series limit is separated by an energy B with the first, $N = 0$, limit $B/2$ above the field-free limit. The "bound" states of the $N = 1$ series overlap the $N = 0$ continuum, likewise the $N = 2$ series overlaps the $N = 1$ and $N = 0$ continua, and so on as $N \rightarrow \infty$. This gives a multitude of autoionization states which merge into the normal, bound hydrogen states of the $N = 0$ manifold and as such the idea of a bound-free absorption edge or threshold is meaningless.

This behavior has been recognized since the early low-resolution photoabsorption measurements of Garton and Tomkins [53] on Ba. In the absence of a field, the spectrum shows a uniform series of bound-bound lines that merge smoothly into a featureless continuum. With the application of a 4.7 T field, the smooth progression turns into a seemingly chaotic assemblage of unevenly spaced and varying amplitude peaks that persist well into the continuum. More recent high-precision measurements

Reproduced with permission of the copyright owner. Further reproduction prohibited without permission.

have investigated the behavior of H, He, and Li [54–56] with theoretical computations reproducing the observed spectra to amazing detail [50–52], but little attention has been given to the intermediate-field regime. Alijah, Hinze, and Broad [59] computed a small portion of the photoionization cross section from the 1*s* state at 20 MG and noted a multitude of resonances qualitatively similar to the low field observations. The most extensive calculation to date is the work of Wang and Greene [60] who determined cross sections at 11.75, 23.5, 47.0 117.5, and 235.0 MG from the ground state using multichannel quantum defect theory (MQDT). Their computations include the first ten Landau levels and reveal to high precision a series of resonance and interference phenomena. Unfortunately, these results are of little astrophysical utility since they are presented in a graphical form and have wavelengths in the far UV shorter than 90 nm which is below the *IUE* short wavelength limit of 120 nm and near the long wavelength limit of the *Extreme Ultraviolet Explorer (EUVE)* which has a 20-75 nm window. In addition, MQDT gives a precision that is unnecessarily high for astrophysical applications where current flux and polarization measurements have a resolution of only ~ 0.1 nm.

Further progress in modeling flux and polarization measurements require cross sections from excited states that contribute to the visible and near IR. The computations need to be for a sufficiently fine field grid, but with a resolution comparable to the measurements only. Table 4.1-2 gives a list of photoionization "thresholds" from excited states at $B = 320$ MG; clearly many continua in addition to the Balmer continuum considered by WF need to be included to accurately model the visible polarization of Grw $+70°8247$.

It is anticipated that the accurate wave functions computed in Sec. 2.1 will be useful for investigations of photoionization in strong fields by time-dependent methods. In the time dependent approach, the cross section is given by the Fourier transform of the autocorrelation function which is the overlap of the initial state wave function

Reproduced with permission of the copyright owner. Further reproduction prohibited without permission.

TABLE 4.1-2. Hydrogen photoionization thresholds for $B = 320$ MG.

State	λ_T (nm)	State	λ_T (nm)
$1s$	80.9	$2p_1$	552
$2p_{-1}$	205	$3d'_0$	607
$2p_0$	264	$3p_0$	642
$3d_{-2}$	290	$4d_{-2}$	659
$2s$	305	$5f_{-3}$	742
$4f_{-3}$	353	$4d_{-1}$	804
$3d_{-1}$	384	$5f_{-2}$	917
$4f'_{-2}$	468	$4f'_{-1}$	980
$3p_{-1}$	535	$3s'_0$	1057
$5g_{-3}$	535		

Reproduced with permission of the copyright owner. Further reproduction prohibited without permission.

with the time-propagated final wave function [61]. The precision of the cross section can be controlled by limiting the propagation time.

4.1.2. Other Magnetic Stars

Absorption features near 140 and 162 nm appear in the *IUE* spectra of the DAP6 ($B = 36$ MG) star BPM 25114 (WD 1743-521) and KUV 2316+123, a 29 MG DAP. These features may possibly be interpreted as the Lyα satellites discussed in Sec. 4.1.1. The *IUE* spectrum of PG 1034+234 is too noisy at these wavelengths to discern any features although an absorption line is present at 117.5 nm, just blueward of the Lyα geocoronal emission, and may be due to the Lyα π component in a field of $\sim$ 300 MG.

4.1.3. Hot Magnetic White Dwarfs

As previously mentioned, H I, He I, and He II absorption lines form in white dwarf spectra for $T_{eff} > 5000$, 13,000, and 30,000 K, respectively. Lines of C IV, N V, and O VI have been observed in white dwarfs with temperatures greater than 100,000 K. Temperatures for the known population of magnetic white dwarfs do not exceed 30,000 K and hence only Zeeman-shifted lines of H I and He I have been observed. Higher temperature magnetic stars are not physically excluded; their absence is probably related to a combination of high cooling rate and rarity of magnetic stars in general. Nevertheless, there is some possibility that high temperature magnetic white dwarfs will be found, particularly with the launching of the *EUVE*, and lines of highly ionized atoms will be observed.

For these possible observations, we determined wavelengths and transition probabilities from some of the hydrogen results. The energies incorporate the combined nuclear mass and nuclear charge scaling relation (2.1-15), while the dipole moments used the charge scaling relation (2.1-43). Some data for He^+ is given in Appendix D. These wavelengths neglect relativistic corrections and are therefore only reliable to

Reproduced with permission of the copyright owner. Further reproduction prohibited without permission.

$\sim 10^{-2}$ nm since the hydrogen corrections are $\sim 10^{-3}$ nm as discussed in Sec. 4.1.1 and the relative correction scales as $\sim Z^2$ according to Sec. 2.1.4. For highly charged ions such as C^{5+}, N^{6+}, and O^{7+}, the correction is ~ 0.1 nm which is on the order of the current observational resolution. This presents the possibility of observing relativistic effects in hydrogenlike ions if a hot magnetic white dwarf is discovered. Data for these ions will be given in the future after the discrepancies in the relativistic corrections are reconciled.

Reproduced with permission of the copyright owner. Further reproduction prohibited without permission.

4.2. Cool White Dwarfs

4.2.1. The Effect of Pressure on Atomic Partition Functions

The divergence of the atomic partition function due to the sum over the excited states of an isolated atom is a well-known problem. It is usually avoided by choosing an appropriate, but more often arbitrary, cutoff for the sum. Irwin [133] chose a binding energy of 0.1 eV for his partition function cutoff corresponding to the inclusion of the first 11, 23, and 11 levels for H, He^+, and He, respectively. It turns out that the partition function, at least for H, is sensitive to the number of terms included at high temperatures [144]. More importantly, the actual cutoff is related to the physical environment in which the atom finds itself, i.e., temperature, pressure, and composition, which dictates the highest excited level that can be populated with remaining higher states delegated to the continuum. This has the effect of pushing the photoionization threshold to longer wavelengths. Determinations of the cutoffs in cool white dwarfs are clearly discussed by Bergeron, Wesemael, and Fontaine [165] (hereafter BWF) where it is shown that the cutoffs themselves result in discontinuity problems when obtaining opacities. Instead, a formalism developed by Hummer and Mihalas [144] incorporated by BWF where a modified partition function is used and is given by

$$Q'_{\rm X}(T) = \sum_i \omega_i g_i \exp(-E_i/k_{\rm b}T), \tag{4.2-1}$$

where ω_i is a occupation probability of the excited state i and varies smoothly with optical depth.

To estimate this effect, we determined $Q'_{\rm H}$ using the occupation probabilities obtained in BWF (see their Fig. 7) for models of pure-hydrogen cool DA white dwarfs with $\log\ g\ =\ 8.0$ and compared to the results of Irwin [133]. The largest discrepancy we find is only 3% for a model with an effective stellar temperature $T_{eff} = 12,000$ K

Reproduced with permission of the copyright owner. Further reproduction prohibited without permission.

and optical depth $\tau = 10$ ($T = 20{,}000$ K). For $T_{eff} = 9000$ K, the discrepancy does not exceed 0.3%. The equilibrium constants given in Table 3.3-1 should therefore be appropriate for cool white dwarfs within the above quoted discrepancies.

Irwin [133] gives $Q_{He^+} = 2$ up to 60,000 K while $Q_{He} = 1$ with a variation of only 0.2% over the range 1000 to 60,000 K, indicating that the He_2^+ equilibrium constants given in Table 3.3-2 should also be reliable for cool white dwarfs. While the equilibrium constants for both molecules could be improved by applying the occupation probability formalism to white dwarf models, its effect on the molecular absorption coefficients of Sec. 3.2 would be minimal.

4.2.2. He_2^+ and H_2^+ Detection Prospects

It has been suggested by Gaur et al. [166] (henceforth GTJP) that He_2^+ and H_2^+ are the most abundant molecules in non-DA and DA white dwarfs, respectively, with the exception in DA stars of H_2. Of all white dwarfs, only the cool helium-rich DQ stars have been observed to contain molecular features. The observed DQ dwarfs which number approximately 25 [167] all generally reveal absorption features due to the C_2 Swan band. CH has been observed in only one white dwarf.

For the helium-rich models considered by GTJP, $n(He_2^+)$, the abundance of He_2^+ exceeds C_2 by at least an order of magnitude at all τ for $T_{eff} > 9000$ K. For lower temperatures, $n(He_2^+)$ exceeds $n(C_2)$ for $\tau > 1$ only. For DA models, $n(H_2^+)$ is comparable to $n(He_2^+)$ in the non-DA models. It therefore seems plausible if C_2 is observed, He_2^+ and H_2^+ should be as well.

Since the stars likely to contain these molecules are cool, one might suggest the IR would be the obvious spectral region to investigate. Unfortunately, there is unlikely to be a detection of RV lines; since these molecules are homonuclear; RV electric dipole transitions are forbidden. The He_2^+ electric quadrupole transitions (1,0) Q(1) and (1,0) O(1) occur at 6.16 μm and 5.91 μm, respectively, but with strengths which are undoubtably weak.

Reproduced with permission of the copyright owner. Further reproduction prohibited without permission.

The lowest lying attractive electronic states of He_2^+ which could connect to the ground state by allowed dipole transitions are the 2 $^2\Sigma_g^+$ and 1 $^2\Pi_g$ states giving bands near 50 nm and 45 nm, respectively. The energies of the RV levels in these excited states are currently unavailable so that line locations and strengths cannot be obtained.

Similar considerations are applicable to H_2^+, except for a lack of electronic transitions due to the nonexistence of attractive excited states that can support bound RV levels. Some states, however, do contain van der Waals minima at large R which may allow for a few bound RV levels, but due to poor wave function overlap with the ground state, the transitions are weak. The RV quadrupole transitions (1,0) Q(0) and (1,0) O(0) occur at 4.56 μm and 4.24 μm, respectively with transition probabilities of the order 10^{-7} s^{-1} [168].

From the above discussion, it appears that the subject of Sec. 3.2, continuum absorption, may prove to be the only hope for detection. Unfortunately, there is no discernible feature in the cross sections of either He_2^+ or H_2^+, except for a broad peak in the UV. But the cross sections are large and according to GTJP, the molecular abundances should also be large suggesting a significant contribution to the continuum opacity. For late-type stars, Mihalas [134] has suggested that H_2^+ may contribute up to 20% of the opacity in the visible region.

4.2.3. Hydrogen-Rich Stars

In a study of a number of cool white dwarfs, Wickramasinghe, Allen, and Bessell [169] (hereafter WAB) noted that some stars classified as DK (currently called DZ) and DC contained flux deficiencies in the Johnson $(U-B)$ and the Strömgren $(u-b)$ colors. A model atmosphere calculation for a hydrogen-rich DA star (T_{eff} = 5000 K) by WAB showed that the H_3^+ abundance $n(H_3^+)$ exceeded $n(H_2^+)$ by at least an order of magnitude for $\tau \leq 1$. They subsequently suggested that H_3^+ was responsible for the $(U-B)$ and $(u-b)$ deficiencies. This concept was previously put forth by Linsky

Reproduced with permission of the copyright owner. Further reproduction prohibited without permission.

[170] to account for missing opacity in the solar ultraviolet, but was rejected due to an apparently low H_3^+ abundance. Since Linsky's suggestion, the photodissociation of H_3^+ has been investigated by many authors [171–173] who have shown that the cross section from the $v'' = 0$ level of the ground state to the first excited state $^1A_1$ peaks at 58 nm with a small magnitude of 10^{-21} cm^2. Though a total temperature-dependent cross section is unavailable, the above value is a good estimate of the upper-limit for $\lambda \geq$ 58 nm.

To ascertain the continuum opacity importance of H_3^+, the abundance ratios calculated by WAB for H_3^+, H_2^+, and H^- in conjunction with the partial pressures of H_2^+ and H_2 from GTJP (their model set III) and the atmospheric structure models of BWF (see their Fig. 1) were used. Unfortunately, GTJP did not investigate polyatomic molecules and we were also required to extrapolate the H_2^+ and H_2 data to 5000 K. H_2 has been included since it is apparently the most abundant molecule in cool DA white dwarfs and its continuum opacity is addressed through photodissociation [161], photoionization and dissociative ionization [175], and the Lyα wing quasimolecular opacity [160]. We further include the H_2^+ quasimolecular broadening of Lyα [158], H^- photodetachment [176], and H photoionization. The effect of density on the Lyα wing as discussed by Allard and Kielkopf [161] does not appear to be important for these particular cool stars and is not included. The H_2 pressure-induced and H^- free-free opacities are neglected since they are only important in the IR.

Fig. 4.2-1 shows the total opacity for each species at $\tau = 1$. A similar plot is produced for $\tau = 0.01$. Atmospheric parameters used in the calculation are also given in the figure. Only partial photodissociation cross sections from $v'' = 0$, 1, and 2 for H_3^+ and from $v'' = 0$ and 14 for H_2 are displayed. Clearly, H^- and H_2^+ are the dominant opacity sources for $\lambda \geq$ 200 nm, while H_3^+ is negligible. The $(U - B)$ deficiency cannot be attributed to H^- since its cross section has the wrong wavelength behavior or H_2^+ since its abundance appears to be too low. This suggests

Reproduced with permission of the copyright owner. Further reproduction prohibited without permission.

Reproduced with permission of the copyright owner. Further reproduction prohibited without permission.

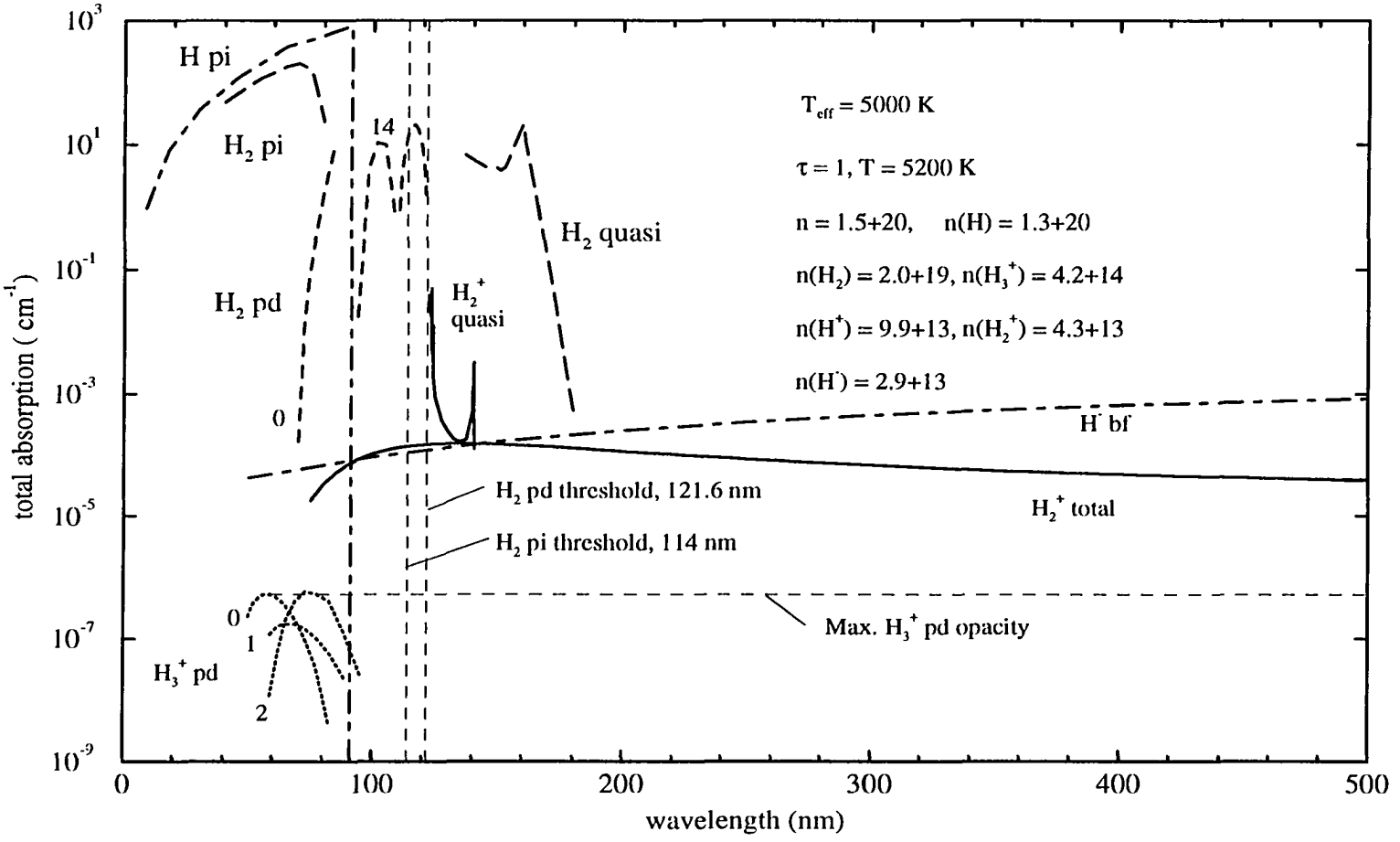

FIG. 4.2-1. Continuum opacities for a cool hydrogen-rich DA white dwarf with $\tau = 1$, $T_{eff} = 5000$ K, and log g = 8.

some unknown opacity source.

4.2.4. Helium-Rich Stars

As mentioned previously, many DZ and DC stars have UV flux deficiences. Greenstein [177] has suggested that pressure-broadened lines due to metals in the photosphere may be responsible for the deficiencies, but it can be argued heavy elements do not contaminate a cool white dwarf's photosphere since radiative levitation occurs only for the hotter stars [178]. In addition, deficiencies in the EUV have not been observed for moderately hot stars with $T_{eff} \leq 35,000$ K [179]. It has also been noted by Greenstein [177] that the DB stars show deficiencies in Greenstein's multichannel U band when compared to the predicted fluxes from the models of Koester [180]. We offer the suggestion that for cool stars, $T_{eff} < 20,000$ K, the invocation of metals is unnecessary since the deficiencies may actually be due to He_2^+.

Using the partial pressures of He_2^+ from GTJP (their model set II) and the helium-rich models of Koester [180], we estimate the abundances and opacities for $T_{eff} = 12,000$ K, $\log g = 8.0$, and $n(\mathrm{He})/n(\mathrm{H}) = 10^5$ at $\tau = 1$. We also include the He^- free-free opacity [181] and photoionization of He from the ground 1^1S and first excited 2^3S states. Results are plotted in Fig. 4.2-2. The He_2^+ opacity exceeds He^- by almost an order of magnitude at U and B with the difference increasing for shorter wavelengths. Inclusion of He_2^+ in future DB, DZ, and DC models may bring them into closer agreement with observations.

4.2.5. Selected Individual Cool White Dwarfs

EG 56 (WD 0752-676, BPM 4729). This star was observed by Wegner [182] to reveal weak C_2 Swan band absorption features suggesting a helium-dominated atmosphere. Wickramasinghe and Bessell [183] later observed weak Hα and Hβ absorption lines indicating this star to be a hydrogen-rich DA. They determined $T_{eff} = 5500$ K assuming a surface gravity of $\log g = 8$. The later suggestion by WAB of H_3^+ fur-

Reproduced with permission of the copyright owner. Further reproduction prohibited without permission.

Reproduced with permission of the copyright owner. Further reproduction prohibited without permission.

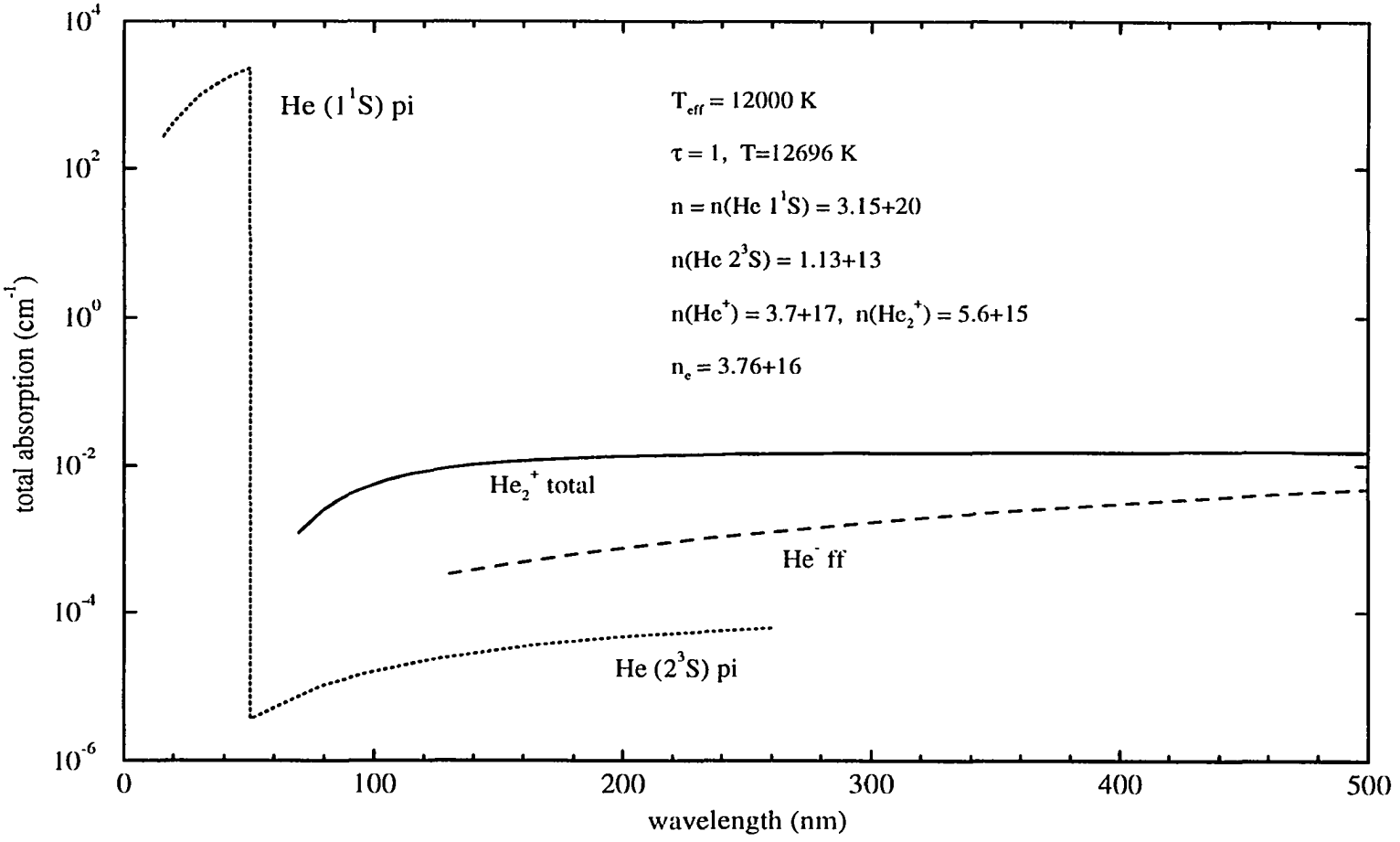

FIG. 4.2-2. Continuum opacities for a cool helium-rich DB white dwarf with $\tau = 1$, $T_{eff} = 12\,000$, and log g = 8.

ther pointed toward a hydrogen atmosphere. The above two works were apparently ignored in the white dwarf catalog of McCook and Sion [167] who classified EG 56 as DQ, indicating helium-rich. Though Sec. 4.2.3 refutes the H_3^+ claim and excludes H^- and H_2^+ as possible $(u-b)$ flux deficiency sources for this object, evidence supporting a hydrogen atmosphere comes from an investigation of helium contamination in a large sample of cool DA stars by Bergeron et al. [184]. Though their analysis indicates that helium contamination can reach as high as $n(\mathrm{He})/n(\mathrm{H}) \sim 25$ for $T_{eff} = 12{,}000$ K, their observations suggest a trend for cooler objects to have lower helium abundances. Extrapolating the upper envelope of their data (see their Fig. 1) gives $n(\mathrm{He})/n(\mathrm{H}) \leq 10^{-2}$ at $T_{eff} = 5500$ K. Further, the Hα and Hβ line depths observed by Wickramasinghe and Bessell [183] compare well to the DA synthetic spectra of BWF (see their Figs. 12, 13, and 14) at $T_{eff} = 5000$ K, $\log g = 8$, and $n(\mathrm{He})/n(\mathrm{H}) \leq 10^{-2}$. Any increase in $n(\mathrm{He})$ or $\log g$ would result in the disappearance of Hβ. This suggests that EG 56 has a hydrogen atmosphere.

G62-53 (WD 1334+039, Gr 100, W 489) and G 99-44 (WD 0552-041, Gr 45, LP 658-2). Both stars were observed by Eggen and Greenstein [185] to have Ca II absorption lines. Careful observations by Wehrse and Liebert [186] failed to detect Hα. Nevertheless, WAB suggested the stars were hydrogen-rich due to flux deficiencies in JHK and $(U-B)$ which they attributed to H_2 pressure-induced dipole opacity and H_3^+ opacity, respectively. The H_2 interpretation has been criticized by Greenstein [177] since a predicted strong feature at 2 μm has yet to be observed. Also, Greenstein [177] has attributed the $(U-B)$ deficiency to pressure-broadened metal lines in a helium-rich atmosphere. Subsequently, McCook and Sion [167] have retained the stars' original classification of DZ9. Both Sec. 4.2.3 and 4.2.4 contribute to the helium atmosphere argument by excluding H_3^+, H_2^+, and H^- as candidates for the $(U-B)$ deficiency while indicating He_2^+. Comparison of the synthetic spectra of BWF suggest three possible scenarios. For a pure hydrogen atmosphere Hα will be

Reproduced with permission of the copyright owner. Further reproduction prohibited without permission.

removed if (i) log $g = 8$ and $T_{eff} < 5000$ K or (ii) $T_{eff} = 5000$ K and log $g > 8.5$. A helium-contaminated atmosphere would require for (iii) $T_{eff} = 5000$ K and log $g = 8$, $n(\mathrm{He})/n(\mathrm{H}) > 1$. Assuming log $g = 8$, WAB find from their JHK photometry $T_{eff} = 5150$ K and 5000 K, respectively, essentially excluding (i). Since the mean surface gravity of the known population of white dwarfs is log $g = 8.0$ with a standard deviation of $\sigma_{\mathrm{d}} = 0.25$, option (ii) is unlikely. The presence of hydrogen in these stars may be checked through spectropolarimetry. If a star contains hydrogen and a magnetic field of at least 10 kG, a line feature in the circular polarization should appear at Hα even though no feature may be present in the flux. This technique was used successfully by Cohen, Putney, and Goodrich [187] to detect hydrogen in the magnetic star G227−35 which has a featureless flux spectrum and previously classified DCP. The above indicates these two stars may have helium-rich atmospheres as previously suggested or at least comparable hydrogen and helium abundances and that the $(U - B)$ deficiencies may be due to He_2^+.

4.2.6. The Ultraviolet and Extreme Ultraviolet

As mentioned in Sec. 4.2.2 the only prominent feature in the photodissociation cross sections is a broad peak in the UV, but both He_2^+ and H_2^+ show effectively temperature independent cutoffs or thresholds of the photodissociation cross sections in the EUV. These thresholds occur at $\sim$ 60 nm and $\sim$ 55 nm for He_2^+ and H_2^+, respectively. From Fig. 4.2-1, it is clear the photoionization opacity of H and H_2 will dominant this region completely obscuring H_2^+. Between the Lyα line and $\sim$ 200 nm the primary opacity is due to the H_2 quasimolecular broadening. H_2^+ appears to be a minor opacity source at all wavelengths.

The H_2 quasimolecular absorption, the famous 160 nm feature, has been observed in many cool DA white dwarfs by the *IUE* (see, for example, Koester et al. [156] and Nelan and Wegner [157] and the discussion in Sec. 4.1.1). The strength of the absorption is proportional to $n(\mathrm{H})^2$ and has been shown to increase with decreasing T_{eff}

Reproduced with permission of the copyright owner. Further reproduction prohibited without permission.

from 16,000 to 10,000 K. At $T_{eff} = 10,000$ K, the atmosphere becomes completely opaque for $\lambda < 160$ nm, but for lower temperatures n(H) begins to decrease as larger fractions of H become bound in H_2. If some flux is present at these wavelengths, H_2 in a cool white dwarf may be observed via its photodissociation. Its photoionization may also compete with the photoionization of H below 50 nm.

The situation for helium-rich atmospheres is less complicated since the ground state of He_2 is effectively repulsive and the cross section for He^- is weak. Though the He ground state photoionization threshold occurs at 50.4 nm, pressure quenching of the upper levels as discussed in Sec. 4.2.1 will shift it to longer wavelengths possibly swamping the He_2^+ EUV cutoff. But for $\lambda > 60$ nm, He_2^+ appears to be the dominant continuum opacity.

Depending on the distance to a particular star, absorption from the local interstellar medium may prove important. One can expect a strong, sharp Lyα core and H, He, and He^+ photoionization [188].

All of the stars in Sec. 4.2.5 have yet to be observed by the *IUE* [182]. Effects on the continuum may be observable if these or other cool, near stars are investigated in high-resolution mode with long integration times. Many DB stars with the Greenstein U deficiency appear in Wegner and Swanson's [189] tabulation and in particular the DBQ5 star WD 1917-077 has a deficiency in the Johnson $(U - B)$ as well. Coincidentally, the *EUVE* has recently become operational [190] with its long-wavelength window covering 28 to 76 nm. Though EUV sources are generally hot stars, two moderately cool white dwarfs are approved *EUVE* targets. These are the DA4 star PG 1123+189 and GD 356 (WD 1639+537), a DAP7 dwarf. The Johnson $(U - B)$ color of the DA4 star is unknown while GD 356 does not show a deficiency. Low-dispersion *IUE* spectra of these stars are too noisy to reveal any features; improved spectra may prove interesting. I am unaware of any DB, DC, DZ, or DQ stars which may be possible *EUVE* targets.

Reproduced with permission of the copyright owner. Further reproduction prohibited without permission.

5. CONCLUSIONS AND COMMENTS

This dissertation has presented a new tabulation of infinite proton mass energies for hydrogen in a magnetic field with some values for $n = 6$ states given for the first time. We give new magnetic field dependent forms for the velocity and acceleration dipole operators as well as the oscillator strength sum rule. A new procedure for obtaining relativistic effects through a perturbative expansion of the Pauli approximation corrections with the Zeeman Hamiltonian is attempted with varying success. We present a new tabulation of wavelengths and probabilities with transitions to $n = 6$ states given for the first time. We have confirmed the previous calculations of the $1s \rightarrow 2p_{-1}$, $2p_0 \rightarrow 3d_{-1}$, and $3d'_0 \rightarrow 5p'_0$ transitions which were suspected by Wickramasinghe and Ferrario [46] to be in error. A 7 nm shift to the red at 320 MG is found for the $3d'_0 \rightarrow 4p'_0$ transition as compared to the previous LSU [12] calculation giving better agreement with the spectra of Grw +70°8247. We suggest the observed shift in the $1s \rightarrow 2p_{-1}$ transition may be due to H-H^+ and H-H collisions in the strong magnetic field of Grw +70°8247 which may also account for observed features at 140.8 and 164 nm.

Quantum mechanical cross sections for radiative association and photodissociation and rate coefficients for the He_2^+ molecular system are given for the first time. It is shown that all rotational-vibrational levels must be included in a quantum mechanical calculation and agreement with semiclassical methods is then possible. This is demonstrated through the resolution of a discrepancy between previous calculations of H_2^+ photodissociation. New free-free absorption coefficients, partition functions, and dissociation equilibrium constants have also been obtained for H_2^+ and He_2^+.

While the major effort of this investigation has been to calculate atomic and molecular data useful for the analysis of magnetic and cool white dwarfs, much remains to be done. The astronomer is severely handicapped, even for the hydrogen-rich mag-

Reproduced with permission of the copyright owner. Further reproduction prohibited without permission.

netic stars, due to the lack of a comprehensive set of hydrogen photoionization cross sections. As discussed earlier, further progress in the modeling of flux spectra and polarization spectra, in particular, awaits the generation of these cross sections. More information concerning the details of the field structure of the star may be obtained from polarization measurements than from the absorption lines, but it is here where the major modeling discrepancies persist. For cooler stars, $T_{eff} \lesssim 6000$ K, H^- may become an important continuum opacity source. Our knowledge of photodetachment of H^- in strong magnetic fields is limited to the calculation of Du [191] for $B = 10^{-2}$ MG.

Further hydrogen work is required to investigate the suggestion given here that the 2 nm shift in the Lyα σ^- line and other UV absorption features in the famous star Grw +70°8247 may be explained by hydrogen-proton and hydrogen-hydrogen collisions. Calculations of H_2^+ and H_2 potentials and transition moments at the necessary field strengths and a detailed computation of the collision opacities versus field strength, pressure, and temperature will be needed.

There are currently eight known hydrogen-deficient magnetic white dwarfs with field strengths greater than 10 MG. They are all presumed to have helium-dominated atmospheres. Many have unidentified features which cannot be attributed to hydrogen in a magnetic field, but are probably helium lines. Reliable helium data exist for visible transitions up to only 20 MG [2,3]. Recently, the Tübingen group have applied their multiconfiguration Hartree-Fock techniques to triplet heliumlike states, but their wavelengths are not well converged in the intermediate-field regime [23]. To ascertain the accuracy of these results and other future many-electron field-dependent atomic structure calculations, it may be necessary to resort to a Hylleraas-type [68] procedure by explicitly introducing the interelectronic coordinate $r_{12} = r_1 - r_2$ into the basis functions. For field-free structure problems, the method has provided benchmarks for judging the accuracy of other calculations. Taking clues from the hydrogen

Reproduced with permission of the copyright owner. Further reproduction prohibited without permission.

problem, the magnetic-field-dependent symmetry can also be included by using a trial basis consisting of mixed Hylleraas- and Landau-type orbitals possibly of the form

$$\phi_{abc} = P_{ab}\Big[r_1^{n_a-1} r_2^{n_b-1} \exp(-\lambda'_a r_1 - \lambda'_b r_2 - \beta_a r_1^2 \sin^2\theta_1 - \beta_b r_2^2 \sin^2\theta_2)$$
$$\times \cos^{\ell_a-|m_a|}\theta_1 \cos^{\ell_b-|m_b|}\theta_2 \sin^{|m_a|}\theta_1 \sin^{|m_b|}\theta_2\Big] r_{12}^c \qquad (5\text{-}1)$$

where the operator P_{ab} interchanges the indices a and b. While many times more complicated than the hydrogen basis, the integrals can be evaluated and the method may prove the most accurate way to address simultaneously the problem of the magnetic field and electron-electron correlation. Further progress on identifying features in helium-rich magnetic white dwarfs would then be possible. Also, the wave function could be used to investigate H^- photodetachment and He photoionization.

The subject of molecules in white dwarfs has received little attention in the literature. The cool stars that contain significant molecular abundances have low luminosities particularly for UV and shorter wavelengths so high precision spectra are difficult to obtain. The only two molecules that have been observed, C_2 and CH, have electronic transitions in the visible. H_2 and He_2^+, the molecules expected to be the most abundant in DA and non-DA stars, respectively, have electronic transitions in the UV and hence are probably unobservable. Their RV transitions are forbidden. In this investigation, we have studied continuum absorption for He_2^+ and H_2^+, but find that there are no prominent features except for a weak, rounded peak and a sharp EUV cutoff. A comprehensive analysis of EUV, UV, and visible spectroscopy, a search for the cutoffs and absorption peaks, and modeling of the spectra with an emphasis on continuum absorption features may lead to a firm identification of He_2^+ or H_2 in a cool white dwarf. The prospects for H_2^+ appear dim.

Reproduced with permission of the copyright owner. Further reproduction prohibited without permission.

BIBLIOGRAPHY

[1] R. H. Garstang, Rep. Prog. Phys. **40**, 105 (1977) and references therein.

[2] R. H. Garstang and S. B. Kemic, Astrophys. Space Sci. **31**, 103 (1974).

[3] S. B. Kemic, JILA Rep. No. 113 (1974).

[4] R. O. Mueller, A. R. P. Rau, and L. Spruch, Phys. Rev. Lett. **26**, 1136 (1971).

[5] A. R. P. Rau, R. O. Mueller, and L. Spruch, Phys. Rev. A **11**, 1865 (1975).

[6] E. R. Smith, R. J. W. Henry, G. L. Surmelian, R. F. O'Connell, and A. K. Rajagopal, Phys. Rev. D **6**, 1700 (1972).

[7] G. L. Surmelian and R. F. O'Connell, Astrophys. Space Sci. **20**, 85 (1973).

[8] E. R. Smith, R. J. W. Henry, G. L. Surmelian, and R. F. O'Connell, Astrophys. J. **179**, 659 (1973); Astrophys. J. **182**, 651 (1973).

[9] G. L. Surmelian, R. J. W. Henry, and R. F. O'Connell, Phys. Let. **49A**, 431 (1974).

[10] R. J. W. Henry, R. F. O'Connell, E. R. Smith, G. Chanmugam, and A. K. Rajagopal, Phys. Rev. A **9**, 329 (1974).

[11] R. J. W. Henry and R. F. O'Connell, Astrophys. J. **282**, L97 (1984).

[12] R. J. W. Henry and R. F. O'Connell, Pub. Ast. Soc. Pac. **97**, 333 (1985).

[13] H. S. Brandi, R. R. Santos, and L. C. M. Miranda, Lett. Nuovo. Cim. **16**, 187 (1976).

[14] J. M. Wadehra, Astrophys. J. **226**, 372 (1978).

[15] J. M. Wadehra, Astrophys. J. **248**, 248 (1981).

[16] S. M. Kara and M. R. C. McDowell, J. Phys. B **13**, 1337 (1980).

[17] G. Wunner, Astrophys. J. **240**, 971 (1980).

[18] G. Wunner and H Ruder, Astrophys. J. **242**, 828 (1980).

[19] P. Pröschel, W. Rösner, G. Wunner, H. Ruder, and H. Herold, J. Phys. B **15**, 1959 (1982).

[20] W. Rösner, G. Wunner, H. Herold, and H. Ruder, J. Phys. B **17**, 29 (1984).

Reproduced with permission of the copyright owner. Further reproduction prohibited without permission.

[21] H. Forster, W. Strupat, W. Rösner, G. Wunner, H. Ruder, and H. Herold, J. Phys. B **17**, 1301 (1984).

[22] G. Wunner, F. Geyer, and H. Ruder, Astrophys. Space Sci. **131**, 595 (1987).

[23] G. Thurner, H. Körbel, M. Braun, H. Herold, H. Ruder, and G. Wunner, J. Phys. B **26**, 4719 (1993).

[24] J. C. Le Guillou and J. Zinn-Justin, Ann. Phys. (NY) **147**, 57 (1983).

[25] J. B. Delos, S. K. Knudson, and D. W. Noid, Phys. Rev. A **28**, 7 (1983).

[26] C.-H. Park and A. F. Starace, Phys. Rev. A **29**, 442 (1984).

[27] C. Liu and A. F. Starace, Phys. Rev. A **35**, 647 (1987).

[28] P. B. Jones, Phys. Rev. Lett. **55**, 1338 (1985).

[29] D. Neuhauser, S. E. Koonin, and K. Langanke, Phys. Rev. A **36**, 4163 (1987).

[30] M. C. Miller and D. Neuhauser, Mon. Not. R. Astr. Soc. **253**, 107 (1991).

[31] M. V. Ivanov, J. Phys. B **21**, 447 (1988).

[32] J. Shertzer, Phys. Rev. A **39**, 3833 (1989).

[33] G. Fonte, P. Falsaperia, G. Schiffrer, and D. Stanzial, Phys. Rev. A **41**, 5807 (1990).

[34] F. M. Fernandez and J. A. Morales, Phys. Rev. A **46**, 318 (1992).

[35] J. Xi, L. Wu, X. He, and B. Li, Phys. Rev. A **46**, 5806 (1992).

[36] E. H. Lieb, J. P. Solovej, and J. Yngvason, Phys. Rev. Lett. **69**, 749 (1992).

[37] Z. Chen and S. P. Goldman, Phys. Rev. A **45**, 1722 (1992).

[38] Z. Chen and S. P. Goldman, Phys. Rev. A **48**, 1107 (1993).

[39] C. Cuvelliez, D. Baye, and M. Vincke, Phys. Rev. A **46**, 4055 (1992).

[40] F. Y. Hajj, J. Phys. B **26**, 613 (1993).

[41] M. R. M. Witwit and J. P. Killingbeck, J. Phys. B **26**, 1599 (1993).

[42] D.-S. Chuu and Y.-K. Lee, Phys. Rev. A **48**, 4175 (1993).

[43] E. P. Lief and J. C. Weisheit, Phys. Rev. A, in press (1994).

[44] J. Trümper et al., Astrophys. J. **219**, L105 (1978).

Reproduced with permission of the copyright owner. Further reproduction prohibited without permission.

[45] J. C. Kemp, J. B. Swedlund, J. D. Landstreet, and J. R. P. Angel, Astrophys. J. **161**, L77 (1970).

[46] D. T. Wickramasinghe and L. Ferrario, Astrophys. J. **327**, 222 (1988) (WF).

[47] S. Jordan, *White Dwarfs*, IAU Colloquium No. 114, edited by G. Wegner (Springer-Verlag, Berlin, 1988).

[48] P. F. O'Mahony and K. T. Taylor, Phys. Rev. Lett. **57**, 2931 (1986).

[49] M. L. Du and J. B. Delos, Phys. Rev. Lett. **58**, 1731 (1987).

[50] D. Delande, A. Bommier, and J. C. Gay, Phys. Rev. Lett. **66**, 141 (1991).

[51] P. F. O'Mahony and F. Mota-Furtado, Phys. Rev. Lett. **67**, 2283 (1991).

[52] S. Watanabe and H. Komine, Phys. Rev. Lett. **67**, 3227 (1991).

[53] W. R. S. Garton and F. S. Tomkins, Astrophys. J. **158**, 839 (1969).

[54] A. Holle, G. Wiebusch, J. Main, B. Hager, H. Rottke, and K. H. Welge, Phys. Rev. Lett. **56**, 2595 (1986).

[55] C. Iu, G. R. Welch, M. M. Kash, D. Kleppner, D. Delande, and J. C. Gay, Phys. Rev. Lett. **66**, 145 (1991).

[56] J. Main, G. Wiebusch, K. Welge, J. Shaw, and J. B. Delos, Phys. Rev. A., in press (1994).

[57] W. Schmitt, H Herold, H. Ruder, and G. Wunner, Astron. Astrophys. **94**, 194 (1981).

[58] G. Wunner, H. Ruder, H. Herold, and W. Schmitt, Astron. Astrophys. **117**, 156 (1983).

[59] A. Alijah, J. Hinze, and J. T. Broad, J. Phys. B **23**, 45 (1990).

[60] Q. Wang and C. H. Greene, Phys. Rev. A **44**, 7448 (1991).

[61] W. P. Reinhardt, J. Phys. B **16**, L635 (1983).

[62] J. E. Bjorkholm and P. F. Liao, Phys. Rev. Lett. **33**, 128 (1974).

[63] A. C. Tam and C. K. Au, Optics Comm. **19**, 265 (1976).

[64] D. Zei, R. N. Compton, J. A. D. Stockdale, and M. S. Pindzola, Phys. Rev. A

Reproduced with permission of the copyright owner. Further reproduction prohibited without permission.

40, 5044 (1989).

[65] L. Cook, D. Olsgaard, M. Havey, and A. Sieradzan, Phys. Rev. A **47**, 340 (1993).

[66] S. G. Alexander and P. Mészáros, Astrophys. J. **372**, 554 (1991).

[67] S. G. Alexander and P. Mészáros, Astrophys. J. **372**, 565 (1991).

[68] H. A. Bethe and E. E. Salpeter, *Quantum Mechanics of One- and Two-Electron Atoms*, (Plenum, New York, 1977).

[69] J. M. Anthony and K. J. Sebastian, Phys. Rev. A **49**, 192 (1994).

[70] R. W. Hornbeck, *Numerical Methods* (Quantum, New York, 1975).

[71] W. H. Press, S. A. Teukolsky, W. T. Vetterling, and B. P. Flannery, *Numerical Recipes in FORTRAN*, 2nd. ed. (Cambridge University Press, Cambridge, 1992).

[72] G. Wunner, W. Rösner, H. Herold, and H. Ruder, Astron. Astrophys. **149**, 102 (1985).

[73] V. B. Pavlov-Verevkin and B. I. Zhilinskii, Phys. Lett. **78A**, 244 (1980).

[74] G. L. Surmelian and R. F. O'Connell, Astrophys. J. **190**, 741 (1974).

[75] M. Weissbluth, *Atoms and Molecules* (London, Academic Press, 1978).

[76] K. A. U. Lindgren and J. T. Virtamo, J. Phys. B **12**, 3465 (1979).

[77] J. T. Virtamo and K. A. U. Lindgren, Phys. Lett. **71A**, 329 (1979).

[78] M. E. Rose, *Relativistic Electron Theory* (Wiley, New York, 1961), pp. 181-188.

[79] G. K. Woodgate, *Elementary Atomic Structure*, 2nd ed. (Oxford, Oxford, 1980), pp. 36-42.

[80] H. Hasegawa and R. E. Howard, J. Phys. Chem. Solids **21**, 179 (1961).

[81] G. Wunner, H. Ruder, and H. Herold, Astrophys. J. **247**, 374 (1981).

[82] M. Goeppert-Mayer, Ann. Phys. (Leipzig) **9**, 273 (1931).

[83] G. Breit and E. Teller, Astrophys. J. **91**, 215 (1940).

[84] L. Spitzer and J. L. Greenstein, Astrophys. J. **114**, 407 (1951).

[85] J. Shapiro and G. Breit, Phys. Rev. **113**, 179 (1959).

[86] A. Dalgarno, in *Physics of the One- and Two-Electron Atoms*, edited by F. Bopp

Reproduced with permission of the copyright owner. Further reproduction prohibited without permission.

and H. Kleinpoppen (North-Holland, 1969).

[87] S. Klarsfeld, Phys. Lett. **30A**, 382 (1969).

[88] F. Bassani, J. J. Forney, and A. Quattropani, Phys. Rev. Lett. **39**, 1070 (1977).

[89] J. H. Tung, X. M. Ye, G. J. Salamo, and F. T. Chan, Phys. Rev. A **30**, 1175 (1984).

[90] P. C. Stancil and G. E. Copeland, Phys. Rev. A **48**, 516 (1993).

[91] G. A. Victor and A. Dalgarno, Phys. Rev. Lett. **18**, 1105 (1967).

[92] G. A. Victor, Proc. Phys. Soc. **91**, 825 (1967).

[93] G. W. F. Drake, G. A. Victor, and A. Dalgarno, Phys. Rev. **180**, 25 (1969).

[94] A. C. Hearn, *REDUCE User's Manual*, Version 3.3 (Rand Corporation, Santa Monica, 1987).

[95] J. H. Tung, A. Z. Tang, G. J. Salamo, and F. T. Chan, J. Opt. Soc. Am. B **3**, 837 (1986).

[96] S. P. Goldman and G. W. F. Drake, Phys. Rev. A **24**, 183 (1981).

[97] W. R. Johnson, Phys. Rev. Lett. **29**, 1123 (1972).

[98] J.-C. Gay, editor Comments At. Mol. Phys. **25** (4-6), (1991).

[99] P. C. Stancil and G. E. Copeland, J. Phys. B **27**, 2801 (1994).

[100] E. U. Condon and G. H. Shortley G H 1963, *The Theory of Atomic Spectra* (Cambridge University Press, London, 1963), p. 152.

[101] K. Darwin, Proc. R. Soc. London **118**, 264 (1928).

[102] J.-C. Gay and W. B. Schneider, Z. Phys. A **278**, 211 (1976).

[103] R. Walkup, A. L. Migdall, and D. E. Pritchard, Phys. Rev. A **25**, 3114 (1982).

[104] A. J. Poustie and M. H. Dunn, Phys. Rev. A **47**, 1365 (1993).

[105] S. Lepp, A. Dalgarno, and R. McCray, Astrophys. J. **358**, 262 (1990).

[106] W. Liu, A. Dalgarno, and S. Lepp, Astrophys. J. **396**, 679 (1992).

[107] P. C. Stancil, J. F. Babb, and A. Dalgarno, Astrophys. J. **414**, 672 (1993).

[108] G. Herzberg, *Molecular Spectra and Molecular Structure I. Spectra of Diatomic*

Reproduced with permission of the copyright owner. Further reproduction prohibited without permission.

Molecules (Van Nostrand Reinhold, New York, 1950).

[109] B. Zygelman and A. Dalgarno, Astrophys. J. **365**, 239 (1990).

[110] K. P. Kirby and E. F. van Dishoeck, Adv. At. Mol. Phys. **25**, 437 (1988).

[111] B. R. Johnson, J. Chem. Phys. **67**, 4086 (1977).

[112] J. D. Power, "One-electron diatomic molecules", QCPE Program no. 223 (1973).

[113] J. F. Babb, (private communication).

[114] M. M. Madsen and J. M. Peek, At. Data, **2**, 171 (1971).

[115] D. E. Ramaker and J. M. Peek, At. Data, **5**, 167 (1973).

[116] T. M. Miller, in *Handbook of Chemistry and Physics*, ed. R. C. Weast (Cleveland, CRC, 1985), p. E-67.

[117] A. Metropoulos, Y. Li, G. Hirsch, and R. J. Buenker, Chem. Phys. Lett. **198**, 266 (1992).

[118] J. Ackermann and H. Hogreve, Chem. Phys. **157**, 75 (1991).

[119] A. Metropoulos and C. A. Nicolaides, Chem. Phys. Lett. **187**, 487 (1991).

[120] C. W. Bauschlicher, Jr., H. Partridge, and D. Ceperley, Chem. Phys. Lett. **160**, 183 (1989).

[121] A. Metropoulos, C. A. Nicolaides, and R. J. Buenker, J. Chem. Phys. **114**, 1 (1987).

[122] B. K. Gupta and F. A. Matsen, J. Chem. Phys. **47**, 4860 (1967).

[123] G. Peach, J. Phys. B **11**, 2107 (1978).

[124] R. E. Johnson, S. T. Epstein, and W. J. Meath, J. Chem. Phys. **47**, 1271 (1967).

[125] B. M. McLaughlin, C. J. Gillan, P. G. Burke, and J. S. Dahler, in *Atomic and Molecular Physics*, Third US/Mexico Symposium, ed C. Cisneros, T. J. Morgan, and I. Alvarez (Hong Kong, World Scientific, 1991), p. 161.

[126] W. L. Wiese, M. W. Smith, and B. M. Glennon, NSRDS-NBS 4, vol. 1 (Washington, USGPO, 1966).

[127] N. Yu and W. H. Wing, Phys. Rev. Lett. **59**, 2055 (1987).

Reproduced with permission of the copyright owner. Further reproduction prohibited without permission.

[128] J. G. Maas, N. P. F. B. van Asselt, P. J. C. M. Nowak, J. Los, S. D. Peyerimhoff, and R. J. Buenker, Chem. Phys. **17**, 217 (1976).

[129] D. E. Ramaker and J. M. Peek, Phys. Rev. A **13**, 58 (1976).

[130] A. Dalgarno and S. Lepp, in *Astrochemistry*, ed. S. P. Tarafdar and M. P. Varshni (Reidel, 1985), p. 109.

[131] P. C. Stancil, Astrophys. J. **430**, 360 (1994).

[132] J. D. Argyros, J. Phys. B **7**, 2025 (1974).

[133] A. W. Irwin, Astrophys. J. Suppl. **45**, 621 (1981).

[134] D. Mihalas, *Stellar Atmospheres* (San Francisco, Freeman, 1978).

[135] R. A. Buckingham, S. Reid, and R. Spence, Mon. Not. R. Astron. Soc. **112**, 382 (1952).

[136] D. R. Bates, Mon. Not. R. Astron. Soc. **112**, 40 (1952).

[137] A. A. Mihajlov and M. S. Dimitrijević, Astron. Astrophys. **155**, 319 (1986) (MD1).

[138] A. A. Mihajlov and M. S. Dimitrijević, Astron. Astrophys. **256**, 305 (1992) (MD2).

[139] A. J. Sauval and J. B. Tatum, Astrophys. J. Suppl. **56**, 193 (1984).

[140] P. C. Stancil, J. Quant. Spectrosc. Radiat. Transfer **51**, 655 (1994).

[141] G. Hunter, A. W. Yau, and H. Pritchard, *At. Data and Nuc. Data Tables* **14**, 11 (1974).

[142] K. P. Huber and G. Herzberg, *Molecular Spectra and Molecular Structure IV. Constants of Diatomic Molecules* (Van Nostrand Reinhold, New York, 1979).

[143] J. B. Tatum, Publ. Dom. Astrophys. Obs. Victoria B. C. **13**, 1 (1966).

[144] D. G. Hummer and D. Mihalas, Astrophys. J. **331**, 794 (1988).

[145] E. M. Sion, J. L. Greenstein, J. D. Landstreet, J. Liebert, H. L. Shipman, and G. Wegner, Astrophys. J. **269**, 253 (1983).

[146] F. Wesemael, J. L. Greenstein, J. Liebert, R. Lamontagne, G. Fontaine, P.

Reproduced with permission of the copyright owner. Further reproduction prohibited without permission.

Bergeron, and J. W. Glaspey, Publ. Astron. Soc. Pac. **105**, 761 (1993).

[147] G. D. Schmidt, H. S. Stockman, and P. S. Smith, Astrophys. J. **398**, L57 (1992).

[148] G. D. Schmidt and P. S. Smith, Astrophys. J. , in press (1993).

[149] G. D. Schmitt, White Dwarfs, IAU Colloquium No. 114, edited by G. Wegner (Springer-Verlag, Berlin, 1988), p. 305.

[150] J. Liebert, P. Bergeron, G. D. Schmidt, and R. A. Saffer, Astrophys. J. **418**, 426 (1993).

[151] J. L. Greenstein, Astrophys. J. **281**, L47 (1984).

[152] J. L. Greenstein, R. J. W. Henry, and R. F. O'Connell, Astrophys. J. **289**, L25 (1985).

[153] G. D. Schmidt, S. C. West, J. Liebert, R. F. Green, and H. S. Stockman, Astrophys. J. **309**, 218 (1986).

[154] R. Minkowski, Ann. Rept. Dir. Mt. Wilson. Obs., p. 28 (1938).

[155] G. L. Greenstein and J. B. Oke, Astrophys. J. **225**, 285 (1982).

[156] D. Koester, V. Weidemann, E.-M. Zeidler-K.T., and G. Vauclair, Astron. Astrophys. **142**, L5 (1985).

[157] E. P. Nelan and G. Wegner, Astrophys. J. **289**, L31 (1985).

[158] J. C. Stewart, J. M. Peek, and J. Cooper, Astrophys. J. **179**, 983 (1973).

[159] K. Sando, R. O. Doyle, and A. Dalgarno, Astrophys. J. **157**, L143 (1969).

[160] K. Sando and J. C. Wormhoudt, Phys. Rev. A **7**, 1889 (1973).

[161] N. Allard and J. Kielkopf, Astron. Astrophys. **242**, 133 (1991).

[162] N. Allard and D. Koester, Astron. Astrophys. **258**, 464 (1992).

[163] J. M. Peek and J. Katriel, Phys. Rev. A **21**, 413 (1980).

[164] F. K. Lamb and P. G. Sutherland, in *Physics of Dense Matter*, IAU Symposium 53, ed. C. J. Hansen (Dordrecht, Reidel, 1974), p. 265.

[165] P. Bergeron, F. Wesemael, and G. Fontaine, Astrophys. J. **367**, 253 (1991) (BWF).

Reproduced with permission of the copyright owner. Further reproduction prohibited without permission.

[166] V. P. Gaur, B. M. Tripathi, G. C. Joshi, and M. C. Pande, Astrophys. Space Sci. **147**, 107 (1988) (GTJP).

[167] G. P. McCook and E. M. Sion, Astrophys. J. Suppl. **65**, 603 (1987).

[168] A. G. Posen, A. Dalgarno, and J. M. Peek, Atomic Data Nucl. Data **28**, 265 (1983).

[169] D. T. Wickramasinghe, D. A. Allen, and M. S. Bessell, Mon. Not. R. Astr. Soc. **198**, 473 (1982) (WAB).

[170] J. L. Linsky, Sol. Phys. **11**, 198 (1970).

[171] K. C. Kulander and C. Bottcher, J. Chem. Phys. **29**, 141 (1978).

[172] K. C. Kulander and E. J. Heller, J. Chem. Phys. **69**, 2439 (1978).

[173] C. Asaro and A. Dalgarno, J. Chem. Phys. **78**, 200 (1983).

[174] A. C. Allison and A. Dalgarno, Atomic Data **1**, 91 (1969).

[175] A. L. Ford, K. Kirby Docken, and A. Dalgarno, Astrophys. J. **195**, 819 (1975).

[176] S. Geltman, Astrophys. J. **136**, 935 (1962).

[177] J. L. Greenstein, Astrophys. J. **276**, 602 (1984).

[178] S. Vennes, Astrophys. J. **390**, 590 (1992).

[179] S. Vennes and G. Fontaine, Astrophys. J. **401**, 288 (1992).

[180] D. Koester, Astron. Astrophys. **29**, 401 (1980).

[181] W. B. Somerville, Astrophys. J. **141**, 811 (1965).

[182] G. Wegner, Mon. Not. R. Astron. Soc. **163**, 381 (1973).

[183] D. T. Wickramasinghe and M. S. Bessell, Mon. Not. R. Astron. Soc. **186**, 399 (1979).

[184] P. Bergeron, F. Wesemael, G. Fontaine, and J. Liebert, Astrophys. J. **351**, L21 (1990).

[185] O. J. Eggen and J. L. Greenstein, Astrophys. J. **141**, 83 (1965).

[186] R. Wehrse and J. Liebert, Astron. Astrophys. **83**, 184 (1980).

[187] M. H. Cohen, A. Putney, and R. W. Goodrich, Astrophys. J. **405**, L67 (1993).

Reproduced with permission of the copyright owner. Further reproduction prohibited without permission.

[188] S. Vennes, J. Dupuis, T. Rumph, J. Drake, S. Bowyer, P. Chayer, and G. Fontaine, Astrophys. J. **410**, L119 (1993).

[189] G. Wegner and S. R. Swanson, Astrophys. J. Supp. **75**, 507 (1991).

[190] S. Bowyer and R. F. Malina, in *Extreme Ultraviolet Astronomy*, ed. R. F. Malina and S. Bowyer (New York, Pergamon, 1991), p. 397.

[191] M. L. Du, Phys. Rev. A **40**, 1330 (1989).

Reproduced with permission of the copyright owner. Further reproduction prohibited without permission.

APPENDIX A

Infinite Proton Mass Energies for Hydrogen

TABLE A-1. Nonrelativistic infinite proton mass energy values for hydrogen s-states in a magnetic field for $m_s = -\frac{1}{2}$.

B (au)	E_{NR}^{∞} (au)			
	$1s$	$2s$	$3s'$	$4s'$
0.20000000-4	-0.500009999900000	-0.12500999859999	-0.05556554772415	-0.0312599738705
0.20000000-3	-0.500099990000000	-0.12509986000024	-0.0556547724276	-0.03134738727
0.10000000-2	-0.50049975000027	-0.12549650015930	-0.0560359850234	-0.0316848127934
0.20000000-2	-0.500999000004417	-0.125986002548	-0.05647736875	-0.031990851407
0.42543812-2	-0.502122665753065	-0.1270638935094	-0.0573309413	-0.032235571026
0.60000000-2	-0.50299100035769	-0.1278742054550	-0.057860655082	
0.10000000-1	-0.50497500275921	-0.129651571358	-0.0586693295753	
0.20000000-1	-0.5099000440894	-0.133624177535	-0.05863423389	
0.42543812-1	-0.520820309276	-0.140363458803	-0.052367	
0.50000000-1	-0.524376706706	-0.142016720515		
0.60000000-1	-0.529103522563	-0.143863462506		
0.70000000-1	-0.533781490585	-0.1453419092		
0.80000000-1	-0.5384110043895	-0.146507411		
0.90000000-1	-0.54299250579	-0.147408855		
0.10000000	-0.547526480401	-0.14808916	-0.043565	
0.12000000	-0.5564539834772	-0.14893174716		
0.13610402	-0.56350890784	-0.1492424440		
0.15000000	-0.5695029457788	-0.14933121		
0.20000000	-0.59038156503	-0.14898667		
0.25000000	-0.610247435260			
0.30000000	-0.629186552901			
0.35000000	-0.647280764956			
0.40000000	-0.6646053799			
0.45000000	-0.6812283864			
0.50000000	-0.6972105385			
0.60000000	-0.727462288			
0.80000000	-0.782283394			
1.00000000	-0.831168896			

Reproduced with permission of the copyright owner. Further reproduction prohibited without permission.

TABLE A-2. Nonrelativistic infinite proton mass energy values for hydrogen p_0-states in a magnetic field for $m_s = -\frac{1}{2}$.

B (au)	E_{NR}^{∞} (au)		
	$2p_0$	$3p_0$	$4p_0'$
0.2000000000-4	-0.125009999400000	-0.055565551955555	-0.03125998454037
0.2000000000-3	-0.1250999400001	-0.055655195561	-0.031348454156
0.1000000000-2	-0.1254985000420	-0.056046559083206	-0.031711425902
0.2000000000-2	-0.1259940006717	-0.05651961183	-0.03209658635
0.4254381205-2	-0.127100054697536	-0.0575209852313	-0.0327003874
0.6000000000-2	-0.1279460542354	-0.058235979481	-0.0329425014298
0.1000000000-1	-0.1298504158325	-0.059687869978	-0.0329178768
0.2000000000-1	-0.13440646598	-0.062378561912	-0.0309425516
0.4254381205-1	-0.14367503059	-0.0656741839	-0.026193
0.5000000000-1	-0.146464837782	-0.0663804983	-0.025398
0.6000000000-1	-0.150016268441	-0.067203260	-0.024712
0.7000000000-1	-0.153368549	-0.067940690	-0.02431
0.8000000000-1	-0.156540574	-0.0686254	-0.02410
0.9000000000-1	-0.159549365		-0.02399
0.1000000000	-0.1624100789		
0.1200000000	-0.16773940		
0.1361040199	-0.17169962		-0.023724
0.1500000000	-0.17491128		-0.0229492
0.2000000000	-0.18518404		

B (au)	E_{NR}^{∞} (au)		
	$5p_0'$	$6p_0'$	$7p_0'$
0.2000000000-4	-0.02000995619811	-0.0138987883546	-0.010213900
0.2000000000-3	-0.02009562111	-0.013978844445	
0.1000000000-2	-0.020391295	-0.01414279	
0.2000000000-2	-0.0205741476	-0.01395725	
0.4254381205-2	-0.0203521314	-0.012507	
0.6000000000-2	-0.019748593	-0.011307	
0.1000000000-1	-0.017724047		
0.2000000000-1	-0.0161		

Reproduced with permission of the copyright owner. Further reproduction prohibited without permission.

TABLE A-3. Nonrelativistic infinite proton mass energy values for hydrogen p_{-1}-states in a magnetic field for $m_s = -\frac{1}{2}$.

B (au)	E_{NR}^{∞} (au)	
	$2p_{-1}$	$3p_{-1}$
0.2000000000-4	-0.1250199987999998	-0.055575548355556
0.2000000000-3	-0.1251998800002	-0.05575483556696
0.1000000000-2	-0.125997000115	-0.0565375627456
0.2000000000-2	-0.12698800185	-0.0574836701743
0.4254381205-2	-0.1292001198328	-0.059486448706
0.6000000000-2	-0.1308921495869	-0.060916499227
0.1000000000-1	-0.134701144177	-0.063820114240
0.2000000000-1	-0.143817610348	-0.069175122
0.4254381205-1	-0.1624245019	-0.0752014
0.5000000000-1	-0.168058188	
0.6000000000-1	-0.1752644186	
0.7000000000-1	-0.182110099	
0.8000000000-1	-0.188633895	
0.9000000000-1	-0.194869409	
0.1000000000	-0.2008456724	
0.1200000000	-0.212119	
0.1361040199	-0.220622253	
0.1500000000	-0.227607738	
0.2000000000	-0.2505391	

Reproduced with permission of the copyright owner. Further reproduction prohibited without permission.

TABLE A-4. Nonrelativistic infinite proton mass energy values for hydrogen p_1-states in a magnetic field for $m_s = -\frac{1}{2}$.

B (au)	E_{NR}^{∞} (au)			
	$2p_1$	$3p_1$	$4p_1'$	$6p_1'$
0.2000000000-4	-0.12499999880000	-0.05555554835556	-0.03124997500246	-0.01388875075
0.2000000000-3	-0.1249998800002	-0.055554835567	-0.0312475004520	-0.0138750868
0.1000000000-2	-0.1249970001150	-0.05553756274558	-0.0311876353495	-0.013550761
0.2000000000-2	-0.124988001854965	-0.05548367017435	-0.03100205581971	-0.01260732
0.4254381205-2	-0.12494573862783	-0.055232067501		-0.008997
0.6000000000-2	-0.1248921495869	-0.054916499227		-0.006578
0.1000000000-1	-0.124701144177	-0.053820114240		-0.00255
0.2000000000-1	-0.12381761035	-0.0491751219		+0.003
0.4254381205-1	-0.1198806899	-0.0326576393		
0.5000000000-1	-0.118058188454	-0.0262577241		
0.6000000000-1	-0.115264418760	-0.017373301		
0.7000000000-1	-0.112110099393	-0.008333532		
0.8000000000-1	-0.108633896259	+0.00074172		
0.9000000000-1	-0.104869409125	+0.0098005		
0.1000000000	-0.10084567237	+0.01882881		
0.1200000000	-0.09211734640	+0.036822		
0.1361040199	-0.0845196	+0.05129765		
0.1500000000	-0.0776078	+0.063810		
0.2000000000	-0.050539102	+0.109158		

Reproduced with permission of the copyright owner. Further reproduction prohibited without permission.

TABLE A-5. Nonrelativistic infinite proton mass energy values for hydrogen d_0-states in a magnetic field for $m_s = -\frac{1}{2}$.

B (au)	E_{NR}^{∞} (au)	
	$3d_0'$	$4d_0'$
0.0000000000	-0.0555555555556	-0.03125000000000
0.2000000000-4	-0.055565553486961	-0.03125999252953
0.2000000000-3	-0.0556553486978	-0.03134925301
0.1000000000-2	-0.05605038508701	-0.0317313574831
0.2000000000-2	-0.0565348858464	-0.032175827349
0.4254381205-2	-0.0575894725487	-0.03304946802
0.6000000000-2	-0.058370667691	
0.1000000000-1	-0.060047921913	
0.2000000000-1	-0.06361693547	
0.4254381205-1	-0.06919113	
0.6000000000-1	-0.07191328	
0.7000000000-1	-0.0730289	
0.8000000000-1	-0.07388250	
0.9000000000-1	-0.074509427	
0.1000000000	-0.074938	
0.1200000000	-0.0752912	
0.1361040199	-0.0751731	
0.1500000000	-0.074842	
0.2000000000	-0.07261	

Reproduced with permission of the copyright owner. Further reproduction prohibited without permission.

TABLE A-6. Nonrelativistic infinite proton mass energy values for hydrogen d_{-1}-states in a magnetic field for $m_s = -\frac{1}{2}$.

B (au)	E^{∞}_{NR} (au)	
	$3d_{-1}$	$4d_{-1}$
0.2000000000-4	-0.055575551955556	-0.03126998560001
0.2000000000-3	-0.055755195559	-0.03144856010914
0.1000000000-2	-0.0565465580136	-0.03221406788860
0.2000000000-2	-0.057519594775	-0.033107070606
0.4254381205-2		-0.034873378658
0.6000000000-2	-0.061234642207	-0.03602996327
0.1000000000-1	-0.064678149523	-0.03813218160
0.2000000000-1	-0.072253547538	
0.4254381205-1	-0.086	
0.5000000000-1	-0.089120138	
0.6000000000-1	-0.0935275038	
0.7000000000-1	-0.097536313	
0.8000000000-1	-0.1012194	
0.9000000000-1	-0.1046309	
0.1000000000	-0.10781210	
0.1200000000	-0.113606	
0.1361040199	-0.1178219	
0.1500000000	-0.12119	
0.2000000000	-0.131785	

Reproduced with permission of the copyright owner. Further reproduction prohibited without permission.

TABLE A-7. Nonrelativistic infinite proton mass energy values for hydrogen d_1-states in a magnetic field for $m_s = -\frac{1}{2}$.

B (au)	E_{NR}^{∞} (au)	
	$3d_1$	$6d_1'$
0.2000000000-4	-0.05555555195556	-0.0138887907455
0.2000000000-3	-0.055555195560	-0.013879083
0.1000000000-2	-0.05554655801363	-0.013648578
0.2000000000-2	-0.0555195947749	-0.012978557
0.4254381205-2	-0.05539345044	-0.0104503
0.6000000000-2		-0.008077
0.1000000000-1		-0.00350
0.2000000000-1		+0.0027
0.4254381205-1		+0.022

TABLE A-8. Nonrelativistic infinite proton mass energy values for hydrogen states in a magnetic field for $m_s = -\frac{1}{2}$.

B (au)	E_{NR}^{∞} (au)		
	$5f_0'$	$6f_0'$	$6h_0'$
0.0000000000	-0.020000000000	-0.01388888889	-0.01388888889
0.2000000000-2	-0.020866092003	-0.01445258378	-0.01468790601
0.4254381205-2	-0.02156111830	-0.01427837	-0.015195043

Reproduced with permission of the copyright owner. Further reproduction prohibited without permission.

APPENDIX B

Relativistic Corrections for Hydrogen

TABLE B-1. Relativistic infinite proton mass corrections for hydrogen in a magnetic field.

State $n\ell_m(jm_j)$	B(au)	ΔE_{R} (10^{-6} au)			
		ΔE_{KE}	ΔE_{SO}	ΔE_{D}	Total
$1s\ (\frac{1}{2},-\frac{1}{2})$	0	-33.282101233	0.0	26.625680987	-6.6564202
	2×10^{-5}	-33.2821054687	0.0	26.62568492	-6.6564205475
	2×10^{-4}	-33.282100263	0.0	26.625678759	-6.65642150
	10^{-2}	-33.285657168	6.5738485545-5	26.6281211	-6.657529
	0.1	-33.62954312	-3.8258451339-2	26.86381234	-6.803989
	1	-52.71340467	-1.077778612	38.52199108	-15.2691922
$2s\ (\frac{1}{2},-\frac{1}{2})$	0	-5.4083415	0.0	3.3282101	-2.0801313
	10^{-2}	-5.43916	-4.23455	3.34620	-2.09338
	5×10^{-2}	-6.0458	-7.3077-3	3.6928	-2.3602
	0.1	-7.1752	-2.9616-2	4.3013	-2.9035
	0.2	-8.479	-0.02291	4.803	-3.699
$2p_0\ (\frac{1}{2},-\frac{1}{2})$	0	-0.97072795	-1.1094034	0.0	-2.0801313
	2×10^{-5}	-0.97072818	-1.1094036	0.0	-2.0801318
	10^{-2}	-0.974033	-1.11163	0.0	-2.08566
	0.1	-1.23881	-1.24469	0.0	-2.48349
$2p_{-1}\ (\frac{3}{2},-\frac{3}{2})$	0	-0.9707280	0.5547017	0.0	-0.4160263
	0.1	-1.5411	0.74595	0.0	-0.79511
$3p_0\ (\frac{1}{2},-\frac{1}{2})$	0	-0.410890	-0.328712	0.0	-0.739602
$3d'_0\ (\frac{3}{2},-\frac{1}{2})$	0	-0.147920	-0.0986136	0.0	-0.246534
	2×10^{-5}	-0.402933	-1.34168	0.159383	-1.58523

Reproduced with permission of the copyright owner. Further reproduction prohibited without permission.

APPENDIX C

Transition Wavelengths and Probabilities for H

TABLE C-1. Transition wavelengths, dipole moments, oscillator strengths, and transition probabilities for the Lyα transitions of hydrogen in a magnetic field. The wavelengths and transition probabilities include the finite nuclear mass correction.

B (au)	λ (Å) D^2_{ab} (au) f_{ba} A_{ab} (s^{-1})		
	$1s \rightarrow 2p_{-1}$	$1s \rightarrow 2p_0$	$1s \rightarrow 2p_1$
0.0000000000	1215.684474	1215.684474	1215.684474
	0.5549289	0.5549290	0.5549290
	0.4161967	0.4161967	0.4161967
	625808500.0	625808580.4	625808580.4
0.2000000000-4	1215.716854	1215.684472	1215.652088
	0.5549290	0.554929	0.554928966
	0.4161856	0.4161967	0.416207824
	625758600.0	625809000.0	625858610.0
0.2000000000-3	1216.008033	1215.684312	1215.360374
	0.554930	0.554929	0.554930
	0.416086	0.4161971	0.4163084
	625310000.0	625809300.0	626310300.0
0.1000000000-2	1217.296841	1215.680422	1214.058590
	0.554948	0.554938	0.55495
	0.415659	0.4162052	0.41677
	623346000.0	625825000.0	628350000.0
0.2000000000-2	1218.895571	1215.6682671	1212.419321
	0.55500445	0.55496649	0.55500445
	0.4151555	0.41623042	0.417375554
	620960110.0	625875940.0	630964107.0
0.4254381205-2	1222.449135	1215.611177189	1208.675417
	0.55526991	0.55510	0.55526991
	0.41414534	0.41635	0.418869997
	615855000.0	626110000.0	637150180.0

Reproduced with permission of the copyright owner. Further reproduction prohibited without permission.

0.6000000000-2	1225.152056	1215.5387838	1205.731302
	0.5556055	0.555266	0.555605499
	0.4134803	0.4164992	0.420147602
	612157700.0	626414000.0	642216803.0
0.1000000000-1	1231.183240	1215.2807189	1198.841835
	0.556792554	0.555859	0.5567926
	0.412331455	0.417033	0.4234673
	604494110.0	627482200.0	654748500.0
0.2000000000-1	1245.260806	1214.086483160	1180.821780
	0.562110	0.55855	0.5621100
	0.411557	0.419462	0.434042
	589803000.0	632380000.0	691727000.0
0.4254381205-1	1271.923894	1208.769414477	1137.098996
	0.583000	0.56958	0.5829996
	0.417889	0.42963	0.4674953
	574052000.0	653420000.0	803415400.0
0.5000000000-1	1279.32397	1206.317438431	1122.056289
	0.59145	0.574233	0.5914472
	0.42149	0.434019	0.4806319
	572320000.0	662780000.0	848279000.0
0.6000000000-1	1288.267897	1202.57717116	1101.678630
	0.60322	0.58090	0.60322
	0.42689	0.44042	0.49928
	571650000.0	676750000.0	914070000.0
0.7000000000-1	1296.18800	1198.38635298	1081.228012
	0.615096	0.58783	0.615096
	0.432623	0.44724	0.518737
	572276000.0	692040000.0	985956000.0
0.8000000000-1	1303.18668	1193.81246049	1060.847390
	0.626723	0.594833	0.6267234
	0.438427	0.4542982	0.538703
	573750100.0	708359000.0	1063614000.0
0.1000000000	1314.783002	1183.750355270	1020.722830
	0.64839482	0.608503	0.64839482
	0.449572079	0.4686893	0.57925104
	578021550.0	743274800.0	1235329430.0

Reproduced with permission of the copyright owner. Further reproduction prohibited without permission.

0.1200000000	1323.70	1172.7928305	981.930
	0.66721	0.621172	0.667200
	0.45949	0.482917	0.619611
	582860000.0	780216000.0	1427847000.0
0.1361040199	1329.25241	1163.5295257	951.905
	0.68002	0.6303997	0.68003
	0.46634	0.4939929	0.6515
	586600000.0	810868620.0	1597400000.0
0.1500000000	1333.07723	1155.325149	926.940
	0.689419	0.6376016	0.68942
	0.471418	0.50318457	0.678243
	589636000.0	837728800.0	1753860000.0
0.2000000000	1341.01996	1125.085048	844.64221
	0.7116468	0.657743	0.7116468
	0.4836956	0.533031	0.7683543
	597895800.0	935765000.0	2392836000.0

Reproduced with permission of the copyright owner. Further reproduction prohibited without permission.

TABLE C-2. Transition wavelengths, dipole moments, oscillator strengths, and transition probabilities for a Hα transition of hydrogen in a magnetic field. The wavelengths and transition probabilities include the finite nuclear mass correction.

B (au)	λ (Å) D^2_{ab} (au) f_{ba} A_{ab} (s^{-1})
	$2p_0 \rightarrow 3d_{-1}$
0.0000000000	6564.696159 4.5086850 0.6262062 32290350.0
0.2000000000-4	6565.640297 4.5087 0.626116 32276400.0
0.2000000000-3	6574.1241807 4.50871 0.62531 32151800.0
0.1000000000-2	6611.5335054 4.50926 0.621844 31613000.0
0.2000000000-2	6657.5885706 4.510955 0.6177699 30973080.0
0.6000000000-2	6833.303665 4.52811 0.604153 28753550.0
0.1000000000-1	6994.440885 4.55779 0.594083 26987400.0

Reproduced with permission of the copyright owner. Further reproduction prohibited without permission.

0.2000000000-1	7333.553533 4.6442 0.57730 23858000.0
0.6000000000-1	8065.63882 4.5431542 0.513274333 17543163.0
0.7000000000-1	8159.63093 4.43140 0.494830 16527090.0
0.8000000000-1	8234.14717 4.30709 0.476547 15631290.0
0.9000000000-1	8293.65560 4.176880 0.4587758 14834770.0
0.1000000000	8341.46536 4.0452 0.44172 14121600.0
0.1200000000	8411.32453 3.78819 0.41013 12897500.0
0.1361040199	8449.78923 3.59332 0.387200 12067720.0
0.1500000000	8473.62334 3.436 0.3691 11440000.0

Reproduced with permission of the copyright owner. Further reproduction prohibited without permission.

0.2000000000	8519.80027
	2.9514
	0.31520
	9669500.0

Reproduced with permission of the copyright owner. Further reproduction prohibited without permission.

TABLE C-3. Transition wavelengths, dipole moments, oscillator strengths, and transition probabilities for the Paschen transitions of hydrogen in a magnetic field. The wavelengths and transition probabilities include the finite nuclear mass correction.

B (au)	λ (Å) D^2_{ab} (au) f_{ba} A_{ab} (s^{-1})	
	$3d'_0 \rightarrow 4p'_0$	$3d'_0 \rightarrow 5p'_0$
0.0000000000	18756.274739 0.15308287018367 0.74415284117063-2 47006.0302291	12821.672185
0.2000000000-4	18756.264406 1.55754 0.757136-1 478262.0	12821.657136
0.2000000000-3	18755.241518 1.5578 0.75730-1 478400.0	12820.167884
0.1000000000-2	18730.532979 1.56400 0.76132-1 482230.0	12784.444920
0.2000000000-2	18654.394417 1.5832 0.77381-1 494150.0	12677.205728
0.4254381205-2	18316.530095	12242.6
0.6000000000-2	17928.216806	11803.655136
0.1000000000-1	16803.572379 2.09315 0.113574 893845.0	10771.265041

Reproduced with permission of the copyright owner. Further reproduction prohibited without permission.

0.2000000000-1	13952.265462 3.30178 0.21577 2463100.0	9601.9
0.4254381205-1	10602.342	8697.
0.6000000000-1	9658.41375 2.9 0.27 6500000.0	
0.7000000000-1	9358.46 2.12 0.207 5250000.0	
0.8000000000-1	9197.162 2. 0.2 6000000.0	
0.9000000000-1	9024.17 1.37 0.138 3780000.0	
0.1361040199	8900.039	
0.1500000000	8785.113	

Reproduced with permission of the copyright owner. Further reproduction prohibited without permission.

TABLE C-4. Transition wavelengths, dipole moments, oscillator strengths, and transition probabilities for some $n = 6$ transitions of hydrogen in a magnetic field. The wavelengths and transition probabilities include the finite nuclear mass correction.

B (au)	λ (Å) D^2_{ab} (au) f_{ba} A_{ab} (s^{-1})		
	$1s \rightarrow 6p'_0$	$2s \rightarrow 6p'_0$	$3s' \rightarrow 6p'_0$
0.2000000000-4	937.813543215 0.0035379 0.00343962 8690900.0	4102.93143858	10941.1359220
0.2000000000-3	937.79437876 0.0035404 0.0034421 8697500.0	4102.5693964	10938.728897
0.1000000000-2	937.3397 0.003593 0.0034946 8839000.0	4093.996 1. 0.2 30000000.	10882.00
0.2000000000-2	936.0218 0.003675 0.003580 9080000.0	4069.327 0.5 0.12 160000000.	10721.55
0.4254381205-2	931.10 0.00311 0.00305 7820000.0	3979.5	10170.58
0.6000000000-2	927.18 0.00120 0.00118 3040000.0	3910.9	9792.6 0.0002 0.0002 500.

Reproduced with permission of the copyright owner. Further reproduction prohibited without permission.

APPENDIX D

Transition Wavelengths and Probabilities for He^+

TABLE D-1. Transition wavelengths, dipole moments, and transition probabilities for the Lyα transitions of He^+ in a magnetic field. The wavelengths and transition probabilities include the finite nuclear mass correction.

B (au)	λ (Å) D^2_{ab} (au) A_{ab} (s^{-1})		
	$1s \rightarrow 2p_{-1}$	$1s \rightarrow 2p_0$	$1s \rightarrow 2p_1$
0.0000000000	303.7973308845633	303.797330848424	303.7973308345836
	0.1387322247028351	0.1387322396039963	0.1387322396039963
	10025180833.58407	10025182121.23682	10025182121.27599
0.7997806957-4	303.8054291958289	303.7973304422435	303.7892311320411
	0.1387322545051575	0.1387322545051575	0.1387322396039963
	10024380803.06877	10025188843.36728	10025984182.21896
0.7997806957-3	303.8782538034326	303.7972903410835	303.7162729559642
	0.1387324929237366	0.1387322545051575	0.1387324184179306
	10017188541.33935	10025193649.23721	10033224108.77320
0.3998903478-2	304.2005897330146	303.7963182221906	303.3906960469545
	0.1387369930744171	0.1387345045804977	0.1387368738651276
	9985700027.521420	10025445156.43004	10065882488.34517
0.7997806957-2	304.6004424622585	303.7932808098381	302.9807178267811
	0.1387511193752289	0.1387416273355484	0.1387511193752289
	9947446644.887281	10026261193.14362	10107837205.48545
0.1701285980-1	305.4892286656628	303.7790141452939	302.0443908883298
	0.1388174742460251	0.1387750059366226	0.1388174742460251
	9865592373.378040	10030010732.86049	10207010488.44977
0.2399342087-1	306.1652757611346	303.7609231695331	301.3081014291502
	0.1389013677835464	0.1388165056705475	0.1389013677835464
	9806307467.726307	10034880681.05296	10288234486.52612
0.3998903478-1	307.6738330465835	303.6964332221069	299.5851730335059
	0.1391981393098831	0.1389647573232651	0.1391981393098831
	9683413570.321974	10051992781.90561	10489123974.34347

Reproduced with permission of the copyright owner. Further reproduction prohibited without permission.

0.7997806957-1	311.1953358811131	303.3979958906955	295.0789729467983
	0.1405275017023087	0.1396375000476837	0.1405274718999863
	9447756801.452646	10130453414.33026	11081873182.40885
0.1701285980	317.8668471817093	302.0692701328429	284.1466659912062
	0.1457500010728836	0.1423950046300888	0.1457498818635941
	9194728667.137867	10467505091.86198	12872035598.56674
0.1999451739	319.7190207430488	301.4565257949007	280.3857457603841
	0.1478624939918518	0.1435582488775253	0.147861793637275
	9166744369.059544	10617448233.57761	13591109877.59527
0.2399342087	321.9580592911887	300.5218398315390	275.2911992776122
	0.1508049964904785	0.1452250033617020	0.1508062332868576
	9155685527.590792	10841241576.50147	14645662906.49513
0.2799232435	323.9413098241819	299.4745620184750	270.1786127111363
	0.1537739932537079	0.1469575017690659	0.1537739634513855
	9165381133.136999	11086180747.10318	15797801487.01889
0.3199122783	325.6943493347305	298.3315546346240	265.0836999280058
	0.1566807478666306	0.1487082540988922	0.1566808521747589
	9188656331.010260	11347604051.55376	17042511968.85802
0.3998903478	328.6005229746676	295.8170529079896	255.0534814932115
	0.1620987057685852	0.1521257460117340	0.1620987057685852
	9256387564.773739	11906940028.85233	19794863525.34949
0.4798684174	330.8372270721421	293.0787874703515	245.3565491716176
	0.1668024957180023	0.1552930027246475	0.1667999327182770
	9333184494.985815	12498722035.98326	22880718550.57314
0.5442668386	332.2315227396202	290.7639045105070	237.8517556794639
	0.1700049936771393	0.1575999259948730	0.1700078099966049
	9392515626.370775	12989763718.10030	25598618979.56261
0.5998355217	333.1931708476985	288.7136457498349	231.6118625600677
	0.1723547428846359	0.1594004034996033	0.1723544895648956
	9440644776.548084	13420052155.73355	28106511837.62339
0.7997806957	335.1988675129897	281.1566997116480	211.0426513729365
	0.1779116988182068	0.1644357442855835	0.1779116839170456
	9571138689.904272	14990549573.45386	38349571997.42470

Reproduced with permission of the copyright owner. Further reproduction prohibited without permission.

BIOGRAPHICAL INFORMATION

Phillip Charles Stancil was born in Norfolk, Virginia in 1963. He received his undergraduate education at Old Dominion University obtaining bachelor's degrees in physics and mechanical engineering. After graduating in 1986, he was a mechanical engineer and project manager with the local consulting firm Clark-Smith Associates. In 1988, Phillip returned to Old Dominion to pursue graduate studies in physics and received a research assistantship at the NASA Langley Research Center in Hampton, Virginia. While at NASA he investigated atomic oxygen effects on polymers and composites with Prof. Wynford L. Harries of the Department of Physics and Dr. Edward R. Long, Jr. and Dr. Sheila A. Thibeault, both of NASA Langley. He began computational investigations of magnetic field effects on atoms with Prof. Gary E. Copeland in 1990 and was supported by teaching assistantships until becoming a predoctoral fellow at the Harvard-Smithsonian Center for Astrophysics in 1992. Under the joint direction of Prof. Alex Dalgarno of the Astronomy Department at Harvard University and Prof. Copeland, Phillip expanded his research to include formation and destruction mechanisms of diatomic molecules and applications of atomic and molecular computations to white dwarf stars. He is a member of the Tidewater Chapter of the Sigma Xi Scientific Research Society and received their award for outstanding graduate student research for 1994. He has received fellowships from the Smithsonian Astrophysical Observatory and the Virginia Space Grant Consortium and is an author on six publications. Phillip is scheduled to graduate in August 1994 and soon after to begin a postdoctoral appointment at the University of Nevada, Las Vegas.

Reproduced with permission of the copyright owner. Further reproduction prohibited without permission.